University of Southampton
Faculty of Physical Sciences and Engineering

Transparent conductive oxide based hybrid nanostructures for electro-optical modulation

Christoph Alexander Riedel
Thesis for the degree of Doctor of Philosophy

12 March 2018

Supervisors: Professor CH Kees de Groot
Professor Otto Muskens

School of Electronics and Computer Science

Acknowledgements

I benefited from much support and help throughout the time during which this thesis was performed and written. First and foremost, thanks go to my wife and our families, who with their incessant support were able to help lift the general burden of research. I would also like to thank my supervisors Kees de Groot and Otto Muskens, who gave me the opportunity to do research with them. Their encompassing help, be it with large-scale organisational issues or minute details, was greatly appreciated. The experimental work of this thesis was supported by a large number of students from the ECS Nano group and the Physics Integrated Nanophotonics group. Specially mentioned are my close friends at ECS, Nikolaos Matthaiakakis, Ben Lowe, Sahar Mirzaei and Jack Nonofu. I would also like to thank Yudong Wang, Sun Kai, Ruomeng Huang and Anushka Gangnaik for their support regarding the many aspects of cleanroom fabrication. The same goes for Leo Black, Daniel Traviss, Roman Bruck and Wei Xiao from Physics for all the support related to optical measurements. For proof-reading, editing and general advice, I would like to thank Ben Lowe, Nikolaos Matthaiakakis, Patrik Rath and Carlos Ríos Ocampo.

To my wonderful wife,
without whose considerable help and support
this thesis would have been a significantly more long-lasting
and depressing work.

UNIVERSITY OF SOUTHAMPTON

ABSTRACT

FACULTY OF PHYSICAL SCIENCES AND ENGINEERING
Engineering and Computer Science

Doctor of Philosophy

TRANSPARENT CONDUCTIVE OXIDE BASED HYBRID NANOSTRUCTURES FOR ELECTRO-OPTICAL MODULATION

by Christoph Alexander Riedel

In the last decades, plasmonic resonant nanoantennas have created interest in a wide range of research fields that deal with light confinement on the nanoscale. One promising new research branch involves electrically switchable optical properties, which are scaled down to sub-μm size using plasmonic structures. In this thesis, samples with antenna structures whose resonances can be electrically modulated were designed, fabricated and characterised both electrically and optically. A comprehensive analytical study on the interaction of carrier modulation and optical antennas showed that shifts of the resonance wavelength depend on the antenna aspect ratio and material, and are enhanced if the surrounding medium's permittivity is near zero.

The simulation capabilities of the properties of transparent conductive oxides were successfully utilised to design an ultrathin optical solar reflector that selectively radiates visible and near-infrared light while strongly absorbing mid-infrared light. The measured solar absorptance was 0.12 and the IR emissivity 0.79. Such selective reflectors can replace currently-used metallised quartz tiles to reduce launch costs of spacecraft. Combining electrical and optical simulation models with nanoscale resolution, a novel modulator structure was designed. By directly electrically addressing nanoantennas, a modulator was enabled to perform in transmission additionally to reflection. Reducing the ITO volume to a gap-filling removed negative impacts of the ITO background, so that the resulting modulator could freely shift the resonance of the antenna. The final structure showed a greatly enhanced amplitude modulation of 45% and a resonance shift of $38\,\mathrm{nm}$ at $1550\,\mathrm{nm}$ with an applied electric field of $1\,\mathrm{V\,nm^{-1}}$.

Fabricated structures showed that the placing of an ITO gap-loading can be achieved by taking into account height alignment errors of current e-beam systems. Experiments on a planar electrical modulator with a TiN-HfO_2-ITO stack showed first electro-optical modulation results, which can benefit from the design developed with the simulation model. The promising results obtained in this thesis open a new pathway for electro-plasmonic modulation in a variety of structures such as tunable reflectors and transmitters in free space or on silicon waveguides.

Contents

Declaration of Authorship

I, Christoph Alexander Riedel, declare that the thesis entitled *Transparent conductive oxide based hybrid nanostructures for electro-optical modulation* and the work presented therein are both my own and have been generated by me as the result of my own original research. I confirm that:

- this work was done wholly or mainly while in candidature for a research degree at this university;
- where any part of this thesis has previously been submitted for a degree or any other qualification at this university or any other institution, this has been clearly stated;
- where I have consulted the published work of others, this is always clearly attributed;
- where I have quoted from the work of others, the source is always given. With the exception of such quotations, this thesis is entirely my own work;
- I have acknowledged all main sources of help;
- where the thesis is based on work done by myself jointly with others, I have made clear exactly what was done by others and what I have contributed myself;
- parts of this work have been published as:
  - Journal articles:
    - C. A. Riedel et al. ‘Nanoscale modeling of electro-plasmonic tunable devices for modulators and metasurfaces’, *Optics Express* 25.9, pp. 10031–10043 (2017).
    - K. Sun et al. ‘Metasurface optical solar reflectors using AZO transparent conducting oxide for radiative cooling of spacecraft’, *ACS Photonics* 5.2, 495–501.
    - K. Sun et al. ‘VO_2 thermo-chromic metamaterial-based smart optical solar reflector’, *ACS Photonics*, *submitted.*
  - Conference talks:
    - CH de Groot et al. ‘Quantification of misalignment in e-beam lithography due to height map error on optically non-uniform substrates for plasmonic nanoantennas’, *International Conference on Nanotechnology (IEEE nano) 2015.*
    - C. A. Riedel et al. ‘Electrically Tunable Gap-Loaded Plasmonic Nanostructures’, *CLEO®/Europe-EQEC 2017.*
    - Otto L. Muskens et al. ‘Metal oxide metasurfaces for active control and space technology’, *CLEO®/Europe-EQEC 2017.*

- Conference poster presentations:
    - C. A. Riedel et al. ‘Electrical Modulation of Plasmonic Structures’, *International Conference on Micro and Nano Engineering (MNE) 2016*.
    - C. A. Riedel et al. ‘Electrically Tunable Plasmonic Nanoantennas’, *Gordon Research Council on Plasmonics and Nanophotonics 2016*.

Signed:. . . . .

Date:. . . . .

List of Acronyms and Symbols

A	Absorbed power
A_e	Thermally emitting surface area
A_s	Area exposed to solar radiation
B	Black body radiation
I	Intensity
L	Length of a particle
N	Carrier concentration
N_i	Induced carrier concentration by an electric bias
R	Radius of a rod
S	Scattered power
T	Temperature
V	Applied bias voltage
$\Delta R/R$	Normalised reflected power of a spatially modulated signal
Γ	Scattering constant
Γ_l	Damping of a Lorentz oscillator
α	Solar absorptance
δ_y	Width of the spatial modulation
ϵ	Infrared emissivity
$\hbar$	Reduced Planck constant
λ_t	Transition wavlength
μ	Electron mobility
ω	Angular frequency
ω_l	Spectral position of a Lorentz oscillator
ω_p	Plasma frequency
σ_{ext}	Extinction cross section
σ_{sol}	Solar constant
$\tilde{n}$	Complex refractive index
ε_0	Electric permittivity of the vacuum
ε_r	Relative electric permittivity
ε_r'	Real part of ε_r
ε_r''	Imaginary part of ε_r
ε_∞	Background permittivity
ε_m	Relative electric permittivity of a medium
ε_{np}	Relative electric permittivity of a nanoparticle
$\vec{E}$	Electric field vector
a	Long dimension of a particle
b	Short dimension of a particle

c_0	Speed of light in vacuum
d	Film thickness
e	Electron charge
f_0	Spatial modulation frequency
g	Geometrical factor of Mie-Gans theory
k	Absorption index
k_0	Electromagnetic wavevector
l	Amplitude of a Lorentz oscillator
l_{acc}	Accumulation layer thickness
m^*	Effective electron mass
n	Refractive index
n_1	Constant of the linear wavelength scaling model
n_2	Constant of the linear wavelength scaling model
r_{rod}	Aspect ratio of a rod
r_{sph}	Aspect ratio of a spheroid
s	Interparticle gap
s	Stefan-Boltzmann constant
t	Time
ALD	Atomic layer deposition
AZO	Aluminium zinc oxide
CMOS	Complementary metal-oxide-semiconductor
CVD	Chemical vapour deposition
DBR	Distributed Bragg reflector
DTGS	Deuterium-doped triglycine sulfate
EBL	Electron beam lithography
ENZ	Epsilon-near-zero region
FDTD	Finite-difference time-domain
FE	Field enhancement
FEM	Finite-element method
FEP	Fluoro-ethylene polymer
FTIR	Fourier-transformed infrared reflectometry
IBE	Ion beam etching
IR	Infrared
ITO	Indium tin oxide
LCD	Liquid crystal display
LED	Light emitting diode
LSP	Localised surface plasmon
MMA	Methyl-methacrylate
OSR	Optical solar reflector
PECVD	Plasma-enhanced chemical vapour deposition
PLD	Pulsed laser deposition
PML	Perfectly matched layer
PMMA	Poly-methyl-methacrylate
RIE	Reactive ion etching

SERS	Surface enhance Raman spectroscopy
SMS	Spatial modulation spectroscopy
TCO	Transparent conductive oxide
UV	Ultraviolet
ZEP	Proprietary name, possibly Zeon e-beam photoresist

1 Introduction

Since the description of the scattering of colloidal particles by Gustav Mie in 1908 [1], the peculiar effects that occur at the interface between a metal and a dielectric have been a growing field of research. This field is called plasmonics, named after the quanta of electron oscillations in the metal, the plasmons. The unique property of plasmons is the ability to confine energy below the diffraction limit. This property is influenced by the surface-to-volume ratio of the metal, which increases for decreasing metal particle size and becomes significant on the nanometre scale. That is why the field of plasmonics is a sub-field of nanophotonics. Small metal particles in a dielectric environment convert incoming electromagnetic waves into localised near-fields, the so-called localised surface plasmons (LSP). The light confinement results in an enormous enhancement of the electric field in the vicinity of the metal particle. Among the many fascinating applications of plasmonics are metamaterials with unprecedented optical behaviours, sub-diffractional microscopy, resonant optical antennas and enhanced nonlinear optics. [2, 3]

The topic of this thesis is the electrical modulation of plasmonic structures and the development of novel devices for infrared applications based on transparent conductive oxides. The aim is to control the optical properties of plasmonic structures by applying an external bias. This external control would give a new degree of freedom to plasmonic application and allow for tunability of sensors, reflectors and metamaterials. It also enables information processing with light, an alternative to electronics providing lower losses (i.e. absorption) and larger bandwidths [4, 5]. Key elements for the transition from electronic to plasmonic data processing are electro-optic modulators, which are nanophotonic devices that convert electrical into optical signals. Realising them however imposes high demands on the fabrication processes involved. The precision of state-of-the-art nanofabrication tools such as atomic layer deposition (ALD) and electron beam lithography (EBL) are required to overcome surface roughness, alignment errors and material imperfections.

1.1 Plasmonic materials and applications

In its most fundamental way, plasmonics deals with the effects of electromagnetic waves at metal-dielectric interfaces. On a scale below the diffraction limit, the electromagnetic waves excite resonant oscillations of the quasi-free electrons, leading to strong field enhancements.

Depending on size, shape and material, plasmonic structures can be designed to be resonant to specific wavelengths, a property that opens a wide field of applications [6].

The strong field enhancements in plasmonics can be utilised to increase the optical signal from weakly scattering samples, e.g. in surface-enhanced Raman spectroscopy (SERS) [7–9]. Nonlinear optics, which depend on higher orders of the magnitude of the electric field, benefit from the enhanced fields [10]. Combining sub-wavelength sized particles into 2D and 3D lattices has opened up the field of metamaterials, with novel properties such as negative refractive index [11, 12] which can be used for invisibility cloaks [13]. Plasmonics is also a driving factor in optical communication, because it combines the advantages of photonics, such as up to petahertz speeds [14] and all-optical memory access [15], with sub-micrometre feature size. This enables ultra-small devices and promises to overcome current limitations of electronic data processing [4]. Carefully selecting the resonance conditions for plasmonic particles creates optical antennas that convert optical far-field information into the near-field and vice versa [2, 16, 17]. This can be used in many sensing applications such as detection of brain cell activity [18]. Further notable areas of research are dimer nanoantennas, which can be used for polarisation conversion [19, 20], the direct electrical addressing of nanoantennas [21, 22], and the anti-crossing of resonances upon the combination of antenna arms of different sizes [23] or materials [24]. The coupling between two antenna arms has also been a field of intense research [25, 26].

Most plasmonic applications are based on gold or silver. Another metal that has been considered for plasmonics is aluminium [27–29], which has the advantage that it can be used in the ultraviolet (UV) range. Applications for longer wavelengths however suffer from aluminium's intraband transition in the near-infrared (IR). Additionally, aluminium forms a few nanometre thick native oxide, which changes the plasmonic properties of the structure and can be disadvantageous in applications such as sensing [29]. Other metals that have been considered are nickel [30] and copper [27], which both have higher losses in the visible range than the noble metals. An alternative route to strong field enhancements is the use of high-index dielectric materials such as silicon, which can be used to imitate plasmonic behaviour [31, 32]. The high refractive index of 3.4 [33] allows scaling below the diffraction limit due to the reduced wavelength of the light, but it cannot compete with scaling factors of plasmonics (10 and higher). The advantage of dielectric resonators are the lower optical losses in dielectrics compared to metals [34].

1.1.1 Transparent conductive oxides

Historically, transparent conductive oxides (TCOs) have been used as transparent electrodes for liquid crystal displays (LCDs), light emitting diodes (LEDs) and solar cells [35–37]. Descriptions of the peculiar electro-optical properties of TCOs go back as far as 1968 [38, 39]. They are highly conductive, degenerate semiconductors that are transparent in the visible range. The most prominent representatives among these materials are ITO (indium tin oxide, actually tin-doped indium oxide) and AZO (Aluminium-doped zinc oxide).

Besides their application as transparent electrodes, TCOs have increasingly been implemented as a switchable medium with ultrafast response time [40–43] and high nonlinearity [44, 45]. Depending on doping, TCOs have a transition wavelength where their optical properties switch from dielectric to metallic behaviour, a spectral region which is called epsilon-near-zero (ENZ) due to the very small electric permittivity. In the ENZ region, TCOs influence the resonance of adjacent plasmonic structures by resonance pinning [46] and exhibit further enhanced nonlinearities [47, 48].

Materials with free electrons in the conduction band have a transition wavelength where their optical properties change from dielectric to plasmonic. While traditional plasmonic materials such as noble metals allow plasmonic resonances for short wavelengths (due to their high carrier concentrations of over $10^{22}\,\mathrm{cm}^{-3}$), TCOs act as dielectrics in the visible range. Due to their transition wavelengths being in the near-IR to mid-IR, TCOs can exhibit plasmonic behaviour in the infrared spectral range, and consequently plasmonic applications have been demonstrated [49–51]. A key potential of TCO plasmonics is the higher antenna density that can be achieved due to low inter-particle coupling, which has been used to demonstrate surface-enhanced IR spectroscopy [52]. Noble metals are also not compatible with CMOS (complementary metal-oxide-semiconductor) technology since they tend to diffuse into semiconductors. TCOs do not suffer from this limitation.

Specific TCO properties such as the transition wavelengths depend mainly on the carrier concentration of the material. This is subject to doping, reaching from $10^{19}\,\mathrm{cm}^{-3}$ to $10^{21}\,\mathrm{cm}^{-3}$, and can be controlled both by the main dopant of the material (Sn for ITO, Al for AZO) and by the amount of oxygen vacancies in the lattice. Especially the latter depends strongly on the chosen deposition method, and studies have been performed for sputtered ITO [53–57] and AZO [56–60], pulsed laser deposited (PLD) ITO [37, 61, 62] and AZO [61–63], chemical deposition of ITO [64, 65] and AZO [66], evaporated ITO [39, 53, 67] and AZO [68], as well as post-deposition treatments of commercial ITO [69, 70]. Summarising these references, it can be said that ITO and AZO perform optically in a similar manner if the carrier concentration is the same. For the same deposition method, AZO sometimes has higher or lower carrier concentrations than ITO, and the same goes for optical losses. More important than the deposition method and the dopant concentration, for which a theoretical model was established [71], seem to be the atmospheric conditions during deposition, particularly the oxygen flow and partial pressure. The only difference between ITO and AZO is that AZO is not based on a rare metal and has therefore the prospect of being a cheaper substitute of the currently widely used ITO.

Another advantage of AZO is that it can be deposited via ALD [72], a chemical vapour deposition variant where one atomic layer after the other is formed on the substrate, offering sub-nanometre control of material deposition. ALD of AZO has been studied in the last two decades, showing a similar spread of reported values for conductivity and carrier concentration as the other deposition methods [36, 73–76]. The DC-conductivity of TCOs can be as low as $10^{-6}\,\Omega\,\mathrm{cm}$ and the carrier concentration up to $1.4 \times 10^{21}\,\mathrm{cm}^{-3}$.

1.1.2 Titanium nitride

The standard metals for plasmonic structures are gold and silver, the former because it is inert and does not degrade, the latter because it has the lowest optical losses at visible frequencies. As mentioned above, these materials are not CMOS-compatible, and TCOs cannot substitute them for visible wavelength applications. An alternative currently proposed antenna material is titanium nitride (TiN), which is a hard ceramic that does not diffuse into silicon. Due to its high carrier concentration similar to that of noble metals, it supports plasmonic resonances for shorter wavelengths than TCOs, though it exhibits higher optical losses than the noble metals [77–80]. Therefore, TiN has been used in plasmonic nanostructures with resonances in the visible and near-infrared [77, 81] and as a nonlinear material [45].

1.2 Electrically modulated devices

The modulation of the optical properties of plasmonic structures is a field that gained much interest in the last decade. Since plasmonic structures can nowadays be fabricated with sufficient reliability so that their optical properties are well known, the modulation of these properties allows modulation of an optical data stream by external controls of an optical, electric or thermal nature. All-optical control has been demonstrated by pump-probe experiments where a pump beam depletes the carriers of a TCO, thereby changing its refractive index. Plasmonic structures allow the resonant enhancement of the carrier depletion and accelerate it into the ultrafast femtosecond regime [40–43]. While these experiments have shown the potential of TCO-based modulators, all-optical setups have not yet been demonstrated as compact, integrated modulators. Electrical modulation however has been recognised as a low-power, scalable modulation technique that has the potential to create large refractive index changes in a nanometre-thin layer, as described in the pioneering work of Feigenbaum et al. [82]. The device that was used for optical characterisation of the ITO refractive index is shown in Fig. 1.1(a). The work enabled the theoretical design [83–88] and experimental realisation [89–92] of electro-optical absorption modulators using a thin MOS structure on top of a silicon waveguide (see Fig. 1.1(b)). The device enables electrical-to-optical data conversion and is therefore a key element in the transition from electronic to photonic circuits [4].

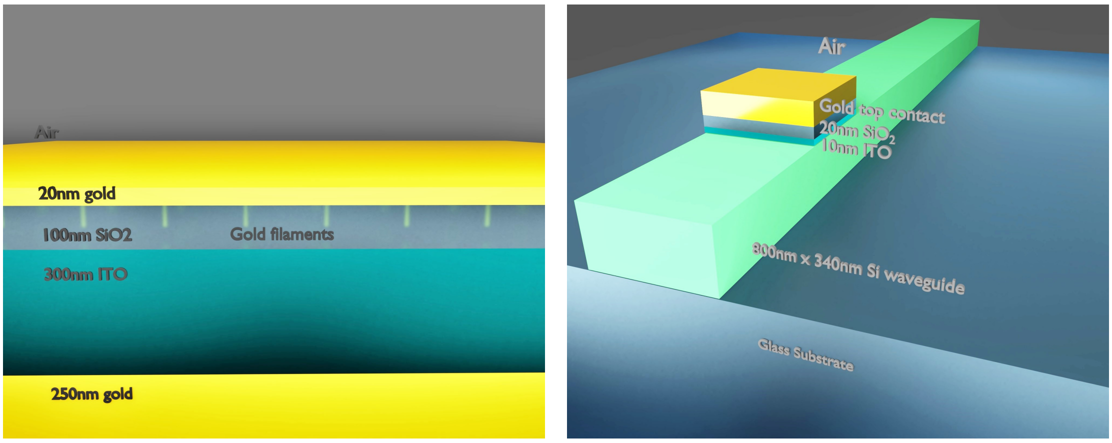

(a) **(b)**

Figure 1.1: (a) 3D-representation of the device by Feigenbaum et al. [82] of a sandwich structure with $300\,\mathrm{nm}$ of ITO and $100\,\mathrm{nm}$ of SiO_2 between two gold electrodes, over which a voltage is applied. (b) Application of the device in (a) onto a waveguide as done by Sorger et al. [91]. The silicon waveguide is used as the bottom electrode.

1.2.1 Electrical insulators

For the electrical modulation of plasmonic structures, an electric field is applied over an insulator by an external voltage. In semiconductor technology it is common to use silica (SiO_2), which is easy to fabricate from silicon by thermal annealing. However it has a comparably low static permittivity of $\kappa = 3.9$ and, depending on the deposition technique, low breakdown voltages [93, 94]. Alternative materials with a high breakdown voltage and a high static permittivity are for example alumina (Al_2O_3), silicon nitride (Si_3N_4) and hafnia (HfO_2), the latter being especially promising due to its static permittivity of $\kappa = 25$ [93, 95]. Al_2O_3 and HfO_2 can also be deposited by ALD, which creates smooth, pinhole-free layers with high breakdown voltages [96, 97].

1.2.2 Waveguide-based plasmonic absorption modulators

The first demonstrated modulator by Dionne et al. [89] used the silicon waveguide itself as the modulated semiconductor, while later works used an ITO sheet on top of the waveguide [90–92]. The carrier modulation increases the refractive index of the top layer, which redistributes the mode energy so that more light is guided by the ITO, which has significantly higher losses than the waveguide. This creates absorption modulation in the waveguide, and good on-off ratios of 1–2 dB/µm have been demonstrated [91]. A disadvantage of these devices remain the high intrinsic losses of the structure, which result in noticeable absorption in the on-state. Additionally, absorption modulation is generally undesirable in this application since the energy is lost to heat. A different approach was shown by the presentation of a phase modulator by Melikyan et al. [98], where the energy stays constant, but the phase is flipped by 180°. This approach is generally preferred in telecommunications as in other fields of nanophotonics, since losses always create heat that needs to be dissipated. However this structure also suffered from high propagation losses compared to non-plasmonic modulators.

A different approach is suggested by the use of vanadium dioxide (VO_2) as the modulated medium. VO_2 is a phase-change material that changes from dielectric to metallic behaviour if its crystallinity is changed. The change can be induced by either thermal heating, optical pumping or an electric field [99]. The change in the optical properties is much larger than in carrier-modulated TCOs and corresponds roughly to accumulating charge carriers to a density of $10^{22}\,\mathrm{cm}^{-3}$ in the material. Additionally, it occurs in the bulk of the material, providing higher overlaps with optical fields. However the effect in optical modulators, as proposed, is currently more power-consuming than for TCOs [100, 101].

It is notable that the initially reported findings by Feigenbaum et al., which are largely responsible for the surge in work on electro-plasmonic modulators, are difficult to reproduce. Particularly the amount of carriers moved ($2.7 \times 10^{22}\,\mathrm{cm}^{-3}$) and the thickness over which carriers accumulated ($5\,\mathrm{nm}$) disagree with what numerical simulations, as well as simple analytical approaches such as Thomas-Fermi screening theory [94], suggest. For the presented structure with a $100\,\mathrm{nm}$ of SiO_2, over which a voltage of $2.5\,\mathrm{V}$ is applied, Thomas-Fermi screening theory gives a carrier concentration change of only $10^{17}\,\mathrm{cm}^{-3}$ over a thickness of $0.6\,\mathrm{nm}$ (see chapter 3 for details). The reduced amplitude and active volume imply that the effect of the actual charge distribution on an optical near-field is six orders of magnitude smaller than what would be expected based on the reported numbers. Now Feigenbaum et al. used a special structure with gold filaments penetrating the insulator, thereby increasing the structure's capacitance to a larger value, but the sheer discrepancy of several orders of magnitude between experimental findings and analytical formula demands caution. Also filaments inside an insulator pose an additional challenge, which is the one of short-circuiting the SiO_2, because the filaments can grow under an applied bias [102]. Indeed, short-circuiting by filament growth could be the actual reason for the large change in optical properties that Feigenbaum et al. reported. This is a mechanism that was recently quantified by the group of Juerg Leuthold and utilised in the demonstration of plasmonic switches [102], since a grown filament provides a non-volatile optical state. Going one step further, the group demonstrated an atomic scale plasmonic switch based on the controlled growth and shrinking of a silver filament by a single atom [103]. Whether this mechanism is the same as in the device employed by Feigenbaum et al. cannot ultimately be determined.

1.2.3 Tunable metasurfaces

Metasurfaces are a 2D version of metamaterials and have applications as ultrathin lenses and in energy harvesting [32, 104, 105]. One application for metasurfaces are metamaterial perfect absorbers, which are basically reflectors that, for a certain wavelength, create a standing wave between the incoming and reflected light with a maximum at the location of an absorbing metamaterial [106–112]. The metamaterial is designed as a plasmonic structure with a broad or narrow resonance, depending on the application. The constructive interference increases the total absorption at a certain wavelength range to up to 100%.

Tunable metasurfaces allow the electrical tuning of the device's reflection and absorption, and beam-steering. A significant amount of research has gone into this field in the last five years, using several different approaches to obtain tunability. The first experimental demonstration was done in 2013 by Yi et al. [113] with an ITO-covered gold grating on Si_3N_4. They demonstrated a relative shift of the absorption peak of $10\,\mathrm{nm}/4.3\,\mu\mathrm{m} = 0.2\%$ with an electric field of $0.1\,\mathrm{V\,nm^{-1}}$. The low carrier concentration of the used ITO of $9 \times 10^{19}\,\mathrm{cm^{-3}}$ does not allow for stronger modulation, and the relative change in absorption remains negligible.

Researchers in the group of Pierre Berini have demonstrated a tunable metasurface using p-doped silicon as modulatable material [114, 115], however their optical data consists of simple voltage-time-curves from their photodiodes with significant noise. Their papers can therefore not be analysed in terms of reflectivity or extinction cross-section. The group of Federico Capasso [116] has used graphene successfully as a modulatable material, however graphene is difficult to produce and to combine with metals and semiconductors.

The most promising results for tunable metasurfaces come from the groups of Mark Brongersma [117, 118] and Harry Atwater [119]. Brongersma's group designed an ITO-based modulator where two resonances interfere once the ITO is depleted of carriers. This enabled a relative reflection (R) modulation of $\Delta R/R = 35\%$ at $4\,\mu\mathrm{m}$, while both resonances where shifted about 20% of the resonance wavelength. The applied electric field was $0.4\,\mathrm{V\,nm^{-1}}$ and the insulator HfO_2. Atwater's group used a very similar structure, but with Al_2O_3 as the insulator and a measured resonance at the telecom wavelength of $1550\,\mathrm{nm}$. The applied electric field was $0.5\,\mathrm{V\,nm^{-1}}$. They obtain $\Delta R/R = 30\,\%$ and a resonance shift of 1.6%. The lower value for the resonance shift is mainly ascribed to the short resonance wavelength, which makes wavelength shifts significantly more challenging.

Peculiar to the research of tunable metasurfaces is the low number of purely simulation-based literature proposing device designs, such as a recent article [120] which proposes an InSb-based metasurface for mid-IR modulation at $11\,\mu\mathrm{m}$. A possible reason is the challenge in combining electrical and optical simulations that accurately model the near-field and carrier distributions on the nanoscale. From the above-mentioned literature of tunable meta-surfaces, only reference

[119] uses such an electro-optical model. The other groups model their carrier distributions as single layers via step functions [115, 120] or as bulk properties [117], which prevent direct comparison of the simulated and experimental results.

The ‘unity order refractive index change’ that was promoted by Feigenbaum et al. was achieved by the latest tunable designs, as well as in the devices demonstrated in this thesis, however only for high-performance dielectrics and for significantly larger electric field strengths than initially reported.

1.3 Outline of the thesis

This thesis gives a comprehensive description of the author’s work on electrically tunable and mid-infrared devices using transparent conductive oxides. The first step in designing a device for electrical modulation of plasmonic structures is an extensive theoretical description of plasmonic resonances and their properties, which is presented in chapter 2. The theory is compared to other analytical formulas available in the literature [121, 122] and utilised to determine necessary parameters to enable successful electrical modulation. Chapter 3 deals with the the deposition and patterning tools used for fabrication, such as ALD, evaporation tools, EBL and etching are described, as well as the following characterisation tools: ellipsometry, spatial modulation microscopy (SMS), Fourier-transformed infrared reflectometry (FTIR), scanning electron microscopy (SEM) and atomic force microscopy (AFM). Additionally, the chapter contains a description and comparison of the software used for numerical simulations, Lumerical FDTD and DEVICE, and COMSOL Multiphysics.

This is followed by the simulation work done within the framework of this thesis. Chapter 4 deals with the simulation-based design of an optical solar reflector using a 2D AZO metasurface showing high reflectance in the visible range and high absorption in the mid-IR. In chapter 5, a novel electro-optical simulation model of the nanoscale interactions of an electric charge distribution with an optical near-field is used to design a highly efficient electro-plasmonic modulator. The design relies on the gap-loading of an antenna with ITO, a method which is experimentally investigated in chapter 6.1. It describes the fabrication and characterisation of ITO gap-loaded gold nanostructures, as well as work on the fabrication of TiN optical resonant antennas. The penultimate chapter 7 shows the fabrication and electro-optical characterisation of a device with electrically tunable nanoantennas. The electrical modulation of the optical properties of the device is successfully demonstrated. A final chapter, summarising the work and giving an outlook, concludes this thesis.

2 Analytical description of plasmonic resonances

This chapter describes the fundamental theory that underlies the charge-carrier-based modulation of plasmonic structures. After describing basic material properties and how they change with changing carrier concentrations, the theory of plasmons at metal-dielectric interfaces is laid out. The first analytical description of plasmonic resonances was done by by Gustav Mie [1] for spherical metal nanoparticles in 1908. Mie theory is the only analytical description that includes the full scaling of the plasmonic resonance with increasing particle size. Depending on the size of a particle, the electrons inside the particle can be excited in different orders of resonances, such as dipolar, quadrupolar, hexapolar etc. In Mie theory, this is done by calculating the sum of the contributions of a number of higher order resonances, depending on the wavelength of the incoming light and the particle size. Since spherical nanoparticles are of small interest in the framework of this thesis, basic Mie theory will not be regarded in this chapter. Elongated particles represent the fundamental building block of nanoantennas, and for those only the dipolar resonances can be fully described analytically [123]. Extensions to the dipolar description of elongated particles have been proposed [124, 125], however in this chapter we will use the basic dipolar approach to minimise the use of approximations. In this thesis, numerical simulations will ultimately be the tool to model electro-plasmonic modulation, and the analytical theory only used to obtain qualitative information about the properties and limitations of the modulation method.

2.1 Material parameters

Plasmonic resonances and resonance shifts are dominated by the relative permittivities, ε_r, of the particle and the surrounding medium, which determine their optical behaviour. If the real part of the permittivity, ε_r', is negative, the material behaves like a metal, i. e. strongly reflective. If on the other hand it is positive, the material behaves like a dielectric with low reflection. Absorption, or optical losses, arises from the imaginary part of the permittivity, ε_r''. The refractive index is connected to the permittivity by $\tilde{n} = n + jk = \sqrt{\varepsilon_r}$.

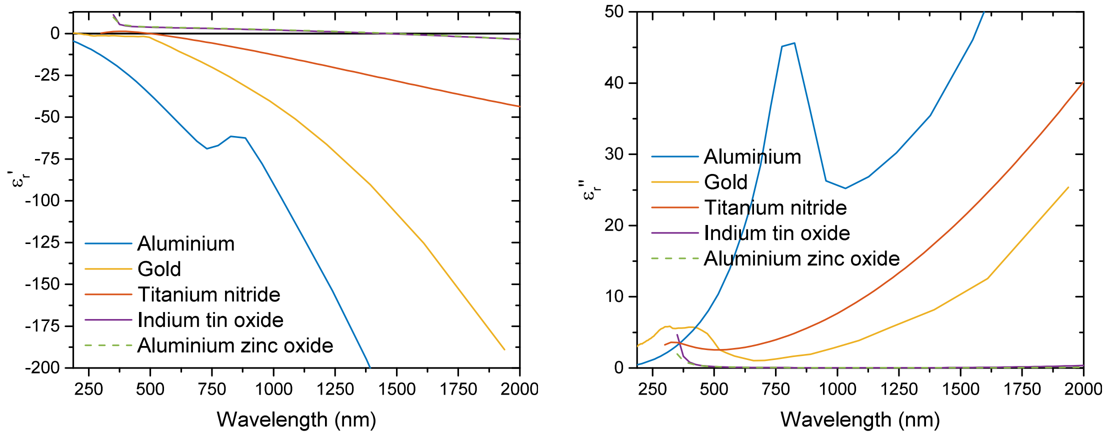

(a) **(b)**

Figure 2.1: (a) Real part and (b) imaginary part of the permittivity of plasmonic materials. Aluminium and gold are experimental data, TiN, ITO and AZO from their Drude-Lorentz models. Experimental values taken from reference [126] (Al) and [127] (gold); Drude-Lorentz data from reference [62].

2.1.1 Drude and Lorentz model

In the visible and infrared regime, materials are typically described by the Drude model. It assumes a free electron gas in the material to describe its response to an incoming electromagnetic wave [6]:

$$\varepsilon_r(\omega) = \varepsilon_\infty - \frac{\omega_p^2}{\omega^2 + \Gamma^2} + j\frac{\omega_p^2\Gamma}{\omega(\omega^2 + \Gamma^2)}. \tag{2.1}$$

The electrical permittivity of a material at a certain angular frequency, ω, depends on the permittivity at large frequencies, ε_∞, the plasma frequency, ω_p, and the scattering constant, Γ, the latter two being given by [6, 55]:

$$\omega_p^2 = \frac{Ne^2}{m^*\varepsilon_0} \qquad \text{and} \qquad \Gamma = \frac{e}{m^*\mu}, \tag{2.2}$$

where N is the carrier concentration, m^* the effective electron mass, ε_0 the permittivity of vacuum, e the electron charge and μ the electron mobility.

This model is valid as long as no interband or intraband transitions occur in the material and within the classical regime. Most metals exhibit band transitions in the UV and partially in the visible range, but can be described by the Drude model for longer wavelengths. For gold and silver, this is the case for wavelengths longer than $500\,\mathrm{nm}$ and $300\,\mathrm{nm}$, respectively. Band

Table 2.1: Table of Drude parameters for different materials from a fit to experimental literature data [126] (Al), from reference [121] (gold), reference [62] (TiN, ITO, AZO) and a fit to experimental data (VO_2). All data except VO_2 at room temperature.

Material	ε_∞	ω_p (eV)	λ_t (nm)	Γ (eV)	Γ (µm)	N (cm^{-3})
Aluminium	1.0	15.0	82	0.08	14.9	18.0×10^{22}
Gold	11.0	9.0	458	0.07	18.8	5.9×10^{22}
TiN	2.5	5.9	328	0.51	2.4	5.9×10^{22}
ITO	3.5	1.8	1308	0.16	8.0	9.0×10^{20}
AZO	3.5	1.7	1335	0.05	27.5	8.0×10^{20}
VO_2 (84°C)	5.5	3.1	930	1.03	1.2	2.8×10^{21}

transitions can be described by adding Lorentz peaks to the electric permittivity [62]:

$$\varepsilon_r(\omega) = \frac{l\omega_l^2}{\omega_l^2 - \omega^2 - j2\omega\Gamma_l}, \tag{2.3}$$

where l, ω_l and Γ_l are the amplitude, the spectral position and the damping of the Lorentz oscillator, respectively. Aluminium for example features an interband absorption at $800\,\mathrm{nm}$, where its ε_r'' exhibits a local maximum.

The Drude parameters of gold, aluminium, TiN, ITO and AZO are listed in table 2.1. The parameters for aluminium and gold are a combination of the values from references [6] [121], the others from [62]. While gold and TiN commonly have very high carrier concentrations of around $5 \times 10^{22}\,\mathrm{cm}^{-3}$ [6, 78], the carrier concentrations of TCOs depend on the fabrication method and dopant concentration. Assuming an average effective electron mass of $m^* = 0.4$ for ITO [55] and $m^* = 0.35$ for AZO [60], the carrier concentrations corresponding to the data from reference [62] can be calculated using equation 2.2. They are also given in table 2.1 and are two orders of magnitude lower than the carrier concentrations of the listed metals. Values from a Drude model fit to experimental VO_2 data are also listed, showing a high carrier concentration of heated VO_2. The thermal switching allows a surpassing modulation of the carrier concentration, since VO_2 acts like a transparent dielectric of negligible carrier concentration at room temperature. A drawback of the mechanism are the optical losses from the high scattering constant compared to ITO and AZO.

The real and imaginary parts of the permittivity resulting from these parameters are plotted in figure 2.1. It can be seen that the different materials show drastically different behaviour and change their permittivity strongly over the wavelength range. In general, metals show a lower ε_r' than TCOs, but also have significantly higher optical losses. AZO and ITO behave very similar, with small differences in the bandgap response and slightly lower losses for the presented AZO. TiN plays an intermediate role, with ε_r' between TCOs and gold, but high optical losses. For the

Drude plot of VO_2, see chapter 4.

Table 2.1 shows that the values of Γ_i correspond to wavelengths in the infrared. In the analytical derivations, we can therefore make a simplification by assuming that Γ[eV] $<<$ ω[eV], which will be used in the following. The optical behaviour of the materials is determined by the carrier concentration (N) and the material's electron configuration (ε_∞ and m^*). As a result, the transition from dielectric to metallic behaviour ($\varepsilon_r' = 0$) occurs at different wavelengths. The spectral location of that transition can be calculated by:

$$\lambda_t = 2\pi \frac{c_0}{\omega_p} \sqrt{\varepsilon_\infty}, \tag{2.4}$$

where $c_0 = 3 \times 10^8\,\mathrm{m\,s^{-1}}$ is the speed of light in vacuum [6]. The transition wavelength also defines the position of the range where the permittivity (epsilon) is near zero (ENZ), i.e. $1 > \varepsilon_r' > -1$. Combining equation 2.4 and 2.2, it can be seen that $\lambda_t \propto 1/\sqrt{N}$, which shows that to move a TCO's ENZ region into the visible range, the carrier concentration has to be quadratically increased. For comparison, λ_t is also given in table 2.1. Due to their short transition wavelengths, aluminium, gold and TiN show metallic behaviour in the visible regime, whereas ITO and AZO show dielectric behaviour up to the near IR. This and their low losses are the reasons why TCOs are optically transparent.

Looking at the experimental data of gold in Fig. 2.1, it can be seen that the real part of the permittivity has a step at $500\,\mathrm{nm}$ due to interband transitions at shorter wavelengths. Concomitantly, the imaginary part, as for several other materials at the short wavelength side, shows an increase that does not follow the Drude model, which assumes proportionality of the electron scattering with wavelength. The Drude model for gold is therefore only valid for wavelengths greater than $500\,\mathrm{nm}$. This has to be taken into account when modelling the behaviour of gold nanoparticles in the visible range. ITO and AZO show UV bandgaps, which are in this case modelled with a single Lorentz peak [62].

2.1.2 Dependency of the permittivity on the carrier concentration

With the assumption Γ[eV] $<<$ ω[eV], equation 2.1 simplifies to [6]:

$$\varepsilon_r(\omega) = \varepsilon_\infty - \frac{\omega_p^2}{\omega^2} = \varepsilon_\infty - \frac{Ne^2}{m^* \varepsilon_0} \frac{1}{\omega^2}. \tag{2.5}$$

It follows that ε depends linearly on the carrier concentration N and that the slope can be calculated as:

$$\frac{\partial \varepsilon'}{\partial N} = -\frac{e^2}{\varepsilon_0 m^*} \frac{1}{\omega^2}. \tag{2.6}$$

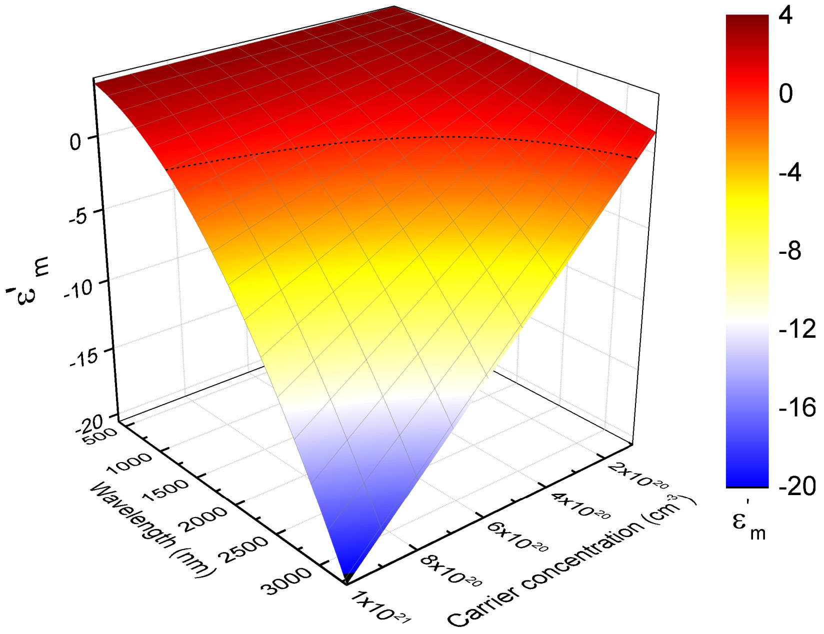

Figure 2.2: Dependency of ε_r' of ITO on the carrier concentration and wavelength. Data based on equation 2.6 using numerical values from reference [55].

This proportionality can be seen in figure 2.2, where the permittivity of ITO is plotted for a list of different carrier concentrations using equation 2.6. The dotted line depicts ENZ region of ITO, separating the range where ITO is optically dielectric from the range of long wavelengths and high carrier concentrations where ITO is optically metallic. A plot for the refractive index as a function of carrier concentration, including real and imaginary parts, can be found in reference [40], figure 2(a).

2.2 Analytical derivation of plasmonic resonances

2.2.1 Elongated particles

As particles, we consider prolate spheroids (or ellipsoids by revolution) which are much smaller than the wavelength. The shape is schematically shown in Fig. 2.3(a). As long as $a << \lambda/10$, with a being the largest dimension of the particle, we can describe the particle's optical response solely by their dipolar resonance. This approximation is known as dipole approximation or quasistatic approximation, and its application to the optical response of elongated metallic particles as Mie-Gans theory.

In the case of small particles, it is important to check if the Drude model is still valid, i.e. that surface scattering is negligible compared to the bulk response. This depends on the material under investigation. For gold, this is true as long as the smallest dimension is larger than $17\,\mathrm{nm}$ [128].

If the particles contain a free electron gas, it will be able to be excited by an incoming electromagnetic wave, leading to plasma oscillations. The plasma oscillation will lead to localised surface plasmon resonances if the so-called Fröhlich condition is met [6]:

$$|\varepsilon_{np} + \frac{1-g}{g}\varepsilon_m| \longrightarrow 0, \tag{2.7}$$

where g is the geometrical factor along the longitudinal axis of a prolate spheroid, and ε_{np} and ε_m designate the relative permittivity of the nanoparticle and the surrounding medium, respectively. The longitudinal resonance is of main interest in this work. It depends on the aspect ratio r_sph of the particle's long and short axes a and b [123]:

$$g = \frac{1-f^2}{f^2}\left(-1 + \frac{1}{2f}\ln\frac{1+f}{1-f}\right), \qquad f^2 = 1 - \frac{1}{r_\text{sph}^2} \qquad \text{and} \qquad r_\text{sph} = \frac{a}{b}. \tag{2.8}$$

Since for the three axes $g + g_2 + g_3 = 1$, it follows that for a sphere $g = 1/3$, as can also be obtained from equation 2.8 for $f^2 \to 0$. The other boundary of g is 0 for $f^2 \to 1$.

If both permittivities are complex, equation 2.7 becomes:

$$\sqrt{\left(\varepsilon'_{np} + \frac{1-g}{g}\varepsilon'_m\right)^2 + \left(\varepsilon''_{np} + \frac{1-g}{g}\varepsilon''_m\right)^2} \longrightarrow 0, \tag{2.9}$$

where ε'_i is the real part and ε''_i the imaginary part of the permittivity. This equation can only become zero under the following conditions:

- The real parts of the permittivities have opposite signs, as is the case in a metal-dielectric combination.

- The imaginary parts have opposite signs, as would be the case if one of the materials had gain.

Since in the scope of this work, materials with gain will not be considered, equation 2.9 can never be exactly zero. The plasmonic resonance is in this case defined as the wavelength where equation 2.9 obtains a minimum. The strongest plasmonic resonance occurs for the dipole resonance, which is the fundamental excitation of the electron plasma. In the following parts, the properties of the dipole resonance will be derived and discussed.

Assuming that the imaginary part is small ($\varepsilon''_i << \varepsilon'_i$) and that its slope is flat $\left(\frac{\partial\varepsilon''_i}{\partial\lambda} << \frac{\partial\varepsilon'_i}{\partial\lambda}\right)$, it is sufficient to analyse equation 2.9 for the real part of the materials' permittivities in order to

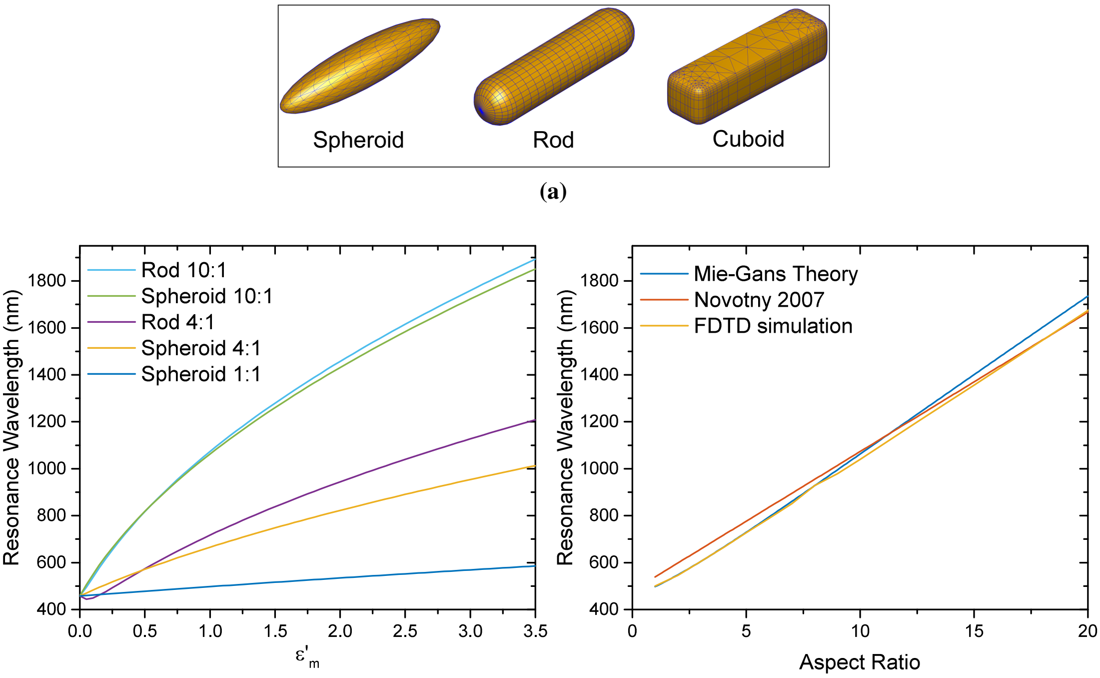

(a)

(b) **(c)**

Figure 2.3: (a) Schematics of the three different shapes discussed in this chapter. Resonance wavelength of gold nanoparticles as a function of the surrounding medium's permittivity and the particle shape. (b) Analytical solutions of spheroids and rods using equation 2.12 and equation 2.13 respectively; (c) 'Linear wavelength scaling' of the resonance wavelength of gold nanoparticles with aspect ratio. Plotted are the results of Mie-Gans theory for spheroids, Novotny's paper for rods (reference [121]) as well as simulations with Lumerical FDTD for cuboids. The surrounding medium is air ($\varepsilon'_m = 1$).

obtain the resonance wavelength. Equation 2.9 then simplifies to:

$$\varepsilon'_{np} = -\frac{1-g}{g}\varepsilon'_m. \tag{2.10}$$

Using the Drude model from section 2.1.1 to describe the particle's permittivity, equations 2.5 and 2.10 can be combined to:

$$\omega_{res} = \frac{\omega_{p,np}}{\sqrt{\varepsilon_{\infty,np} + \frac{1-g}{g}\varepsilon'_m}}. \tag{2.11}$$

The resonance wavelength can be obtained by [6]:

$$\lambda_{res} = 2\pi\frac{c_0}{\omega_{res}} = 2\pi\frac{c_0}{\omega_{p,np}}\sqrt{\varepsilon_{\infty,np} + \frac{1-g}{g}\varepsilon'_m}. \tag{2.12}$$

Figure 2.3(b) shows the resonance wavelength of gold particles versus the real part of the permittivity of the surrounding medium. For a sphere, the factor in equation 2.12 becomes $\frac{1-g}{g} = 2$, as is well known in literature. With increasing aspect ratio, this factor increases, and reaches infinity for an infinitely long wire. The impact of this can be seen in equation 2.10, where, compared to the spherical case, $|\varepsilon'_m|$ is weighted stronger and the resonance is shifted towards frequencies where $|\varepsilon'_{np}|$ is larger. As can be seen in the Drude model plots (figure 2.1), larger $|\varepsilon'_{np}|$ is given at longer wavelengths. Therefore, compared to the spherical case, the elongated particles experience pronounced red-shifts. From a physics point of view, this corresponds to the electric dipoles excited in the metal interacting more strongly, and thus for the plasmon to being more sensitive to the surrounding medium. The amount of red-shift experienced due to elongation depends on the slope of the permittivity $\partial|\varepsilon'_{np}|/\partial\lambda$, and the same holds for red-shifts due to an increase of ε'_m. For small ε'_m, all resonance wavelengths approach λ_t, which comes from the fact that in equation 2.12, $\lambda_{\text{res}} = \lambda_t$ when $\varepsilon'_m = 0$.

Before comparing the analytical model with numerical results, another prominent analytical model from the literature is investigated. In reference [121], Lukas Novotny described a model for $\lambda/2$-rod antennas with variable aspect ratios $r_{\text{rod}} = L/(2R)$. The rods of total length L consist of a cylinder of radius R and two hemispheres as end caps. Starting from the Drude model, he assumed optically thin wires ($R << \lambda$), neglected the losses of the antenna material and used further not explicitly stated approximations. In the end he arrives at:

$$\lambda_{res} = 2\pi \frac{c_0}{\omega_{p,np}} \left[\sqrt{\varepsilon_{\infty,np} + 141\varepsilon_m} + \left(\frac{2r_{\text{rod}}}{\pi} - 13.1 \right) \frac{\varepsilon_m}{0.12\sqrt{\varepsilon_{\infty,np} + 141\varepsilon_m}} \right]. \quad (2.13)$$

Comparing this equation with equation 2.12, it becomes apparent that the first part of Novotny's formula equals equation 2.12 for $\frac{1-g}{g} = 141$, which corresponds to an aspect ratio of 20:1. The second part of the equation is scaling linear with the aspect ratio of the particle. This is based on the often-stated 'linear wavelength scaling' of optical antennas, which is also stated in reference [121]:

$$\lambda_{res} = n_1 L + n_2, \quad (2.14)$$

where n_1,n_2 are constants and L is the total length of the considered particle (a for spheroids). It can be seen that these constants depend on the materials used as well as the aspect ratio of the rods. That means that for different particle materials or shapes the constants have to be adjusted. Additionally, the linear scaling is only an approximation of the exact length dependency of the resonance position. Equation 2.13 is plotted in figure 2.3(b) together with the results from spheroids. The rods also experience a red-shift compared to the spherical case. For large aspect ratios, the analytical functions for spheroids and rods are near equal. For small aspect ratios however, the discrepancy is large.

To better judge the differences between Novotny's model and Mie-Gans Theory, the scaling of the particle resonance as function of the aspect ratio is given in Fig. 2.3(c). Numerical FDTD simulation results for a $25 \times 10 \times 10\,\mathrm{nm}^3$ rectangular antenna, modelled with a mesh size of $0.1\,\mathrm{nm}$, are shown as well. Since larger aspect ratios give more weight to the surrounding medium's permittivity ε'_m, the resonance red-shifts compared to the spherical case. The apparently linear behaviour comes from the shape of the particle material's Drude model, which is approximately linear for wavelengths longer than λ_t (see Fig. 2.1). For short aspect ratios, the graph is slightly curved, which the Mie-Gans model captures correctly. It can be seen that in general the model agrees surprisingly well with the numerical results, even though the particle shape differs. For aspect ratios above 5, the Mie-Gans theory shows a linear scaling similar to that of Novotny's model. However the slope of Novotny's model is lower than that of Mie-Gans theory. Comparison with the FDTD results reveals that while, for aspect ratios below 10, Mie-Gans theory agrees near exactly, above 10 the numerical results rather follow the line of Novotny's model, indicating that Mie-Gans theory must be less suitable for these large aspect ratios. Since Novotny's model is a mere fit to the behaviour at an aspect ratio of 20, it makes sense that it agrees well with numerical results at that size.

Further aspects of the exact scaling of rod antennas were investigated in reference [122] by Bryant et al. From boundary element modelling, they found that the wavelength scaling factor n_1 is 2.5 for large particles instead of the expected 2 for a $\lambda/2$-resonance, whereas for small particles within the dipole approximation, the slope is higher than 5. This matches the slope in Fig. 2.3(c) and the observation that Novotny's linear model does not match well with small aspect ratio particles. Another finding in reference [122] is that the resonances depend largely on the absolute value of the transverse dimension b and not just on the aspect ratio, even if the particles are well below $\lambda/10$. The discrepancy from the dipole approximation includes the numerical nanoantennas with $b = 10\,\mathrm{nm}$ with aspect ratios above 5. This finding disagrees with the observations made from the numerical results here, which agree excellently with the dipole approximation up to aspect ratios of 10. More simulations are needed to conclusively compare the accuracy of the three approaches, dipole approximation, linear scaling and numerical modelling.

In the work performed for this thesis, the maximum aspect ratio of fabricated nanoantennas is 8. Fabricated nanoantennas are designed with a rectangular shape throughout, and as was shown, Mie-Gans Theory for spheroids agrees well with FDTD simulations for this shape. The simulation work of reference [129] supports the statement that the shape, be it spheroid, rod or cuboid, has a small influence on the resonance shift. For these reasons, the formula from Novotny will not be considered further in this thesis.

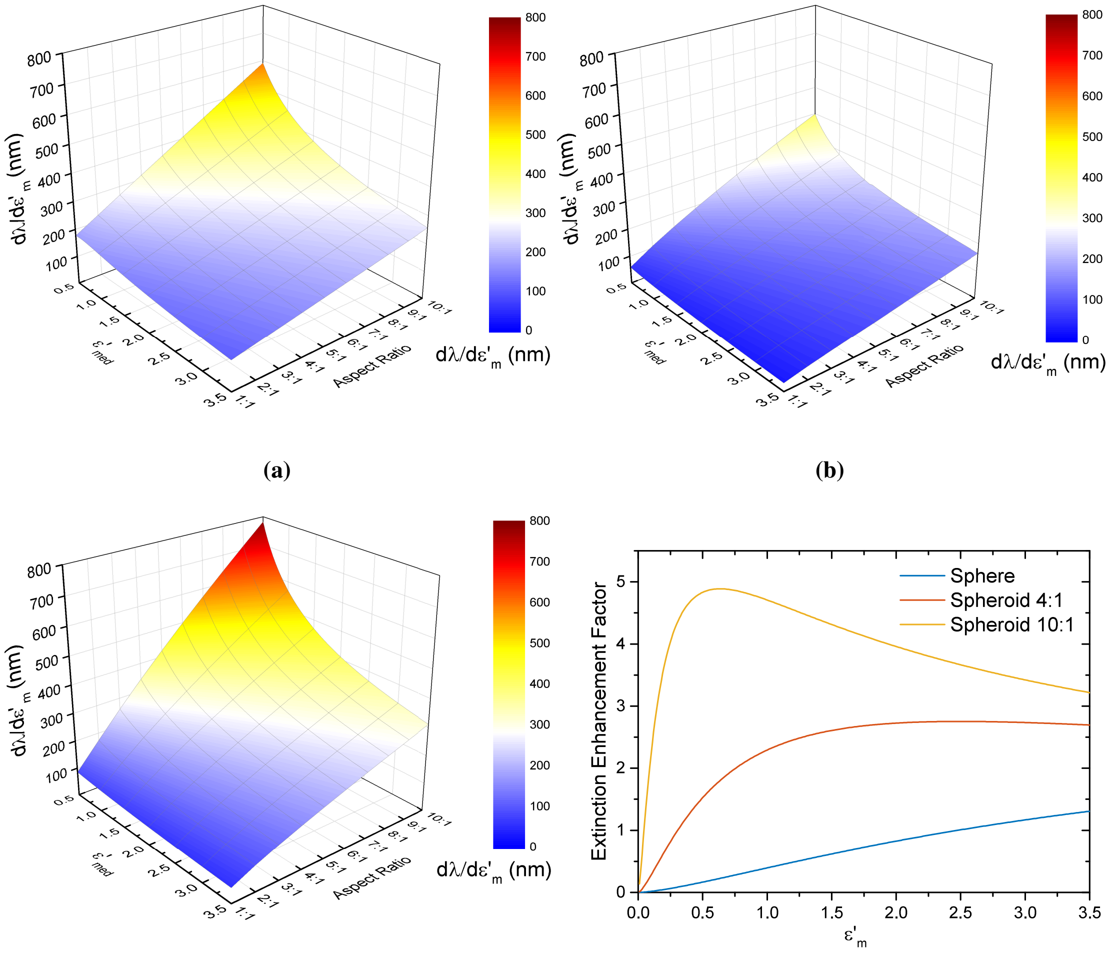

(a) **(b)**

(c) **(d)**

Figure 2.4: Dependency of the plasmonic resonance wavelength shift on the aspect ratio and the permittivity of the surrounding medium for (a) gold, (b) aluminium and (c) TiN nanoparticles. (d) Amplitude of the extinction enhancement factor at resonance as a function of the permittivity of the surrounding medium.

2.2.2 Dependency of plasmonic resonances on the permittivity

By differentiating equation 2.12 with respect to ε'_m, it follows that:

$$\frac{\partial \lambda_{res}}{\partial \varepsilon'_m} = 2\pi \frac{c_0}{\omega_{p,np}} \cdot \frac{1-g}{g} \cdot \frac{1}{2\sqrt{\varepsilon_{\infty,np} + \frac{1-g}{g}\varepsilon'_m}}, \tag{2.15}$$

where $\partial \lambda_{res}/\partial \varepsilon'_m$ is the shift of the resonance wavelength per permittivity change and will be called *sensitivity* of the particle. Note that if ε'_m varies with wavelength, the derivative can no longer be taken. A constant permittivity is therefore assumed for the current analysis.

Equation 2.15 is plotted in figure 2.4(a – c) for varying surrounding medium permittivities and aspect ratios. Two trends can be identified: an increase of the sensitivity with increasing aspect ratio on one hand and with the surrounding medium permittivity approaching 0 on the other. Notable is also the strong impact of the nanoparticle material on the sensitivity. TiN shows the strongest sensitivity of the three materials, whereas aluminium the weakest. The influence of the aspect ratio comes from the fact that the resonance shift is proportional to $\frac{1-g}{g}$ which goes to infinity for large aspect ratios. The reason for the enhancement near $\varepsilon'_m = 0$ is that $\lambda_{res} = \lambda_t$ for $\varepsilon'_m = 0$, forcing the resonance to travel across a large part of the spectrum, especially for particles with large aspect ratios. The values for low ε'_m have to be considered with care though, since when ε'_m approaches 0, the plasmonic resonance is quenched due to the lack of a metal-dielectric interface. The surrounding medium no longer has a positive real part of the permittivity.

Quenching of the plasmonic resonance at ENZ can be seen by looking at the amplitude of the plasmonic resonance, which is given by the extinction enhancement factor, calculated as the extinction cross-section normalised by the physical particle cross-section. The extinction cross-section is a fundamental antenna property defined as the ratio of the sum of the absorbed, A and the scattered power, S, by the intensity, I, of the incoming light $\sigma_{\text{ext}} = (A + S)/I$ [123, 130]. The extinction enhancement factor is used to quantify the strength of the plasmonic resonance and plotted in Fig. 2.4(d) for gold nanoparticles. While an aspect ratio of 10:1 shows a peak for $\varepsilon'_m = 0.5$, which less elongated particles do not show, they all share the fact that for $\varepsilon'_m < 0.4$ the enhancement factor drops, i.e. the plasmon resonance is quenched. So, approaching the transition wavelength to obtain strong resonance shifts is not an option, at least not when the whole particle is surrounded by ITO. As will be seen in chapter 5, if a part of the metal-dielectric interface is preserved, the plasmon resonance can be preserved.

By combining equation 2.1 and equation 2.12, one obtains the resonance wavelength as a function of the change of carrier concentration in the surrounding medium. This also allows ε'_m to be dispersive and thus enables a complete description of the plasmon resonance in a tunable medium. Still, the one equation cannot be directly inserted into the other, instead one has to evaluate equation 2.7 for each carrier concentration and find the wavelength where it reaches the minimum. The result is shown in figure 2.5, where the resonance frequencies of gold and TiN spheroid particles for several aspect ratios are plotted. The background shows the real part of the permittivity of the surrounding medium, which corresponds to a top view of figure 2.2. The resonance lines follow to some extent the lines of constant ε'_m, though the dispersion of the metal has to be taken into account. At high carrier concentrations, the resonance is closer to the dashed ENZ line. One observes that for particles with a large aspect ratio the resonance is closer to the $\varepsilon'_m = 0$ region. For large aspect ratios, the resonance shifts are thus greater than for short particles. Comparing the response of gold and TiN particles, the TiN particles are generally slightly red-shifted, and therefore closer to the ENZ line than their gold counterparts, as well as

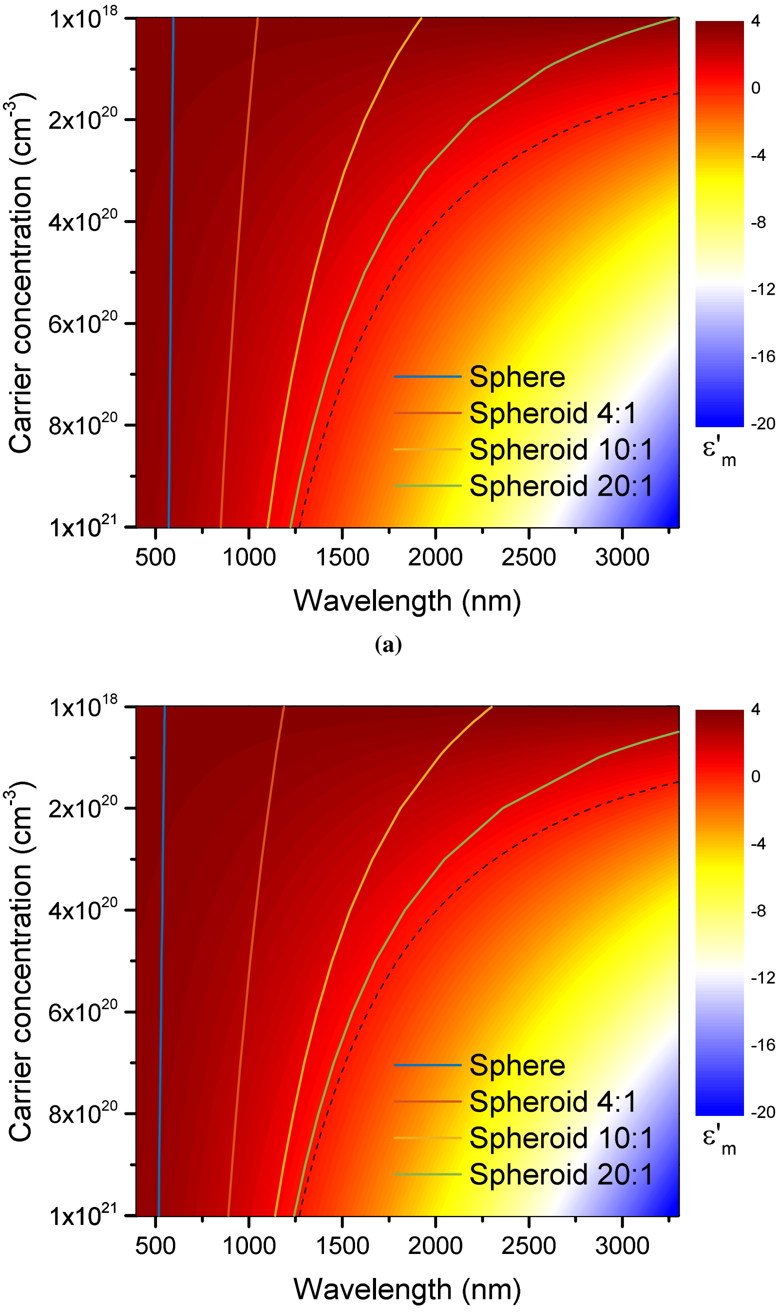

(a)

(b)

Figure 2.5: Resonance wavelength of spheroidal particles surrounded by ITO depending on the ITO carrier concentration. The contour map in the background, showing the ITO permittivity, is a top view of figure 2.2. The dashed line shows the region in which $\varepsilon_r' = 0$. (a) Resonance wavelength lines for spheroids out of gold and (b) resonance wavelength lines for spheroids out of TiN, calculated using equations 2.1 and 2.12.

more strongly curved, indicating a greater resonance shift for the same carrier modulation.

Another feature that can be observed in the graph is resonance pinning [46], caused by the suppression of the plasmonic resonance in regions where $\varepsilon \leq 0$. This leads to a reduced scaling of the resonance wavelength with antenna arm length, as can be well seen for the carrier concentration of $10^{21}\,\mathrm{cm}^{-3}$. While in a medium with constant refractive index, twice the aspect ratio leads to roughly twice the resonance wavelength, for high carrier concentrations the resonances are grouped together into a narrow spectral range.

At this point, the limitation of the developed model becomes apparent, which is the assumption that carrier modulation occurs in the whole ITO around the particle. Instead, carriers accumulate in thin layers, so that only a fraction of the particle's near-field volume experiences a change in the permittivity. The response is expected to be a small modulation around a working point in the graph. Nonetheless, accurate modelling above the level of qualitative aspects can only be done using numerical approaches.

2.3 Fabricated antenna dimensions and coupled nanoantennas

Realistic sizes of the fabricated nanoantennas made throughout this thesis are limited by the dimensions that can reliably be fabricated with e-beam lithography (EBL) patterning. This limits the length and width of the antennas to sizes larger than $50\,\mathrm{nm}$, with common values being widths of $80\,\mathrm{nm}$ to $100\,\mathrm{nm}$ and lengths of $100\,\mathrm{nm}$ to $800\,\mathrm{nm}$. These values are out of the range of the dipolar approximation, resulting in a broadened and red-shifted resonance compared to the dipolar case. The thickness is not limited by EBL, but is chosen depending on the material properties. For gold, the thickness is the minimum thickness where the formation of a continuous film is guaranteed, for which $30\,\mathrm{nm}$ is a suitable value from experiments. Thin antennas also reduce higher order resonances [128]. For TiN, the optimum thickness for a balance between surface scattering and bulk losses is at $50\,\mathrm{nm}$ [80] and for ITO between $80\,\mathrm{nm}$ and $120\,\mathrm{nm}$ [131].

As a last step from simple dipolar particles to realistic nanoantennas (with dimensions below $1\,\mathrm{\mu m}$), the coupling of two antenna arms separated by a small gap, a so-called dimer antenna, will be described. It is widely known that if two or more nanoparticles are close to each other, they couple capacitively leading to a red-shift in their resonance [3, 132, 133]. This coupling creates a field enhancement inside the gap between the particles, the strength of which depends, among other factors, on the nature of the excited modes. Several scaling laws have been proposed for different applications [130, 134–136]. For the quasistatic approximation, there is a derivation of the resonance shift in the supporting information of reference [137]:

$$\Delta\lambda/\lambda_0 = \frac{14.3\varepsilon_m/g^2}{(12r_{\text{sph}}(s/a)^3 - 1/g)(464.6 + 14.3\varepsilon_m(1/g - 1))}. \tag{2.16}$$

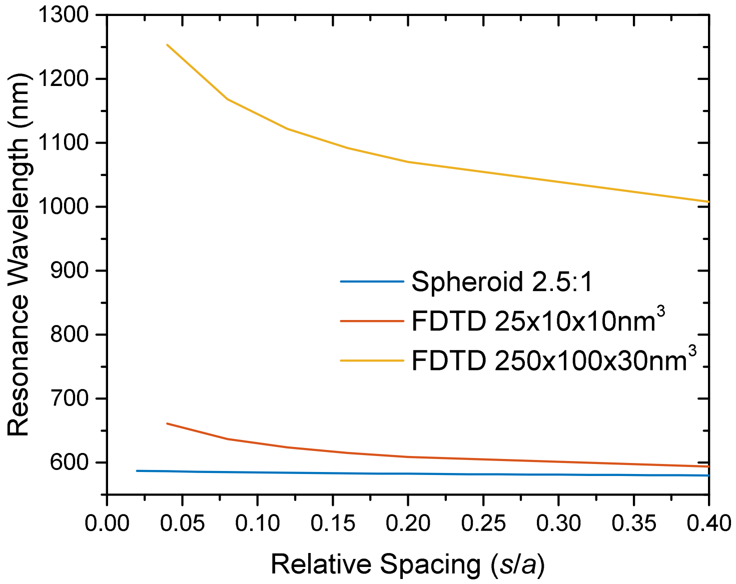

Figure 2.6: Resonance wavelength shift as a function of relative particle spacing for a dimer antenna of two spheroidal particles of aspect ratio 2.5:1. Numerical plots for a $25 \times 10 \times 10\,\mathrm{nm}^3$ and a $250 \times 100 \times 30\,\mathrm{nm}^3$ arm dimer antenna are given as well.

Here, s is the interparticle gap, the other variables are as defined previously. The cubic function of s/a, the size of the gap relative to the antenna arm length, dominates this equation. The surrounding medium permittivity and the aspect ratio only have a small influence on the coupling behaviour. That is why this equation is called the 'universal scaling law' for interparticle coupling. For simplification purposes, it is usually approximated by an exponential function that is fitted to experimental data [137].

Figure 2.6 shows the increasing resonance red-shift with decreasing gap size that a spheroid with an aspect ratio of 2.5:1 experiences. The surrounding medium permittivity is that of air. For the analytical formula, the resonance wavelength for a single particle is located at $576\,\mathrm{nm}$ and shifts to $582\,\mathrm{nm}$ for a gap of $10\,\mathrm{nm}$, i.e. by 1.5%. The Lumerical FDTD simulation results for the rectangular $25 \times 10 \times 10\,\mathrm{nm}^3$ arm antenna, which is within the dipole regime, do not match this. Instead, the shift in this case is from $594\,\mathrm{nm}$ to $661\,\mathrm{nm}$, i.e. by 11%. This red-shift between analytical formula and numerical results was found to be systematic, and after extensive checks on the derivation of equation 2.16, it was found that the equation does not accurately describe the modelled system, for an unknown reason.

To compare the analytical results to fabricated structures, several adjustments must be made. For a surrounding medium consisting of a glass substrate and air above, $\varepsilon_m = 1.75$ has been shown to be a good representative [124]. Additionally, fabricated antennas have a typical size of $250 \times 100 \times 30\,\mathrm{nm}^3$ to reduce the demand on the lithography precision. The comparably low thickness of $30\,\mathrm{nm}$ represents the optimum balance between minimum surface scattering and reduced higher order resonances. Still, the overall larger size red-shifts the resonance by $414\,\mathrm{nm}$ compared to the dipolar antenna with the same aspect ratio. Since the red-shift obtained by coupling is relative to the uncoupled resonance, particles with a longer resonance wavelength experience a larger red-shift. This is also shown in Fig. 2.6.

2.4 Conclusions from the theoretical analysis

To summarise the findings of this chapter, the material properties according to the Drude model and its influences on a plasmonic resonance described by Mie-Gans theory were analysed. The Drude model was found accurate for the description of TCOs over a wide spectral range. The Mie-Gans model for plasmonic resonances gave superior results, for aspect ratios below 10, compared to a model by Novotny [121]. The model was then used to characterise the interaction between carrier modulation in TCOs with the plasmonic near-field around a resonant particle. Noticable wavelength shifts are predicted for currently realisable carrier modulations on the order of $1 \times 10^{20}\,\mathrm{cm}^{-3}$, especially if the particle aspect ratio is large and the medium in its epsilon-near-zero range. Compared to gold particles, TiN particles offer a higher sensitivity to changes in the surrounding medium, due to the flatter curve of the material's real part of the permittivity. The last part of the chapter compared the ideal particle dimensions with realistic antennas, finding that the general resonance wavelength is red-shifted by higher order resonances in the antenna and by arm coupling of dimer antennas.

3 Fabrication and characterisation methods and simulation validations

The first part of this chapter describes the various techniques for the fabrication and characterisation of optical nanostructures. The key method to define the dimensions of the nanostructures used for this thesis is electron-beam lithography (EBL), which is described in the first section. Connected to the patterning of nanostructures is the deposition and ellipsometry-based characterisation of the optical properties of transparent conductive oxides (TCOs), which comprises the main part of deposition recipe developments that were performed for this thesis. The deposition and patterning section is followed by a listing and detailed description of the various characterisation tools that were used in the experiments. The last section of this chapter deals with the numerical simulation methods and a comparison between the commercially available Lumerical FDTD and COMSOL Multiphysics, including a validation of a case where the two softwares showed different results for a particular structure. The chapter is concluded by a comparison of the results from the electrical solver of Lumerical with the analytical formulas from Thomas-Fermi screening theory.

3.1 Electron-beam lithography patterning

EBL patterning is a powerful lithographic tool that provides the precise patterning of nanostructures of various different materials. It is a development from photo-lithography and shares many of its fabrication steps, such as the spinning of a resist onto the sample which is subsequently exposed and developed. The key difference is that in EBL, the exposure occurs via an electron beam instead of optical radiation. The electron beam is focused onto the sample in a nanometre-sized spot and the pattern written pixel by pixel. For the JEOL JBX-9300FS system used in the Southampton University's nanofabrication cleanroom, the minimum spot size for the voltage of $100\,\mathrm{kV}$ is $5\,\mathrm{nm}$ with a current of $5\,\mathrm{nA}$. Exposure dose and development procedure depend on the chosen patterning, deposition methods and resists.

3.1.1 E-beam patterning techniques

Materials can be deposited isotropically, i.e. there is a preferred direction of deposition, or anisotropically. If the deposition method of choice deposits materials anisotropically, like sputtering and ALD, the material has to be patterned by etching. Strictly speaking, ALD is conformal, i.e. the material follows the shape of the substrate when deposited. With etching, the resist is the top layer and the pattern on it is transferred onto the material beneath. Etching methods used in the framework of this thesis are reactive ion etching (RIE), which is chemically selective due to the use of plasma-activated chemicals, and ion beam etching (IBE), which uses an argon ion bombardment to physically ablate the material and is thus not chemically selective. When etching is used, it is possible that the chemical properties of the material's sidewalls, or even the bulk, change. Changes in the chemical properties will add an additional influence to the optical properties of the material than those that would result from the pattern change alone.

For isotropic deposition methods such as evaporation, the material deposition has a preferred direction and the material can be patterned by lift-off, thereby minimising chemical reactions in the material. Three methods for positive resists (the exposed area is the final pattern) were used throughout this thesis: single layer lift-off, bilayer lift-off and trilayer lift-off. In the case of single layer lift-off, only one resist material is chosen for exposure and spin-coated onto the substrate in a single layer. After exposure, the development of the resist creates a slight undercut in the resist. The undercut comes from the increased exposure dose near the substrate edge from backscattered electrons. This slight undercut ensures that when the material is deposited in the next step, the part deposited on the substrate is not connected to the material deposited onto the remaining resist. Lift-off is then performed by dissolving the unexposed resist. Possible positive resists for single-layer lift-off are poly-methyl-methacrylate (PMMA) and ZEP (proprietary name) .

In the case of a bilayer resist, PMMA and methyl-methacrylate (MMA) are spin-coated on top of each other. Since MMA is highly soluble by the PMMA developer, a large undercut is created. This gives advantages when the undercut generated by a single PMMA layer is too small, as is the case for low doses, small patterns and low pattern densities.

The tri-layer lift-off is a further development of the bilayer resist patterning. Between the MMA and PMMA spinning, a $20\,\mathrm{nm}$ thick SiO_2 layer is deposited via low-temperature plasma enhanced physical vapour deposition (PECVD). After exposure, the SiO_2 protects the MMA from development. In a second step, the structure is dry-etched by RIE to transfer the pattern into the SiO_2 and MMA. The resulting tri-layer resist has a very small, but sufficient, undercut from the sidewall etching of the RIE. This allows the fabrication of high-density nanoparticle arrays with high precision of size and gap.

3.1.2 Deposition and characterisation of transparent conductive oxides

The samples under investigation in the framework of this thesis were fabricated using a large number of deposition tools. Standard tools that have been used for example are sputtering and plasma-enhanced chemical vapour deposition (PECVD). In sputtering, a material is ablated from a source, such as a TiN target, via argon ion bombardment and redeposited onto the sample. In PECVD, chemicals react directly on the sample, for example silane reacting with oxygen plasma to form SiO_2. Both processes are anisotropic and their choice depends on the material to be deposited. In the following section, the less well-known methods of depositing ITO via e-beam evaporation and AZO via ALD will be described.

E-beam evaporation of ITO and ellipsometry

The process of depositing ITO via e-beam evaporation was evaluated and characterised intensively during the work for this thesis. The existing deposition recipe for ITO nanostructures in combination with EBL patterning was to deposit ITO with a speed of $1\,\text{Å}\,\text{s}^{-1}$ to $2.5\,\text{Å}\,\text{s}^{-1}$ in an oxygen environment, where the O_2 partial pressure determined the final carrier concentration. The ITO source was pressed pellets from a powder of 90wt% In_2O_3 and 10wt% Sn_2O_3 from Sigma-Aldrich. After deposition, the sample was annealed in an oven at 200°C under atmospheric conditions for an hour, thereby reducing optical losses by increase of the grain size and reducing the carrier concentration by refilling of oxygen vacancies. The final carrier concentration was around $1 \times 10^{20}\,\text{cm}^{-3}$ to $4 \times 10^{20}\,\text{cm}^{-3}$ if the O_2 partial pressure was set to $4 \times 10^{-4}\,\text{mbar}$ during deposition and from $5 \times 10^{20}\,\text{cm}^{-3}$ to $1 \times 10^{21}\,\text{cm}^{-3}$ for an O_2 partial pressure of $2 \times 10^{-4}\,\text{mbar}$.

This recipe, which was developed by Dr. Yudong Wang, was based on Hall measurements, where the carrier concentration and mobility are measured from the deviation that accelerated electrons experience when deflected by a magnetic field. A pair of electrodes applies an external voltage in one direction (x) that accelerates free carriers. At the same time, a magnetic field is applied perpendicular to the external voltage (z-direction), leading to a Lorentz force that accelerates the electrons perpendicular to both fields (y-direction). Along the third dimension in which the electrons are deflected by the magnetic field, an electric field is created by the accumulation of carriers at the edge of the semiconductor. This electric field and the resulting voltage are measured with the second pair of electrodes, from which the carrier concentration can be calculated.

Compared with optical measurements of various types, the author noticed that the carrier concentration from Hall measurements often did not coincide with that from fits to optical data of the same sample. This is mentioned in some of the literature as well [73], while there are also references where Hall and optical measurements agree [42]. The author found that for samples deposited during the work for this thesis, the carrier concentration values of ITO were in less than 20% of the cases in the same order of magnitude between Hall and optical measurements. In the other cases, the Hall measurement overestimated the carrier concentration by an order of magnitude, sometimes even more.

Additionally, in some cases, optical spectra did not show any ITO-typical behaviour, such as plasmonic behaviour in the IR, which indicated a low ITO carrier concentration below $10^{19}\,\mathrm{cm}^{-3}$. Again, Hall measurements showed carrier concentrations on the order of $10^{20}\,\mathrm{cm}^{-3}$. This disagreement between the two measurements affected particularly the work on ITO gap-loaded antennas in chapter 6.1. A possible explanation of the differences between the measurement methods is that the Hall measurement setup gives the electron concentration in localised regions where it is particularly high, such as the surface layer, since the conductivity there will be increased. Optical measurements, however, average over a large volume, thus giving different results. Apart from the discrepancy of the measurement methods, it was also concluded that the deposition process was not reliable, with possible reasons being an insufficient control of the O_2 partial pressure or the deposition speed, a contamination of the chamber by materials deposited during other runs or contamination of the source material. Therefore, two conclusions were drawn from the listed issues: first the optical properties of fabricated films need to be characterised precisely, and second the reproducibility of the ITO deposition needs to be increased.

For the first reason, a characterisation method was developed using ellipsometry, including models to accurately determine the complex refractive index. Ellipsometry is an extremely accurate tool for the optical characterisation of thin films. It uses elliptically polarised light, which is shone onto the sample and the changes in polarisation of the reflected light along two axes recorded. By varying the angle of incidence, a total of three parameters are available from which the complex refractive index, n and k, and the thickness of the film, d, can be accurately obtained. Apart from the quality of the fit that is applied by the user, the tool is only limited if the film is thinner than $1\,\mathrm{nm}$ or the material so lossy that no light reaches the detector. Back reflections from transparent substrates such as glass create large amounts of noise, which is why the best results were obtained for silicon substrates with $150\,\mathrm{nm}$ of thermal oxide on the surface. Silicon and SiO_2 were found to be accurately represented in the database of the analysis software.

To analyse the measured spectra of the polarisation angles, different modelling approaches are possible. The intuitive choice is a Drude model, which models the free-carrier behaviour in the material (see section 2.1.1 on p. 10). An issue, however, is that the fit algorithm of the ellipsometry software tends to choose values that are unphysically high, such as $N = 10^{22}\,\mathrm{cm}^{-3}$, and has trouble dealing with such large fit range limits. Also, the Drude model cannot describe the optical bandgap of ITO in the UV. The method of choice was therefore to use an assumption-free B-spline model to obtain n, k and d over the whole wavelength range from $200\,\mathrm{nm}$ to $1700\,\mathrm{nm}$. Enabling the Kramers-Kronig relations [138], a model describing the reciprocal dependence of n on k and vice versa, ensured physical behaviour of the refractive index. The data was then fitted manually with two models, a Lorentz model with a single resonance for the spectral range below $600\,\mathrm{nm}$ and a Drude model to the wavelength range above $600\,\mathrm{nm}$, to be sufficiently far away from band transitions.

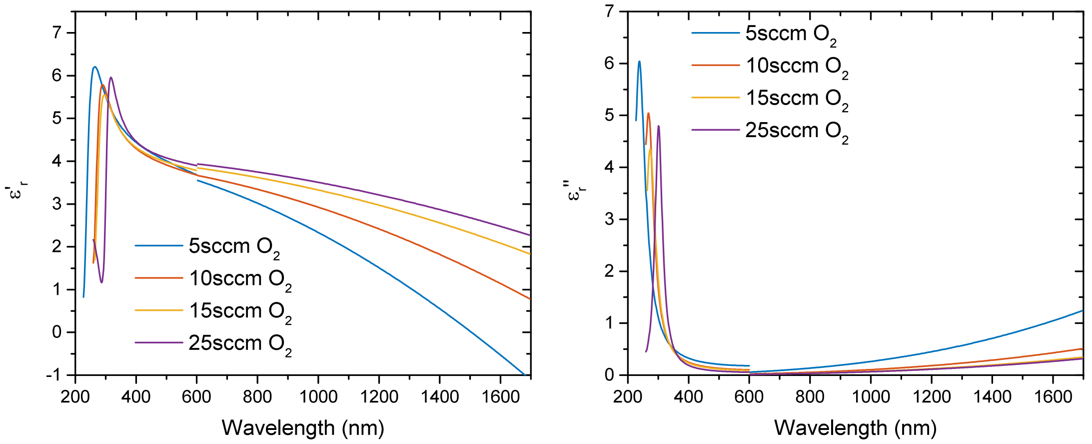

Figure 3.1: Material parameters of e-beam evaporated ITO with ionised O_2-doping. Obtained from ellipsometry data fitted with a Lorentz model for $250\,\mathrm{nm}$ to $600\,\mathrm{nm}$ and a Drude model for $600\,\mathrm{nm}$ to $1700\,\mathrm{nm}$. (a) Real part of the dielectric permittivity; (b) imaginary part of the dielectric permittivity.

To improve the reproducibility of the ITO deposition process, other deposition recipes were investigated. Since one of the available evaporators had an in-built ion gun, an existing recipe was tested using ionised O_2 with a flow of $25\,\mathrm{cm}^3$, a deposition speed of $1.0\,\text{Å}\,\mathrm{s}^{-1}$ and a substrate heater set to $200\,°\mathrm{C}$, showing good reproducibility in optical properties. Though the deposition speed and thickness were found to be 60% higher than set on the machine, the effect was stable over all runs and could easily be adjusted for. The sample was not post-annealed, since it was already heated during deposition.

By controlling the oxygen flow rate (given in standard cm^3 per minute, sccm), real and imaginary part of the electric permittivity can be tuned, as shown in figure 3.1. The figure shows the two fits for the different spectral ranges in one graph. A small discontinuity can be seen where the fit data meets. The material parameters are given in table 3.1. The standard method to obtain the Drude parameters is to measure N and μ via Hall measurements and use ellipsometry to determine m^*, however in the present case m^* is a fixed value, because the two measured entities n and k are not enough to solve for three variables. The optical simulations based on this data will still be correct, since they use the permittivity values directly, but the origin of the observed permittivity might be different from what was found with the presented model. The effective electron mass was set to $m^* = 0.4m_\mathrm{e}$ [54] to ensure reasonable results. The ITO deposited using ionised oxygen shows good scaling of the carrier concentration, which can be tuned from $3 \times 10^{20}\,\mathrm{cm}^{-3}$ to $8.7 \times 10^{20}\,\mathrm{cm}^{-3}$. At the same time, the losses in the film stay constant at $1.7 \times 10^{14}\,\mathrm{rad\,s}^{-1}$, except for the lowest O_2 flow, where the high carrier concentration probably causes increased electron-electron scattering [55]. ε_∞ changes weakly from 4.1 to 4.3.

Table 3.1: ITO properties for evaporated films as a function of oxygen flow during deposition. The value of m^* is fixed while N, Γ and ε_∞ are variables.

O_2 flow (sccm)	N ($\mathrm{cm^{-3}}$)	Γ ($\mathrm{rad\,s^{-1}}$)	m^*	ε_∞	Film thickness (nm)
25	3.0×10^{20}	1.8×10^{14}	0.4	4.18	325
15	3.7×10^{20}	1.7×10^{14}	0.4	4.14	110
10	5.25×10^{20}	1.7×10^{14}	0.4	4.09	108
5	8.7×10^{20}	2.6×10^{14}	0.4	4.26	115

AZO deposition by ALD

The AZO used for the metasurface-based optical solar reflector in chapter 4 was fabricated using thermal ALD. Dr. Kai Sun developed the recipe from existing recipes for both ZnO and Al_2O_3. ALD is a development of chemical vapor deposition (CVD) , where the formation of a material self-terminates after each monolayer [72]. That way, deposition of single atomic layers of a material can be done in a four-step process. In the first step, the precursor of the first material (diethylzinc for ZnO and trimethylaluminium for Al_2O_3) is deposited onto the sample. Reactions with the sample surface ensure that the first layer of molecules is covalently bonded, while further material is purged in the second step. The third step consists of the reaction of the first layer of molecules with water vapour under a temperature of 350°C. This creates the first monolayer of ZnO or Al_2O_3 respectively. Afterwards the chamber is purged again.

For a highly optimised process, where each purge lasts only as long as necessary, depositing a monolayer takes several hundred milliseconds. A standard deposition however can take hours

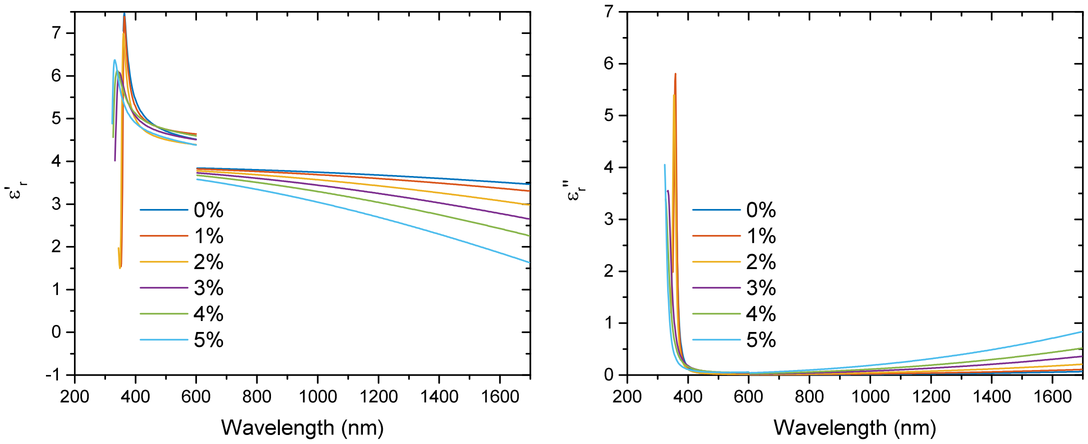

Figure 3.2: ALD AZO spectra from ellipsometry fitted with a Lorentz model for 250 nm to 600 nm and a Drude model for 600 nm to 1700 nm. (a) Real part of the dielectric permittivity; (b) Imaginary part of the dielectric permittivity

Table 3.2: AZO properties for ALD films as a function of Al-doping concentration. The value of m^* and ε_∞ are fixed while N and Γ are the variables.

Al (mol%)	N ($\mathrm{cm^{-3}}$)	Γ ($\mathrm{rad\,s^{-1}}$)	m^*	ε_∞
0	6.9×10^{19}	1.7×10^{14}	0.4	3.9
1	9.5×10^{19}	2.0×10^{14}	0.4	3.9
2	1.5×10^{20}	2.5×10^{14}	0.4	3.9
3	2.1×10^{20}	3.2×10^{14}	0.4	3.9
4	2.8×10^{20}	3.5×10^{14}	0.4	3.9
5	4.0×10^{20}	4.1×10^{14}	0.4	3.9

for $100\,\mathrm{nm}$. For large-scale industrial applications, a proposed faster method is spatial ALD [139], where the substrate moves under the valves emitting each precursor similar to a roll-to-roll process, thereby increasing deposition speed.

To deposit AZO, ZnO and Al_2O_3 are deposited intermittently. While evaporated ITO has a fixed tin-doping of 10wt%, the aluminium-doping of AZO can be tuned during deposition. For a 5mol%-doping, 20 layers of ZnO are deposited, then a single layer of Al_2O_3. This is repeated until the desired thickness is reached. The monolayers of both materials are around $1\,\text{Å}$ thick. By changing the mixing ratio of ZnO and Al_2O_3, the carrier concentration of the final film can be tuned from $7 \times 10^{19}\,\mathrm{cm^{-3}}$ to $4 \times 10^{20}\,\mathrm{cm^{-3}}$, see figure 3.2. The data is listed in table 3.2. The two spectral ranges show a significant discontinuity, which comes from the fact that the AZO bandgap covers a broad spectral range in the UV, and is poorly fitted by a single Lorentzian oscillator. The oscillator was chosen in such a way that it matched the long-wavelength edge of the bandgap sufficiently well. In case of the ellipsometry data above $600\,\mathrm{nm}$, the ellipsometry change was not always enough to determine the Drude parameters, because the AZO carrier concentrations were too low to allow an accurate fit. This was solved by obtaining the Drude parameters from a simulation fit to the IR reflectivity of the AZO film. The substrate used for this purpose was the optical solar reflector used in chapter 4. Again, the effective electron mass was fixed, and since the background permittivity only varied weakly in ITO, it was fixed here to simplify the fitting.

The achievable AZO carrier concentrations are lower than those of ITO, due to the lower doping. Up to $4 \times 10^{20}\,\mathrm{cm^{-3}}$ can be achieved. However, at comparable carrier concentrations, the AZO losses are twice to three times higher than those of ITO. This can be attributed to the lower mixing of ZnO and Al_2O_3 in a layer-by-layer deposition compared to evaporation of pre-mixed ITO pellets [140].

3.2 Experimental characterisation tools

3.2.1 Fourier-transformed infrared reflectometry

For reflectivity measurements in the mid-IR, a powerful tool is Fourier-transformed infrared reflectometry (FTIR). FTIR uses an infrared source with an interferometer to obtain an interference pattern between the IR radiation emitted from the source and the one reflected from the sample. The detected interference pattern is then Fourier-transformed to obtain spectral information from the spatial pattern.

The setup used for this thesis consists of a Thermo-Nicolet Nexus 670 with a continuum microscope, a mid-IR light source, a KBr beam splitter and a nitrogen-cooled deuterium-doped triglycine sulfate (DTGS) detector. The wavelength range of the available FTIR is $2\,\mu\mathrm{m}$ to $25\,\mu\mathrm{m}$, which allows the characterisation of samples for longer wavelengths than any other available tool. The signal-to-noise ratio of the FTIR improves for larger beams, which is why the measurements are usually taken from an array of nanoantennas with an area of $100 \times 100\,\mu\mathrm{m}^2$. The resulting spectra can therefore suffer from homogeneous broadening due to fabrication variances of the individual antennas in the array.

3.2.2 Spatial modulation spectroscopy

Spatial modulation spectroscopy (SMS) is an optical spectroscopy tool that can detect smaller particles than standard optical microscopes [141–143]. The key element is the spatial modulation of the position of either the sample or the laser beam. The frequency of the spatial modulation and its second harmonic can be selected in a lock-in amplifier, thereby increasing the signal-to-noise ratio. It can be used to measure the extinction spectra of single nanoantennas and nanoparticles. Whereas common dark-field microscopy cannot detect the scattering from gold nanospheres smaller than 50 nm [144, 145], SMS is able to detect gold nanospheres down to 5 nm in diameter [142]. This comes from the fact that SMS detects extinction, which includes the absorption that dominates the optical response of small particles. The SMS therefore allows unmatched direct measurements of the extinction cross-section spectra of single nanoparticles [146–148]. The technique can also be combined with other optical characterisation tools such as pump-probe microscopy [149], allowing the full optical characterisation of single particles. Another optical method of comparable single-particle sensitivity is superresolution optical fluctuation imaging (SOFI) [150], which relies on the fluctuations of the intensity of quantum dots to separate their optical signals from each other. However, it only works for quantum dots, and not for plasmonic particles.

The unique property of the spatially modulated signal is that the difference between the incident power and the power of the second harmonic of the reflection is directly proportional to the

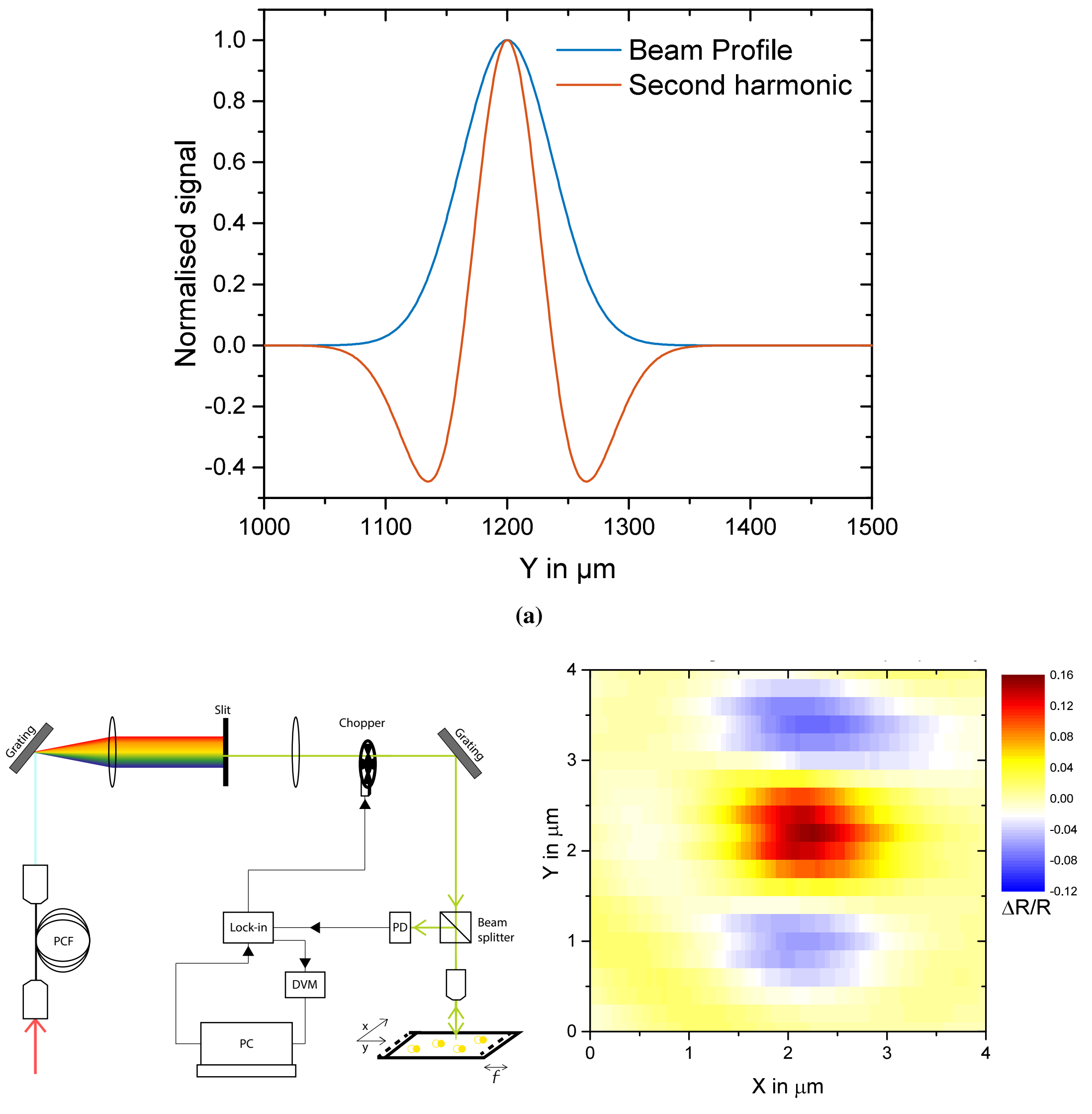

(a)

(b) **(c)**

Figure 3.3: (a) Example of a normalised Gaussian beam profile and its normalised second derivative. (b) Spatial modulation spectroscopy setup adapted from [141]. A photonic crystal fibre generates a broadband spectrum, from which a wavelength is selected to excite the sample. The sample's spatial position is periodically modulated and the excitation signal analysed with a lock-in amplifier. (c) Example of a measured spatial modulation map at resonance of a gold dimer with $250\,\mathrm{nm}$ arm length and $40\,\mathrm{nm}$ gap by the author.

extinction cross-section of the particle under investigation [141]:

$$\Delta R(x,y,\lambda) \approx \frac{1}{4}\sigma_{\text{ext}}(\lambda)\delta_y \frac{\partial^2 I_\lambda(x,y)}{\partial y^2}\cos(4\pi f_0 t), \tag{3.1}$$

where $\Delta R(x,y,\lambda)$ is the reflected power at the second harmonic, $\sigma_{\text{ext}}(\lambda)$ the extinction cross-section, δ_y the modulation width, $\frac{\partial^2 I_\lambda(x,y)}{\partial y^2}$ the second derivative of the particle's point spread function, f_0 the spatial modulation frequency and t time. If the particle is much smaller than the beam, the point spread function will be defined by the Gaussian profile of the incoming beam. A theoretical Gaussian profile and its second derivative are shown in Fig. 3.3(a).

Figure 3.3(b) shows the setup for spatial modulation spectroscopy. A photonic crystal fibre generates a broadband spectrum which is spread out using a grating and a lens. From the spectrum, the excitation wavelength is chosen via a slit. A chopper modulates the beam with a frequency of $450\,\text{Hz}$ which enables the detection of the reflected power R. The laser beam is spatially modulated along the y-direction with a frequency of $f = 650\,\text{Hz}$, creating a reflection signal R_{2f} at twice the frequency. The reflected light is focused onto a photodiode and fed into a lock-in amplifier, which detects the two modulated signals. A computer calculates $\Delta R = R_{2f} - R$ and normalises it to the unmodulated signal $\Delta R/R$, so that the final signal is independent of the excitation spectrum of the photonic crystal fibre. By solving equation 3.1 for σ_{ext}, the extinction cross-section spectrum of the particle under investigation can be calculated from the lock-in signal, given the beam profile and spatial modulation amplitude are known.

A 2D map of the SMS signal from a gold dimer with $250\,\text{nm}$ arm length and $40\,\text{nm}$ gap is shown in Fig. 3.3(c). The wavelength was at the resonance of the antenna at $1200\,\text{nm}$. The central peak, shown in red, represents the antenna position. The blue patches above and below are coming from the negative side lobes of the second harmonic of the Gaussian profile (Fig. 3.3(a)), since spatial modulation was applied along the y-axis.

Due to its highly sensitive nature, spatial modulation microscopy is affected by small variations in focus and antenna position. When the centre of the antenna is found ($y = 1200\,nm$ in Fig. 3.3(a)), a wavelength scan gives the $\Delta R/R$-spectrum. A phenomenon that often occurs are negative parts of that spectrum, which lead to negative extinction cross-sections that are not physical. One possible cause is that the modulated signal becomes negative, which occurs if the beam is not aligned with optical axis and moves to the side-lobes of the antenna during the wavelength scan. Another possibility is that the phase of the substrate reflectivity changes due to interference effects. The latter will be seen in all spectra consistently, while the former can depend on the precision of the positioning of each antenna into the beam.

3.2.3 Electro-optical modulation spectra

Electro-optical modulation spectroscopy is a variation of spatial modulation spectroscopy in which the modulation method is swapped from spatial to electrical modulation of suitable samples that provide electrical contacts. In electro-optical modulation spectroscopy, a function generator applies a voltage onto the sample to periodically accumulate and deplete carriers. By using a lock-in amplifier to select the frequency of the function generator, the difference between the antenna spectra at the two modulations can be extracted. A theoretical example is given in Fig. 3.4(a), where 'resonance 1' is the first, and 'resonance 2' the second resonance shifted by $100\,\mathrm{nm}$ due to carrier modulation. The normalised difference of the two spectra is then calculated by:

$$\Delta R/R_0 = (R(V_+) - R(V_-))/R_0, \qquad \Delta\sigma/\sigma_0 = (\sigma(V_+) - \sigma(V_-))/\sigma_0. \tag{3.2}$$

V_+ and V_- indicate the maximum and minimum voltage of the voltage sweep. Figure 3.4(b) gives an example of the normalised difference of two spectra, which is a wave-pattern that has two extrema, showing the spectral location where the modulation is strongest. If the shape of the antenna resonance does not change, the difference spectrum is symmetrical and crosses 0% relative modulation at the middle between both resonances. This signal is not directly connected to the antenna spectrum, but gives a direct reading of the optical modulation strength and its spectral position. In the case of simulations of the antenna extinction cross-section σ, the normalised difference $\Delta\sigma/\sigma_0$ is calculated manually by subtracting the two modulated spectra and dividing them by the zero-volt spectra.

3.2.4 Scanning electron microscopy

In scanning electron microscopy (SEM), a beam of highly accelerated electrons is used to scan across an area, while the electrons scattered back by the sample are measured. Since the amount of electron scattering from a structure depends strongly on the electron configuration of the material, SEM gives a good material contrast. Gold for example is a much better scatterer than aluminium, even though both are metals. The resolution of an SEM image is limited by the beam size and shape, as well as the electron acceleration voltage. Typically the spot size is on the order of $10\,\mathrm{nm}$, which is larger than for EBL due to the lower acceleration voltage. SEM allows high-resolution 2D images with good material contrast.

3.2.5 Atomic force microscopy

Atomic force microscopy (AFM) measures the interaction between a cantilever and the atoms on the surface of a sample. It is an unmatched tool to measure surface profiles with sub-nanometre

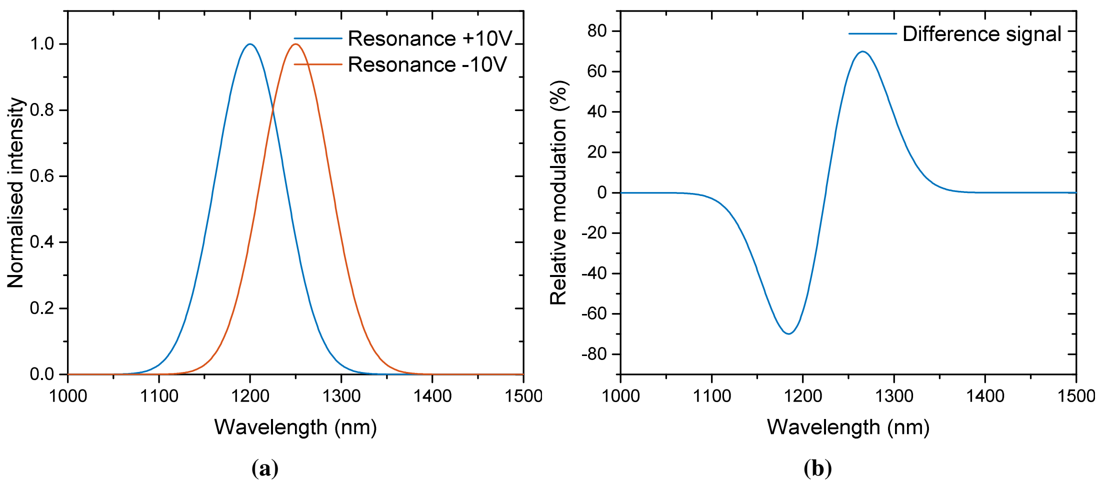

Figure 3.4: Numerical example of the principle of electro-optical modulation spectroscopy: (a) showing two Gaussian spectra separated by $100\,\mathrm{nm}$; (b) the resulting normalised second differential signal.

precision. The cantilever position is monitored by a laser deflection measurement while the sample is scanned. Tapping mode is the most common way of measuring the height profile of a sample, where the cantilever is brought to oscillations. The oscillation frequency and its changes due to interaction with the sample are monitored to obtain the height information. If the phase changes of the oscillations are recorded, different materials can also be distinguished.

Tapping mode is more robust to sudden height changes than traditional operation modes, where the cantilever is stationary and its height is kept constant while the force is measured. The opposite is also possible, where the height is controlled such that the force on the cantilever is constant. In all modes, the height measurement precision is only limited by the precision of the piezo-controllers used to control the position of the cantilever. However, the precision of the profile in x- and y-direction is limited by the thickness of the cantilever's tip, which is usually around $10\,\mathrm{nm}$. Together with SEM, AFM allows the creation of a high-resolution 3D model of the sample.

3.3 Numerical simulations

The simulation of plasmonic structures can be done analytically and numerically. While analytical simulations give exact solutions, they can only be calculated for certain assumptions such as a homogeneous surrounding medium and certain simple geometries. An analytical description of longitudinal plasmon resonances of elongated particles was presented in the previous chapter. Numerical computations become necessary if there is no analytical solution available for a specific problem, as is the case for complex structures. Then, numerical solutions for Maxwell's equations, which govern the propagation of light in media, become necessary. To find an approximate solution, the integrations over a surface or volume are substituted by sums over a mesh, where the precision of the approximation is limited by the density of the mesh. [133]

In the numerical solvers regarded in this thesis, the Helmholtz equation, a derivative of Maxwell's equations [6], is solved in either the time or frequency domains:

$$\nabla \times (\nabla \times \vec{E}) - k_0^2 \varepsilon_r \vec{E} = 0, \tag{3.3}$$

with $\vec{E}$ being the scattered or total field, depending on the application, and $k_0 = 2\pi/\lambda$ the wavevector of the incoming electromagnetic wave. From the electric field $\vec{E}$, the antenna cross-sections, as well as reflection, absorption and transmission can be calculated. For the antenna cross-sections, a model with perfectly matched layer (PML) boundary conditions has to be created [151]. PMLs absorb incoming light without back reflection due to their impedance-matched nature so that, to the electromagnetic wave, the simulation domain appears to be infinitely large. The absorption cross-section is calculated by integrating over the total field going through the particle boundaries, while the scattering cross-section is integrated over the scattered fields going towards the PMLs. To obtain reflection, absorption and transmission, periodic boundary conditions are used on the boundaries transverse to the direction of propagation, while PMLs remain in backward and forward propagation direction. This is necessary because reflection and transmission are recorded over the whole area, and PMLs parallel to the propagation direction distort the electric field in that direction. If periodic boundaries are used for single-particle simulations, care has to be taken to make the model large enough so that undesired interactions between the periodic cells are minimised.

In the simulations for this thesis, the optical constants were carefully selected based on the application and the spectral range of interest. While the optical solvers can automatically interpolate sampled data, extrapolation is often imprecise and therefore requires a sufficient amount of data points within the chosen wavelength range. Lumerical performs extrapolation using a multi-oscillator model that is flexible towards different causes of dispersion, such as bandgaps or elastic scattering. Comsol offers linear and polynomial extrapolation. Simple dielectrics can be described by only the refractive index, e.g. 2.1 for HfO_2 [96, 152] and 1.45 for SiO_2 [153]. In the mid-IR range, phonon interaction necessitates the full description of the dielectrics optical properties, as is done in chapter 4. Gold is described by the data from Johnson & Christy [127] for wavelengths up to $2000\,\mathrm{nm}$ and by data from the CRC Handbook of Chemistry and Physics for longer wavelengths [126]. The CRC Handbook also gave the data for aluminium. ITO and AZO are modelled with the Drude model given in section 2.1.1 in the last chapter, while TiN is based on ellipsometry data from own measurements.

3.3.1 COMSOL Multiphysics®

A widely used software to numerically compute optical properties is COMSOL Multiphysics, which uses the finite-element method (FEM). For this thesis, COMSOL was used for comparison to evaluate some of the Lumerical software simulations. A two-step simulation was chosen to compute the scattered fields. In the first step, the background field in the model volume is calculated for a sample without nanoantennas, i.e. with only the substrate. In the second step, the background field is used as the excitation field for the device to compute the extinction cross-section of the nanoantennas. To obtain a wavelength spectrum of the extinction cross-section, the model has to be solved for each wavelength individually, which can take a large amount of computational resources.

The mesh in COMSOL is a hybridisation between a rectangular mesh, which is used for the PMLs and the medium around the particles, and a triangular mesh, which is used for the nanoparticles. For the simulations in this thesis the standard mesh settings for a gold scatterer, which are provided in a tutorial by COMSOL, were used. They are based on the maximum skin depth of gold of $43.2\,\mathrm{nm}$ at $498\,\mathrm{nm}$ [154]. An advantage of FEM simulations is the ability to describe the electro-magnetic fields within one mesh element with polynomial functions, instead of constant values, leading to high accuracy even with rather coarse meshes, and thus to a decreased memory use [133].

3.3.2 Lumerical FDTD Solutions

Most of the optical simulations of nanostructures in this thesis were performed using the FDTD module by Lumerical. The FDTD module, as indicated by its name, computes optical properties using the finite-difference time-domain (FDTD) method. In this method, a light pulse is injected into the simulated structure and its propagation computed numerically by solving Maxwell's equations. To obtain spectral information, the Fourier transform is applied to the time-domain solution. This leads to significantly shorter computation times than for a spectrum obtained by FEM, where each frequency has to be calculated individually. Another advantage of FDTD is the use of separate rectangular grids for the electric and magnetic fields. The one is calculated from the other at each half-step in time [133]. This leads to a very efficient use of computational power and memory. A disadvantage of FDTD is the assumption that the fields are constant within one mesh element, which can lead to convergence problems if the fields change rapidly on a scale smaller than the mesh size.

In Lumerical FDTD, the size of the solely rectangular mesh is, to some extent, chosen automatically. Based on the refractive index of the different media, the number of mesh elements per wavelength can be adjusted from 1 to 5 (default is 2, chosen in all simulations in this thesis). However, if the automatic method is insufficient, the mesh size can additionally be refined

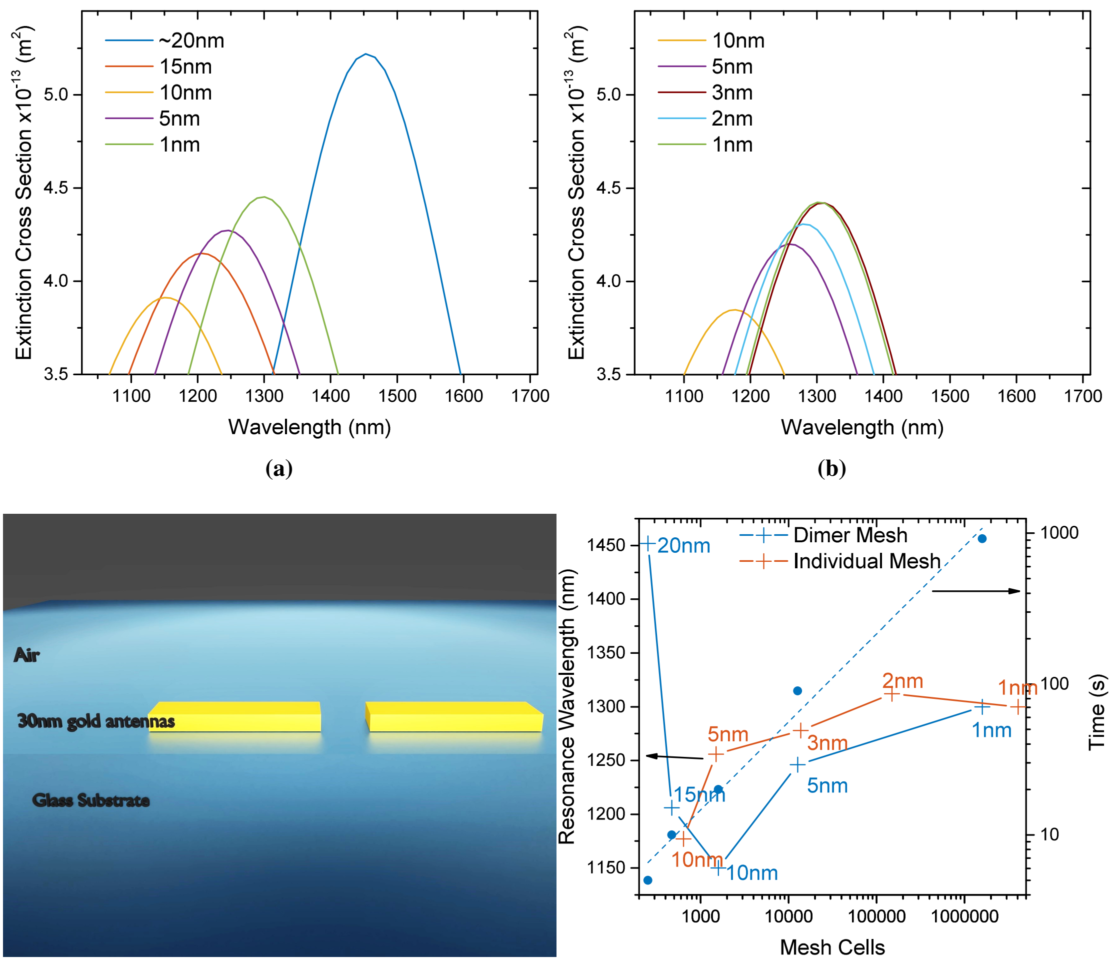

(a) (b) (c) (d)

Figure 3.5: (a, b) Extinction cross-sections calculated using Lumerical FDTD for a 250 nm x 100 nm x 30 nm antenna using different mesh constraints: (a) for a refined mesh volume matching the dimer antenna size (530 nm x 100 nm x 30 nm); (b) For a volume matching one of the antenna arms plus one mesh element in each direction. (c) Schematic of the simulated structure. (d) Resonance wavelength and simulation time depending on the number of mesh cells inside the refined mesh volume.

inside a chosen volume, the so-called mesh constraint, which is necessary to efficiently simulate nanoparticles.

To quantify the necessary mesh refinement, the simple setup of a gold dimer antenna on a glass substrate was chosen. The antenna size was set to 250 nm length, 100 nm width and 30 nm height with a gap of 30 nm. Its expected response is between 1200 nm and 1400 nm as known from experimental results. Typically, the resonance wavelength in a numerical model converges with decreasing mesh size towards a final value, which would be reached for an infinitely thin mesh [151]. In the following discussion, the resonance wavelength for a 1 nm-mesh will be used as the final value, since the topic of discussion are the deviations from monotonous convergence that were observed. The extinction cross-section spectra of the dimer antenna are shown in Fig. 3.5(a–b). The spectra in Fig. 3.5(a) were calculated in a simulation where the volume of the manual mesh constraint was as large as the whole dimer antenna (including the gap). Here, the case of $20\,\mathrm{nm}$ is the unconstrained mesh that Lumerical creates automatically when using the lowest mesh density settings. In Fig. 3.5(b), the volume of the mesh constraint had the size of one antenna arm plus one mesh element. This was done because it was noted that the mesh element edges rarely coincided with the material interfaces, meaning that the size of the antenna was not adequately represented. Especially the meshing inside the gap was improved this way. Choosing the mesh constraint size one element larger than the antenna is recommended by the Lumerical manuals to ensure that the mesh and the material boundaries match. By using symmetry, the edges of both antenna arms are represented correctly.

For the first mesh constraint, which covers both antenna arms and the gap, if the mesh size is larger than $5\,\mathrm{nm}$, as the gap is a comparable length scale ($30\,\mathrm{nm}$), the discretisation error becomes significant. For example, for a mesh size of $10\,\mathrm{nm}$, the first element from $x = 0$ to $x = 10$ would represent air and the second element from $x = 10$ to $x = 20$ would exhibit the average refractive index between air and gold. Due to this effect, the mesh size inside the refinement volume has to be chosen carefully.

Figure 3.5(d) shows the resonance wavelength and the computation time depending on the number of mesh cells inside the refined mesh volume on a double log-scale. The resonance wavelength is given by crosses connected with solid lines. Labels give the mesh element size. The computational time is indicated by circles, to which a linear function was fitted, shown in dashed lines. With increasing mesh density, more resources are needed, increasing the computation time. The slope of the linear fit is 0.589 for the larger refined mesh volume, which gives a proportionality of $t_{\text{comp}} = n_{\text{mesh}}^{0.589}$ for the computation time depending on the number of mesh cells inside the refined mesh volume.

Additionally plotted in Fig. 3.5(d) is the resonance wavelength of the dimer antenna as obtained by the different mesh constraints. Typically, an increased mesh density goes along with an asymptotic increase in the peak of the extinction cross-section, while the resonance wavelength approaches a final position asymptotically [133, 155]. For the investigated geometry, the final resonance wavelength position is not monotonously approached. Instead, there are deviations to higher and lower resonance wavelengths, which are attributed to the fact that the antenna size is not exactly matched by the mesh cells in those cases. For the larger mesh constraint, an exact antenna size and gap match is given for the $1\,\mathrm{nm}$ spectrum. The smaller mesh constraint maps the antenna size and gap accurately in all cases except the one for $2\,\mathrm{nm}$, which can be seen to deviate from the trend of increasing resonance wavelength with decreasing mesh element size. The $1\,\mathrm{nm}$ spectrum of the larger mesh constraint fits exactly to the $1\,\mathrm{nm}$ spectrum of the smaller constraint, indicating again that the observable variations are due to the size matching of the simulation mesh. For future simulations, the $5\,\mathrm{nm}$ meshing with the smaller mesh constraint was chosen to get a reasonably accurate result while saving computation time. The difference between the resonance wavelength position compared to the $1\,\mathrm{nm}$ case is less than 5%.

Different spectral ranges also influence the computation time of Lumerical simulations, however only indirectly. A broad spectral range will be simulated with a short pulse of light, and the simulation's time step size decreases automatically with decreasing pulse duration. Very broad spectral ranges will therefore significantly increase computation time.

3.3.3 Comparison of Lumerical and COMSOL simulations

During the simulations of one of the designs for electrical control of gold nanoantennas, a discrepancy between the behaviour of Lumerical and COMSOL was observed. While COMSOL simulations performed by Dr. Martina Abb showed a decrease of the resonance amplitude with increased optical coupling, spectra obtained from Lumerical for the same design showed the opposite trend. The discrepancy occurred as soon as a TiN bottom contact was included in the simulations. It was therefore found necessary to analyse the two simulation models in detail.

The general layout is shown in Fig. 3.6(a). The individual layer thickness is $d_1 = 200\,\mathrm{nm}$ in the simulations where TiN was included, $d_2 = 50\,\mathrm{nm}$ to $150\,\mathrm{nm}$ for the HfO_2 thickness sweep and $d_3 = 120\,\mathrm{nm}$ for all ITO layers. Simulations of the structure were done in Lumerical and are shown in Fig. 3.6(b) as a function of HfO_2 thickness. The results were compared to the COMSOL simulations shown in Fig. 3.6(c).

HfO_2 and TiN have higher refractive indices than glass, leading to a general red-shift of the plasmonic resonance. As shown in Fig. 3.6(b), a HfO_2 substrate correlates to an antenna resonance at $1542\,\mathrm{nm}$. If TiN is included, the resonances are further red-shifted. Increasing the HfO_2 thickness results in further red-shifts. This implies that though TiN has a higher refractive index than HfO_2, in the Lumerical simulations there is no red-shift of the resonances with decreasing HfO_2 thickness. As known from experiments with multi-particle systems, coupling between the gold nanoantenna and the TiN contact should also lead to a broadening of the extinction cross-section amplitude, while again the opposite is observed. The COMSOL computations, on the other hand, follow the expectations described above: the thinner HfO_2 layer leads to a low-amplitude, red-shifted resonance. The COMSOL simulations shown in Fig. 3.6(c) for slightly different antenna dimensions and SiO_2 insulator were repeated for the exact same device as those in the Lumerical simulations and the discrepancy between the two softwares persisted.

Figure 3.6(d) summarises the simulations with varying HfO_2 thickness. Without TiN, the simulations from Lumerical and Comsol match closely (not shown). For purely dielectric substrates, the resonance red-shift from the presence of HfO_2 seems to saturate for a HfO_2 thickness of $100\,\mathrm{nm}$. An increase in HfO_2 thickness then gives no further wavelength change. In the presence of a TiN back contact, red-shifts are observed even for more than $100\,\mathrm{nm}$ HfO_2. The results from COMSOL on the other hand show a reduction of the resonance wavelength with increasing HfO_2 thickness. Another important aspect is that the lines of the Lumerical simulations with and without TiN do not approach each other. This means that the presence of TiN fundamentally changes the behaviour of the antenna resonances even when it is further away

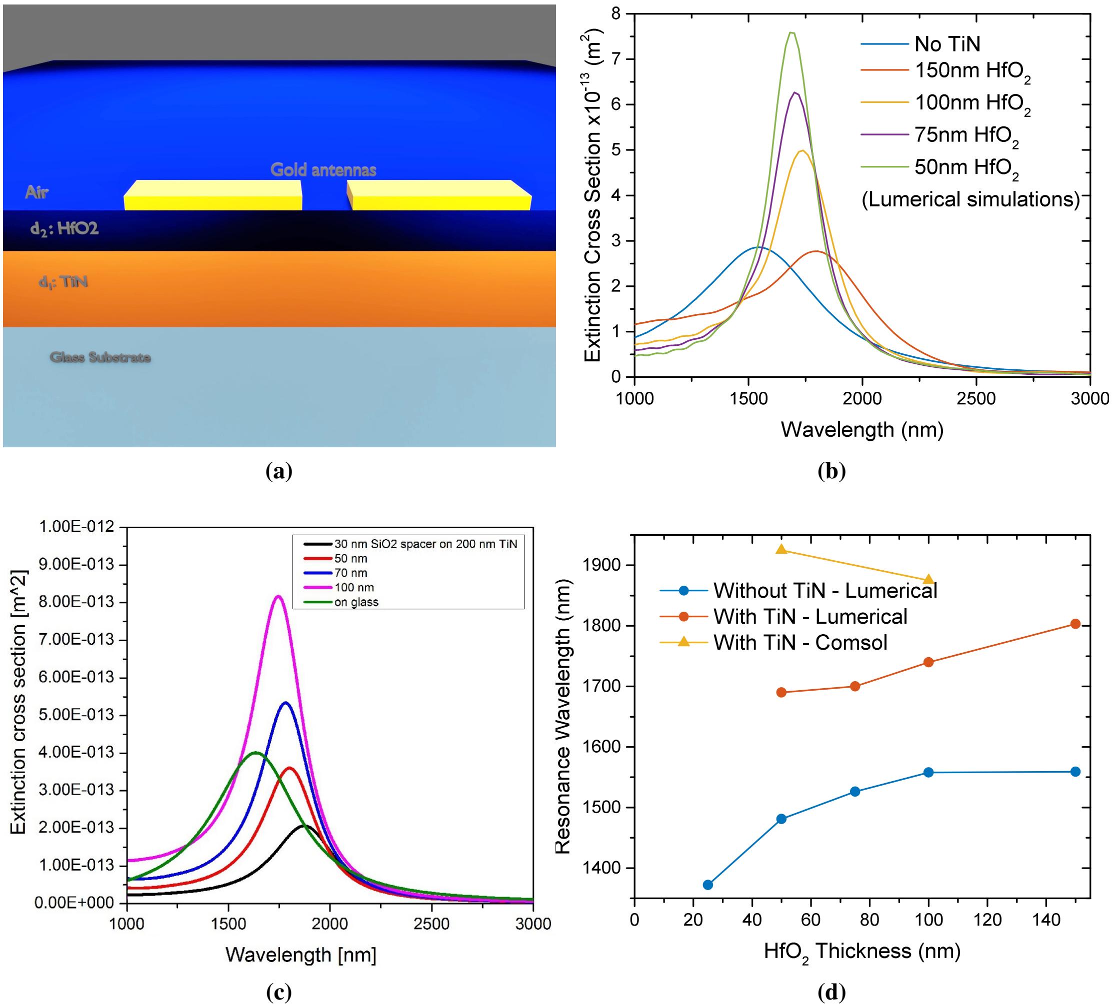

(a) (b)

(c) (d)

Figure 3.6: (a) Schematic of the analysed structure, consisting of a ITO-HfO_2-TiN stack on a glass substrate. A gold dimer antenna is embedded in the ITO. $d_1 = 200\,\mathrm{nm}$, $d_2 = 50\,\mathrm{nm}$ to $150\,\mathrm{nm}$ and $d_3 = 120\,\mathrm{nm}$. (b, c) Resonance wavelength of an antenna with $250 \times 100 \times 30\,\mathrm{nm}^3$ arms and $30\,\mathrm{nm}$ gap size: (b) from Lumerical FDTD, (c) previous COMSOL results of an antenna with $290 \times 80 \times 20\,\mathrm{nm}^3$ arms and $20\,\mathrm{nm}$ gap size by Dr. Martina Abb. (d) Resonance peak wavelength extracted from both plots (b) and (c), as a function of HfO2 thickness.

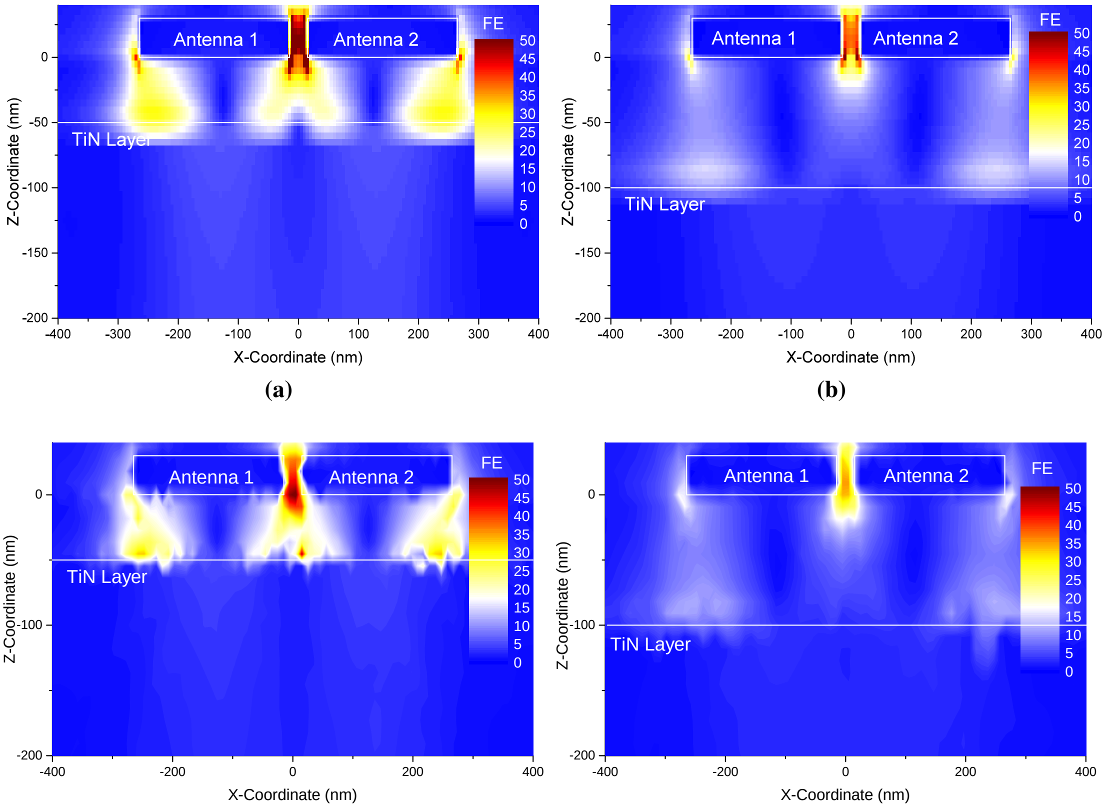

(a) **(b)**

(c) **(d)**

Figure 3.7: Vertical cross-section of the normalised electric field distribution (field enhancement) of an antenna with $250 \times 100 \times 30\,\mathrm{nm}^3$ arms and $30\,\mathrm{nm}$ gap size. The antenna is positioned on top of a $200\,\mathrm{nm}$ TiN and a HfO_2 layer of (a, c) $50\,\mathrm{nm}$ or (b, d) $100\,\mathrm{nm}$ thickness, respectively. (a, b) Simulations using Lumerical FDTD; (c, d) using COMSOL Multiphysics.

than the antenna near-field reaches. This is most likely due to the strong back reflections caused by the TiN, resulting in standing waves and other interference patterns that change the interaction between the antennas and the incoming light.

A further analysis of the differences of COMSOL and Lumerical was done by plotting the electric near-field of the antennas at resonance, as shown in Fig. 3.7. The plots show the vertical cross-section of the electric field enhancement (FE) around the antenna and inside the substrate. The substrate-air interface is located at $z = 0$ and the top of the TiN layer is marked in the plots. In-between the air and the TiN lies HfO_2 with a thickness of $50\,\mathrm{nm}$ (Fig. 3.7(a, c)) or $100\,\mathrm{nm}$ (Fig. 3.7(b, d)). The Lumerical simulations are shown in Fig. 3.7(a, b), COMSOL simulations with their triangulated mesh in Fig. 3.7(c, d). The Lumerical plots were normalised by dividing them by the background electric field without antenna, while for the COMSOL simulations this is done automatically during the computation. The agreement between Lumerical and COMSOL is striking, both in the near-field distribution and the peak field enhancement. However, the COMSOL near-field in Fig. 3.7(c) seem to be asymmetric, which can create artifacts such as the field intensity spike near the TiN surface. At $50\,\mathrm{nm}$ HfO_2 thickness, a strong coupling between the gold antenna and the TiN back contact is obvious from the vertical distribution of the field enhancement. With increasing HfO_2 thickness, this coupling weakens significantly in both softwares. The field enhancement with $50\,\mathrm{nm}$ HfO_2 is 70, and up to 40 with $100\,\mathrm{nm}$ HfO_2.

Both software show a reduction in field enhancement with increased HfO_2 thickness (Fig. 3.7). In agreement with this, Lumerical showed a reduction of the extinction cross-section enhancement (Fig. 3.6). In contrast, COMSOL showed an increase in extinction cross-section enhancement. Since extinction cross-section enhancement and the near-field enhancement of an antenna are directly connected, the behaviour of COMSOL is paradoxical. Therefore, the Lumerical simulations were judged to be correct and COMSOL erroneous. In a comparison of simulation methods for plasmonics, the two methods were found equivalent for complex 3D structures [156]. Why COMSOL displayed the contradictary behaviour could not ultimately be determined, but may be due to an incorrect setup of the model. That the expected behaviour of a dampened and broadened resonance, which was shown by the COMSOL simulations, is contradicted in the Lumerical simulations could be due to the influence of constructive and destructive interference by the light reflected from the TiN.

3.3.4 Electrical simulations using Lumerical DEVICE

DEVICE is the electrical solver of Lumerical and enables calculation of carrier densities and band shapes, which can then be used as parameters for the optical solver. DEVICE assumes simple material properties for metals (perfect conductors) and dielectrics (perfect insulators), while allowing complex description of the electrical behaviour of semiconductors. Band gap, carrier mobilities, radiative and non-radiative recombination, and contact properties are some of the attributes that can be defined in DEVICE. Like COMSOL, DEVICE also uses FEM with triangular meshing to compute the drift-diffusion equations for an applied voltage. DEVICE needs significantly more memory for the same volume than FDTD, mostly because a finer mesh is needed to accurately compute carrier diffusion compared to optical propagation. This issue is partially solved by using 2D simulations to adjust the mesh to the strength of the possible carrier modulation before solving the model in 3D.

For the simulations in this thesis, gold and TiN are modelled by their work function of $5.1\,\mathrm{eV}$ and $4.5\,\mathrm{eV}$, respectively. HfO_2 is defined by its DC-permittivity of 25. To model ITO, its bandgap was set to $4\,\mathrm{eV}$, the DC-permittivity to 9.3 and the work function to $4.5\,\mathrm{eV}$ [37, 68, 90].

Analytically, the accumulation of charges at a semiconductor-insulator interface can be described by the Thomas-Fermi screening theory [90, 94]. Assuming a rectangular charge

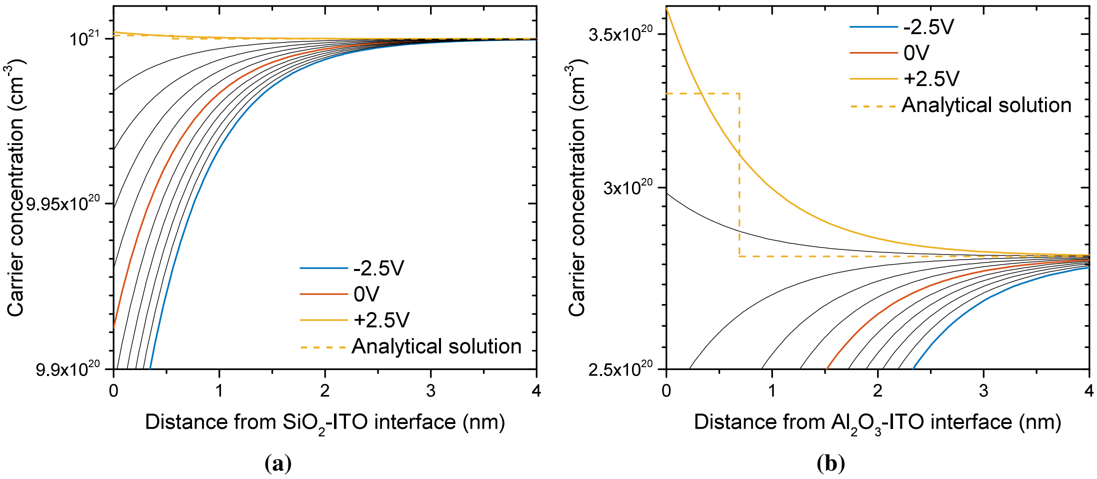

(a) **(b)**

Figure 3.8: Carrier modulation inside ITO for two different structures presented in the literature: (a) Simulated for the geometry of reference [82], (b) the geometry of reference [119]. The modulation calculated with Thomas-Fermi screening theory (Eqs. 3.4 and 3.5) for the maximum positive voltage is added as a dashed line for accumulation. Black lines mark increments of the applied voltage of $0.5\,\mathrm{V}$.

distribution, it defines the carrier concentration $N_i(z)$ induced by an applied voltage inside the semiconductor as:

$$N_i(z) = N_0 - \frac{\varepsilon_0 \epsilon_{\text{ins}}}{e} \frac{V(z)}{d_{\text{ins}}^2}, \tag{3.4}$$

where N_0 is the bulk carrier concentration, ϵ_{ins} the static permittivity of the insulator, $V(z)$ the applied voltage and d_{ins} the thickness of the insulator. The equation is valid for small applied voltages (eV less than the Fermi energy). For the structure used by Feigenbaum et al. [82], where a voltage of $2.5\,\mathrm{V}$ was applied over a SiO_2 insulator of $100\,\mathrm{nm}$ thickness and ITO with a bulk carrier concentration of $10^{21}\,\mathrm{cm}^{-3}$, equation 3.4 gives a resulting carrier concentration of $1.0001\times10^{21}\,\mathrm{cm}^{-3}$, meaning that the carrier concentration changes by $10^{17}\,\mathrm{cm}^{-3}$. To increase the amount of accumulated carriers, the applied voltage and the permittivity of the insulator need to be increased or the insulator thickness decreased.

Another critical parameter is the thickness of the accumulation layer which can be calculated as [90]:

$$l_{\text{acc}} = \left[\sqrt[3]{\frac{\pi^4}{3N_0}} \frac{\varepsilon_0 \epsilon_{\text{ITO}} \hbar^2}{m^*} \right]^{1/2}, \tag{3.5}$$

where $\hbar$ is the reduced Planck constant and $\epsilon_{\text{ITO}} = 9.3$ [93]. For the example above, we find (with $m^* = 0.4m_\mathrm{e}$) $l_\mathrm{acc} = 5.6\,\mathrm{Å}$. The calculated carrier distribution is shown in Fig. 3.8(a) together with the corresponding result from DEVICE. Figure 3.8(b) gives the results for the paper from Huang et al. [119], using a $5\,\mathrm{nm}$ thick alumina insulator (ϵ_ins=9). The resulting values are $d = 6.9\,\mathrm{Å}$ and $N_i(0) = 3.3 \times 10^{20}\,\mathrm{cm}^{-3}$. The graphs show a good agreement between theory and simulation in terms of the total amount of carriers moved.

For unstructured optical samples, the Thomas-Fermi screening theory is sufficient to describe the effect of charge accumulations on reflection and transmission. For nanoantennas with their high field confinement, the exact charge distribution, as can be obtained from DEVICE, needs to be used. Especially if the ITO locally crosses the ENZ region, optical effects can no longer be described by an averaged charge distribution. As can be seen in Fig. 3.8, the numerically calculated charge distributions are exponential curves instead of rectangular, which comes from the fact that the last term in equation 3.4 is actually the derivative $\partial^2 V(z)/\partial d_\mathrm{ins}^2$. The iterative solving algorithm results in exponential curves for N, E and V, which are self-consistent with derivation.

The results found in this section show the challenge in modulating plasmonic structures in the visible wavelength regime: to obtain plasmonic resonances in the visible part of the spectrum, high ITO carrier concentrations of the order of $10^{21}\,\mathrm{cm}^{-3}$ are needed. Yet with conventional MOS-structures based on $100\,\mathrm{nm}$-thick SiO$_2$, these high carrier concentrations can barely be modulated: the concentration change $N_i - N_0$ stays the same, yet with increasing N_0 the relative modulation strength $(N_i - N_0)/N_0$ decreases. To solve this problem, one has to either find unprecedented structures that allow orders of magnitude higher near-field confinement, or design the modulators for the infrared where significantly lower bulk carrier concentrations are sufficient. One also needs to maximise the spatial and spectral overlap of the antenna with the carrier modulation, i.e. the spatial overlap of the antenna near-field with the carrier modulation region and the spectral overlap of the resonance wavelength with the spectral position of the maximum refractive index change induced by the carrier modulation. The literature references described in section 1.2 all deal with infrared wavelengths, some at $4\,\mathrm{\mu m}$, others at the more challenging telecom wavelength of $1550\,\mathrm{nm}$. For the work in this thesis, the telecom wavelength was chosen as the target wavelength as well, due to its importance for optical communication.

4 Transparent conductive oxide based optical solar metareflectors

Optical Solar Reflectors (OSR) play a crucial role in the thermal control of a spacecraft, since they constitute the physical interface between the thermal management system and the space environment. Glued to the external skin of the radiator panels, OSRs are designed to reflect the solar radiation and to radiatively dissipate the heat that is generated on board. Reducing weight and thus launch costs by employing a metasurface-based, ultrathin, spectrally selective reflector that can be fabricated on top of hard substrates or flexible foils is the perspective that drove this project. As part of an EU project, extensive Lumerical simulations of the structure were done to optimise the design process before fabrication. This chapter will focus on the design optimisation as done by the author. The fabrication and measurements of the device were afterwards performed by Dr. Kai Sun. The device was realised with two materials for the active plasmonic structure: AZO and VO_2. While AZO is the main component, for which the design was optimised, experimental data using the thermally switchable material VO_2 will also be provided at the end of the chapter.

4.1 Introduction to optical solar reflectors

Current OSRs are mass-fabricated in the form of quartz tiles metallised on the radiator-facing surface [157]. The quartz absorbs and emits the thermal IR spectrum, while the silver metal layer reflects the solar spectrum. Quartz tile OSRs have excellent thermo-optical properties, that remain unaltered after long exposure to the space environment. However, quartz tiles are prone to break during assembly, and replacement of glued broken tiles is challenging. Additionally, quartz tiles add a significant amount of weight to the structure, thereby increasing satellite launch costs.

Optically, an OSR is a spectrally selective filter, that reflects those parts of the ultraviolet, visible and near infrared parts of the optical spectrum which correspond to the radiation spectrum of the sun. At the same time, an OSR emits the thermal infrared spectrum corresponding to that of a black body at 300 K. The performance of an OSR is characterised by the two thermo-optical parameters α (solar absorptance) and ϵ (IR emissivity), where α is required to be close to 0 and ϵ to be close to 1 [158]. Quartz tiles exhibit values of $\alpha = 0.11$ and $\epsilon = 0.8$ [159].

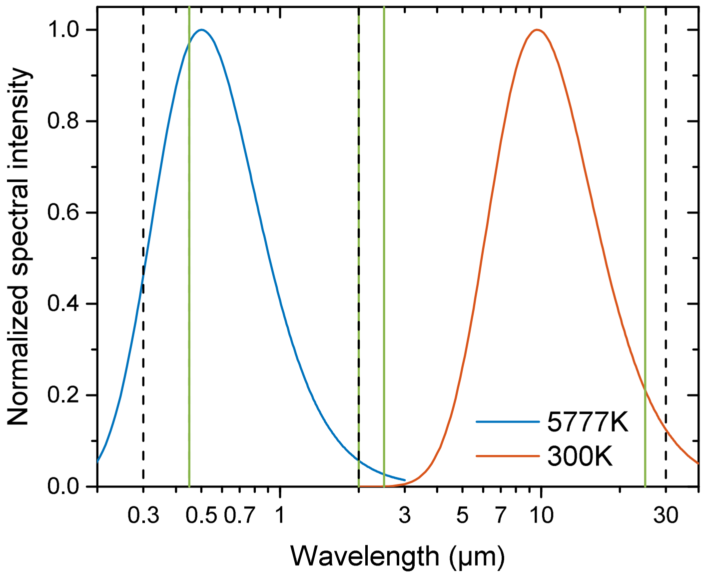

Figure 4.1: Blackbody radiation spectra for a black body at 5777 K and 300 K. The dashed black lines show the boundaries of the definition of α and ϵ, the green solid lines show the boundaries of the available measurement tools.

The absorptance in the visible and the emissivity in the infrared part of the spectrum can be quantified by the following factors [160]:

$$\alpha, \epsilon = \frac{\int_{\lambda_1}^{\lambda_2}(1-R(\lambda))B(\lambda,T)d\lambda}{\int_{\lambda_1}^{\lambda_2}B(\lambda,T)d\lambda}, \tag{4.1}$$

where $R(\lambda)$ is the spectral reflectance and $B(\lambda, T)$ the black body radiation at temperature T. This way, the reflectivity is spectrally weighted to give the best overlap with the irradiation from a black body. The spectral ranges of interest are shown in Fig. 4.1. For α, the surface temperature of the sun $T = 5777\,\mathrm{K}$ is used, and the integration limits set to λ_1=300 nm and λ_2=2000 nm. This includes 90.6% of the total black body energy, with 3.5% being left on the short-wavelength side and 5.9% on the long wavelength side. For ϵ, the temperature is set to $T = 300\,\mathrm{K}$, $\lambda_1 = 2\,\mu\mathrm{m}$ and $\lambda_2 = 30\,\mu\mathrm{m}$, which includes 89.1% of the total black body energy, with $10^{-5}\%$ not included on the short-wavelength side and 10.9% on the long wavelength side. Thus, the spectral range of interest spans two orders of magnitude. The measurable range indicated by the green vertical lines in Fig. 4.1 is smaller than the defined spectral range. The influence of this limitation will be quantified in section 4.4.

The thermal equilibrium of a body can be described by [158]:

$$A_s\sigma_{\mathrm{sol}}\alpha = A_e s\epsilon T^4, \tag{4.2}$$

where A_s is the area exposed to solar radiation, $\sigma_{\mathrm{sol}} = 1367\,\mathrm{W\,m^{-2}}$ is the solar constant, A_e is the emitting surface area of the body and $s = 1.38 \times 10^{-23}\,\mathrm{J\,K^{-1}}$ is the Stefan-Boltzmann constant. Solving this equation for the temperature renders

$$T = \sqrt[4]{\frac{A_s \sigma}{A_e s} \frac{\alpha}{\epsilon}}. \tag{4.3}$$

Apart from the ratio of the surface areas, which are determined by the satellite's dimensions, this equation scales only with the inverse of ϵ/α. This is why this value is the figure of merit for the design, indicating the strength of emission relative to the absorptance of the structure.

An alternative to currently used quartz tiles are Ag-FEP-foils, where the quartz tile is replaced by a flexible foil of fluoro-ethylene polymer (FEP) as the IR emitter, providing flexibility [157]. However, Ag-FEP-foils lack the thermo-optical performance and durability of quartz OSRs. A metasurface-based alternative has to provide a long-lasting solution with good thermo-optical parameters. In the approach used for this project, AZO is used as the plasmonic material instead of metals, since it behaves as a low-loss dielectric in the visible range. By carefully choosing the carrier concentration of the material, the transition wavelength can be placed so that ϵ is maximised and α minimised. As a free-standing structure, plasmonic particles cannot absorb 100% of the incoming radiation. This is solved by placing the metasurface on a metal reflector, separated by a dielectric spacer, similar to a Salisbury screen [161]. The reflector provides constructive interference of IR radiation at the position of the metasurface, and also provides reflection in the visible range. The dielectric nature of AZO in the visible range prevents higher order plasmonic resonances and thereby decreasing α. This is a key advantage over metal-based metasurfaces.

4.2 Meta-OSR design

The structure consists of three layers: the back reflector, the spacing layer and the meta-surface. The schematic of the structure is shown in Fig. 4.2. The back reflector can be made of silver or aluminium, both of which are good reflectors in the visible and IR spectral range. While silver has the higher average reflectivity in the visible spectrum, it has a bandgap at around $350\,\mathrm{nm}$, thereby increasing absorption in the ultraviolet. Aluminium on the other hand has a lower average reflectivity and weak bandgap absorption at $800\,\mathrm{nm}$. Simulated absorption spectra for a $100\,\mathrm{nm}$ thick layer of the respective metal are shown in Fig. 4.3(a). The solar absorptance is 0.078 for Al and 0.058 for Ag, based on literature data for the metals' optical constants [153]. These values represent the minimum absorptance values possible with the respective reflector. In the experiments, the dielectric spacers were prone to peel off of silver due to poor adhesion on native

AgO. Therefore, Al was chosen as reflector for the fabricated structures.

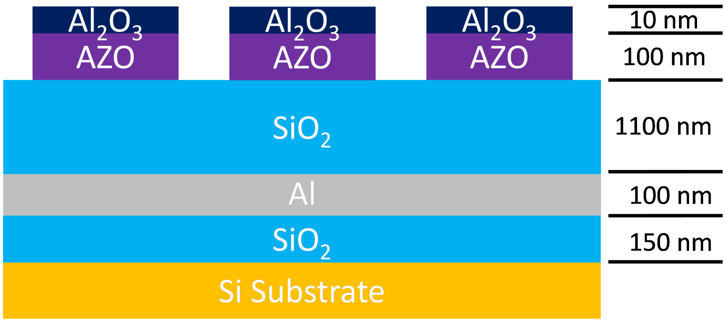

Figure 4.2: Schematic cross-section of the metareflector, consisting of a back reflector, a dielectric spacer and a patterned TCO meta-surface.

The spacer layer of the structure is designed to create a standing wave between the incoming and the reflected radiation, with a maximum field intensity at the position of the AZO meta-surface. This works similar to a $\lambda/4$-spacer, however due to the complex permittivity ε_r of common dielectrics in the IR and the cross talk of the meta-surface with the reflector, the optimum spacer thickness varies with AZO carrier concentration and generally with changing top material. The permittivity of the spacer material is an important parameter as its dispersion allows the AZO absorption to broaden while also negatively impacting ϵ through phonon resonances. Figure 4.3 (b) shows the real part of the permittivity ε_r' of several dielectric spacer materials. In the mid-IR range, most materials show absorption bands due to phonon vibrations, which show as perturbations in ε_r'. These so-called reststrahlen bands have an increased reflectivity and exhibit spectral regions where the real part of the dielectric permittivity becomes negative [162]. As was described in section 2.2, the real part of the permittivities of the antenna material and the environment must have opposite signs for a plasmonic resonance to occur. That is why to achieve a plasmonic resonance in the AZO at a certain wavelength, the dielectric needs to have $\varepsilon_r' > 0$, otherwise the plasmon resonance is quenched. Infrared transparent materials like fluorides lack phonon bands in the thermal infrared, but were not used for this work. Fabrication is substantially more complicated and they are generally more brittle and prone to damage than oxides.

To evaluate the influence of the dielectric spacers' dispersion on the IR performance, numerical calculations of the meta-OSR design were evaluated using Lumerical FDTD. The resulting spectra from a metareflector with an insulator thickness of $1130\,\mathrm{nm}$, a carrier concentration of $2 \times 10^{20}\,\mathrm{cm}^{-3}$, a square size of $950\,\mathrm{nm}$ and a $250\,\mathrm{nm}$ gap are shown in Fig. 4.3 (c). The normalised spectrum for a TCO rectangle in air is given for comparison. The perturbations in ε_r' of the spacer materials lead to heavily distorted absorption spectra in the infrared, quite different to that in air. For all these materials, the design parameters result in near unity optical

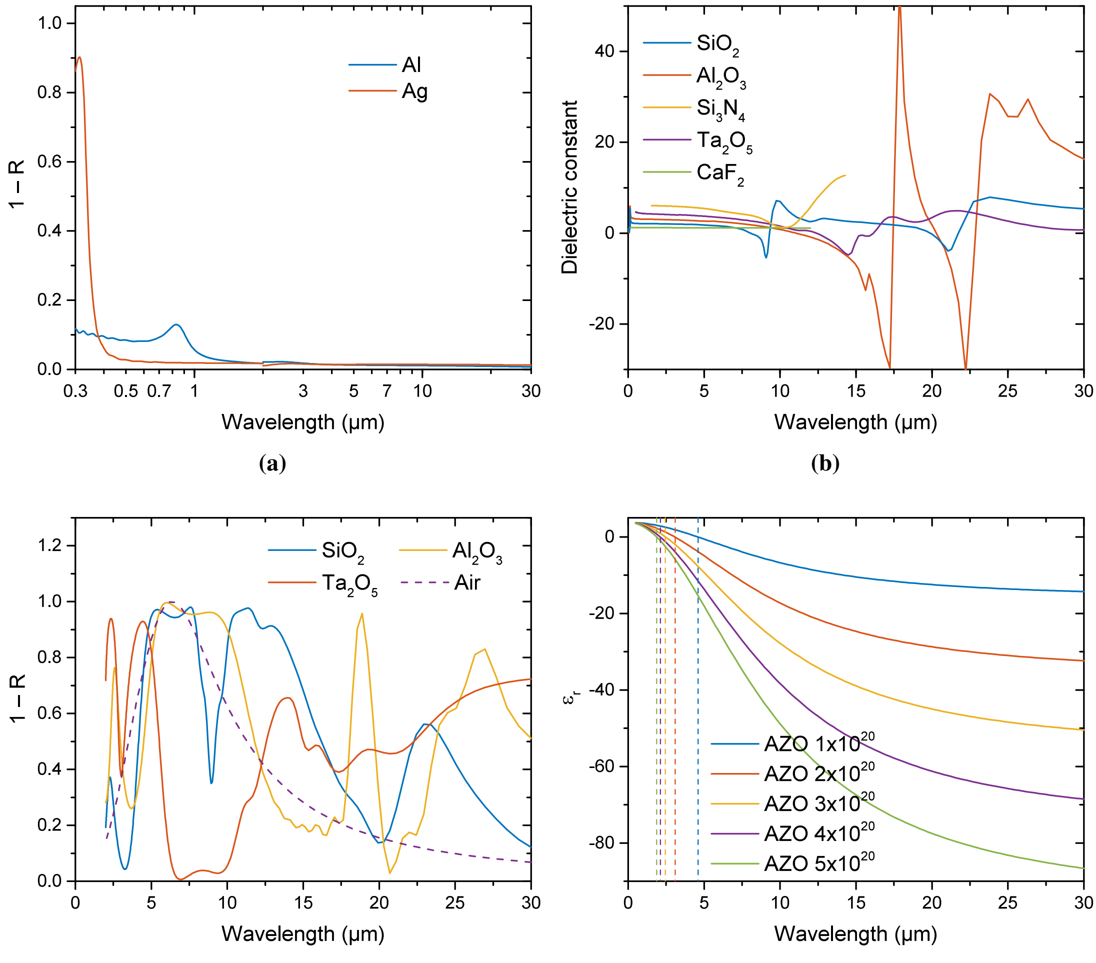

(a) **(b)**

(c) **(d)**

Figure 4.3: (a) Reflectivity of 100 nm thick silver and aluminium films, based on literature data [153]. (b) Real part of the permittivity of different spacer materials. (c) Simulated spectra for different dielectric spacer materials using the full structure device with an insulator thickness of 1130 nm, a carrier concentration of $2 \times 10^{20}\,\mathrm{cm}^{-3}$, a square size of 950 nm and a 250 nm gap. The spectrum for air is added for comparison. (d) Real part of the permittivity of transparent conductive oxides as a function of wavelength and carrier concentration. The vertical lines represent the transition wavelength, where $\epsilon = 0$.

absorption in a spectral window around $10\,\mu\mathrm{m}$, the peak of the 300 K blackbody radiation. The emissivity values are 0.667 for SiO_2, 0.586 for Al_2O_3 and 0.357 for Ta_2O_5. SiO_2 shows narrow perturbation regions at 10 µm and 21 µm, and supports a particularly broad absorption range, which is attributed to the dispersion of the material resulting in an extension of the constructive interference condition. Absorption compared to the case in air is thus significantly enhanced.

Following the choice of back reflector and dielectric spacer, the choice of the metasurface plasmonic material and its parameters is crucial for the device performance. AZO is a transparent conductive oxide whose optical properties largely depend on the carrier concentration, which in turn can be tuned over a wide range by varying deposition conditions. Its electrical permittivity can be described using a Drude-Lorentz model, as was done in chapter 2 in equation 2.1 and equation 2.3. For the design process, the TCO material values from the Drude model in that chapter were used.

Connected to the unique properties of AZO is the transition wavelength λ_t at which ε_r' changes sign. For wavelengths shorter than λ_t, AZO behaves like a dielectric, while for wavelengths larger than λ_t, it behaves like a metal and supports plasmonic resonances. As was shown in chapter 2, λ_t and thus the lower wavelength limit for plasmonic resonances is anti-proportional to the square root of the carrier concentration. Figure 4.3 (d) shows ε_r' for TCOs with carrier concentrations from $1 \times 10^{20}\,\mathrm{cm}^{-3}$ to $5 \times 10^{20}\,\mathrm{cm}^{-3}$. The dashed vertical lines mark the transition wavelengths of the materials. Due to its large transition wavelength, a carrier concentration of $1 \times 10^{20}\,\mathrm{cm}^{-3}$ is not feasible for the device in question. The higher carrier concentrations with transition wavelengths of $3\,\mu\mathrm{m}$ and lower are preferred.

The combined effect of spacer dispersion and meta-OSR design results in a broad absorption spectrum which can be further optimized by tuning the parameters of the AZO carrier density, spacer thickness and feature size. Figure 4.4 summarizes the optimization of design parameters. Figures 4.4 (a) and 4.4 (b) show colormaps of IR spectral reflectivity versus meta-OSR square size. The corresponding values of ϵ are plotted in Figs. 4.4 (c),(d) for the carrier densities of $2\times10^{20}\,\mathrm{cm}^{-3}$ and $3\times10^{20}\,\mathrm{cm}^{-3}$, which were identified as the near optimum values. The insulator material is SiO_2, the reflector material aluminium. While the lower carrier concentration gives broader resonances, the spectra for the higher carrier concentrations have a higher amplitude. The maximum emissivity values are $0.79 - 0.80$ for $2\times10^{20}\,\mathrm{cm}^{-3}$ and $0.77 - 0.78$ for $3\times10^{20}\,\mathrm{cm}^{-3}$, which are reached over a range of 150 nm of the insulator thickness and 400 nm of the square size. The ranges show good tolerances of the optical response to dimensional variations, which is an advantage over plasmonic structures made of metals, which are more sensitive to size changes due to the larger change of permittivity over the wavelength.

To conclude the design process, the figure of merit of the meta-surface is considered. To that end, the emissivity and absorptance of the same structure (1300 nm of SiO_2, $2 \times 10^{20}\,\mathrm{cm}^{-3}$ carrier concentration) are plotted in Fig. 4.5(a) as a function of the AZO fill factor on the surface. As can be seen, both values are low for a structure without any AZO and one covered completely, and have a maximum around 75%. At this point it is important to mention a systematic issue that was found with the FDTD simulations in the visible range, when simulating a patterned structure. Since the wavelength is on the same order of the pattern size, diffraction was observed, as also occurs in the experiment, yet the FDTD simulations additionally showed large absorption spikes at random wavelengths. This could be traced down to the inability of the FDTD software to

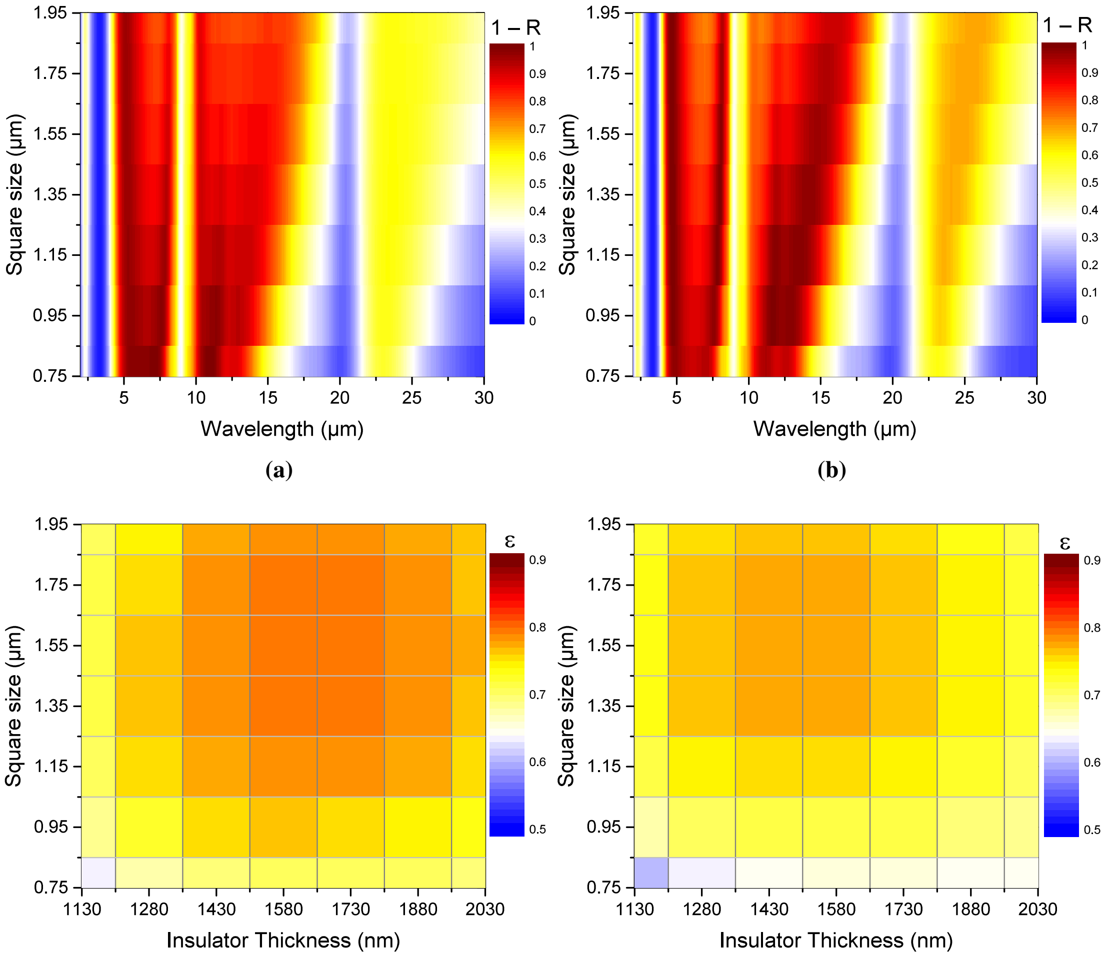

(a) **(b)**

(c) **(d)**

Figure 4.4: (a, b) $1-R$-spectra of the full structure as a function of square size, using 1130 nm of SiO_2 and a TCO carrier concentration of (a) $2\times10^{20}\,\text{cm}^{-3}$ and (b) $3\times10^{20}\,\text{cm}^{-3}$. (c, d) Emissivity values (ϵ) for a 2D-sweep of square size and insulator thickness with TCO carrier concentrations of (c) $2\times10^{20}\,\text{cm}^{-3}$ and (d) $3\times10^{20}\,\text{cm}^{-3}$.

account for diffraction at 90°. Energy that travels at 90° to the structure's surface never reaches the reflection monitor used to measure reflection in the model. It therefore increases the measured absorption above the correct value.

To circumvent this issue, which increases the simulated solar absorptance values above those obtained in reality, the effects contributing to absorption in the metareflector were investigated. Apart from the reflector losses, which are constant over fill factor, the bandgap absorption of AZO in the UV is the main contributor. This absorption scales linearly with fill factor and can therefore be obtained by the dashed line in Fig. 4.5(a), which connects the 0% and the 100% fill

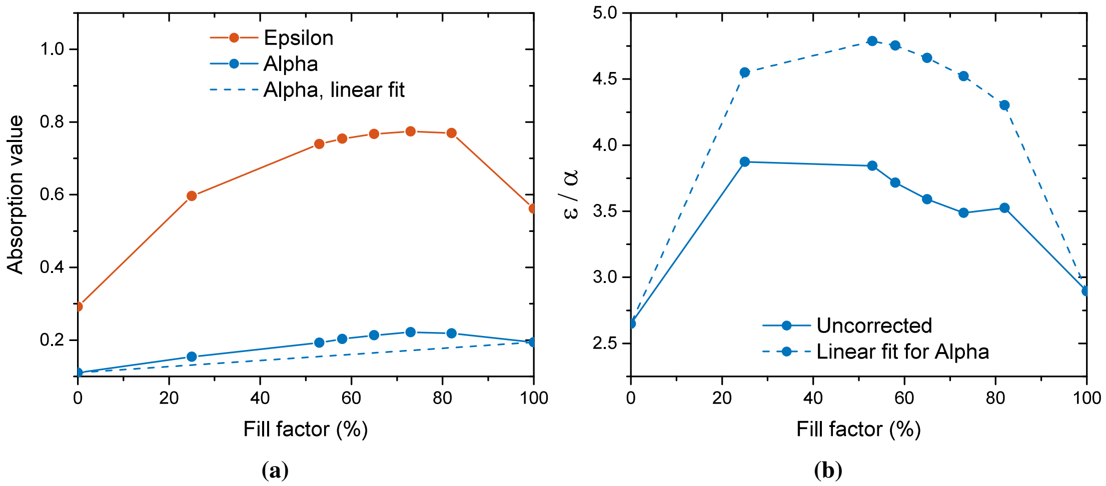

Figure 4.5: (a) Emissivity and solar absorptance for a structure with a carrier concentration of $2 \times 10^{20}\,\mathrm{cm}^{-3}$ and an insulator thickness of 1300 nm as a function of fill factor. The straight line between the two planar cases 'no TCO' (0% FF) and 'unpatterned TCO' (100% FF) represents the expected scaling of α. (b) Figure of merit ϵ/α for the values given in (a).

factor points. The figures of merit obtained from the simulated solar absorptance values and the linear fit are given in Fig. 4.5 (b). Ratios close to 5 are obtainable with the current structure.

4.3 Fabrication and characterisation of the AZO-based metareflector

Figure 4.6(a) shows the SEM cross-section of the designed meta-reflector. The oxide-insulator-metal stack was fabricated on a SiO_2-coated silicon substrate, with the top patterned AZO as the electric resonator, a SiO_2 spacer in middle and the bottom aluminium as an optical mirror. The AZO was designed as square arrays with sizes from 750 nm to 1350 nm in steps of 200 nm, and gaps between the squares of 150 nm and 250 nm. Each array has a size of $120 \times 120\,\mu\mathrm{m}^2$, leaving adequate area for FTIR and other optical characterisations.

The 80 nm aluminium layer was sputtered onto the substrate, followed by 1100 nm SiO_2 by PECVD. Afterwards, a 100 nm AZO layer and a 10 nm Al_2O_3 capping were deposited by thermal ALD. In Fig. 4.6(b), the polycrystalline structure of the deposited AZO can be seen. The 10 nm thin Al_2O_3 capping layer is required for the subsequent e-beam lithography process as ZnO was found to pose a serious adhesion issue with the chosen e-beam resist ZEP520A. The Al_2O_3/AZO layer was subsequently patterned by e-beam lithography and IBE. At the exposed areas, the Al_2O_3 and AZO layers were accurately removed, as can be seen in Figs. 4.6(c) and 4.6(d). They show SEM micrographs of the etched square patterns with 250 nm and 150 nm

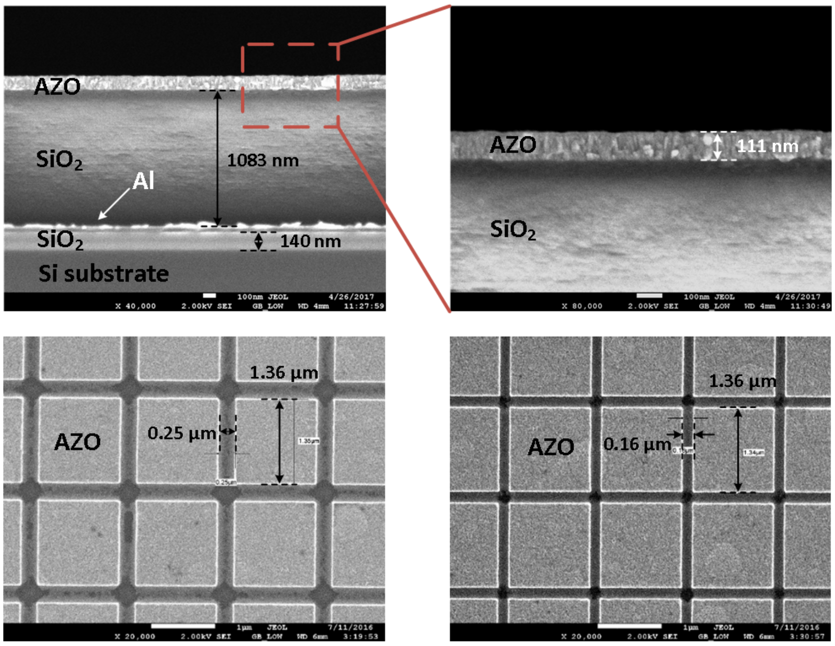

Figure 4.6: (a) SEM cross-section of the fabricated structure. (b) Zoom-in on the AZO film. (c, d) SEM top-views of patterned squares with designed edge lengths of 1350 nm and gaps of (c) 250 nm and (d) 150 nm.

gaps, respectively.

For the emissivity, FTIR measurements (2.5 µm to 25 µm) were taken using an 80 nm aluminium-coated SiO_2/Si substrate as reference. The solar absorptance was obtained by measuring the visible to near-IR reflectance using a total reflection setup based on an integrating sphere and a supercontinuum light source spanning a wavelength range of 0.45 µm to 2 µm with a two-detector system. For those measurements, a white surface made with TiO_2 nanoparticles was used as reference.

4.4 Results and discussion

The experimental spectra for the fabricated metareflectors, showing the spectra from both measurement systems stitched together, are shown in Fig. 4.7 for the two gap sizes of 150 nm and 250 nm. As can be seen, the absorption shown by the structure is low on the short-wavelength half and high on the long-wavelength half, as desired. An oscillating pattern in the spectra corresponds to interference between reflections from the top of the SiO_2 and from the reflector can be seen for most of the spectra up to 6 µm, where the refractive index of SiO_2 is no longer constant. The absorption in the IR range is stemming from the broad plasmon resonance of the AZO squares as shown before in Fig. 4.4(a). The effect of the pattern size can be seen in the

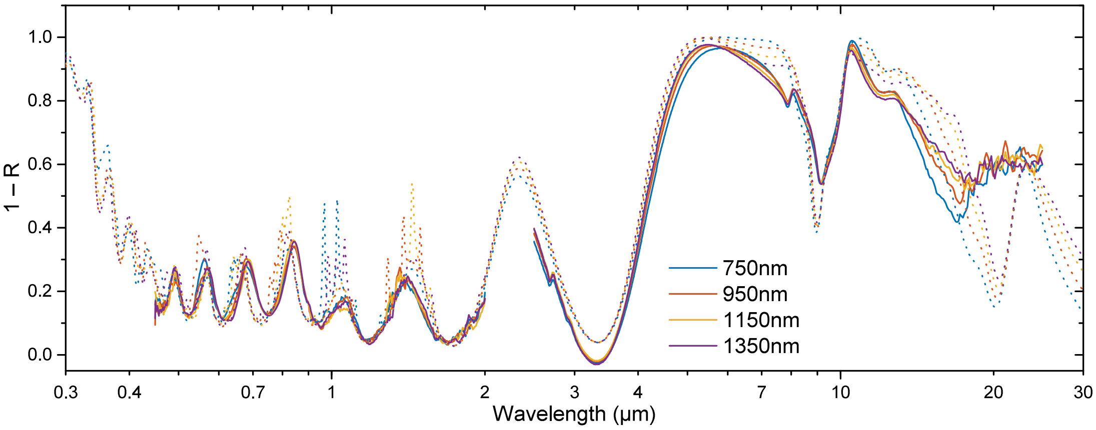

(a)

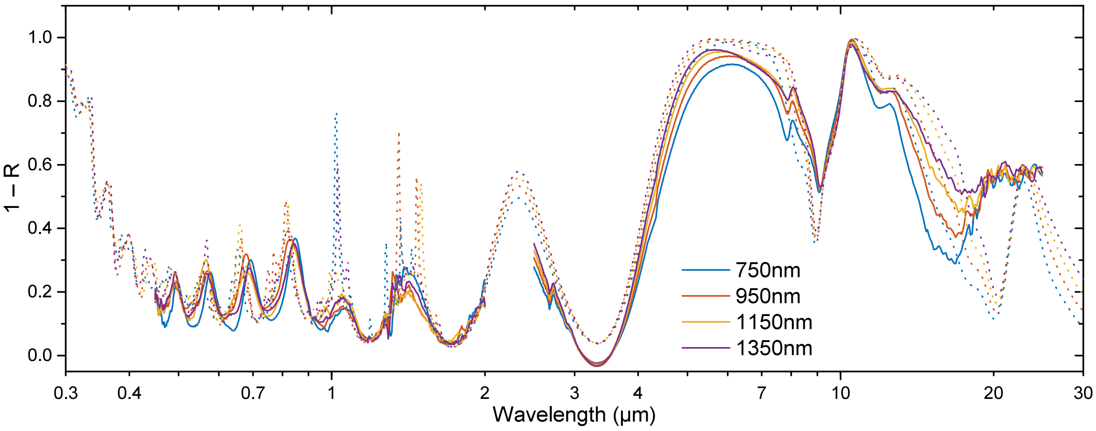

(b)

Figure 4.7: Full measured (solid) and simulated (dotted) spectra of the square patterns of indicated sizes: (a) for $150\,\mathrm{nm}$ gap size between the squares and (b) for $250\,\mathrm{nm}$ gap sizes.

broadening of the absorption peaks with increasing pattern size, especially at $5\,\mu\mathrm{m}$ and $17\,\mu\mathrm{m}$.

To fit the simulations to the experimental spectra, the Drude parameters of AZO were adjusted to $N = 2.1 \times 10^{20}\,\mathrm{cm}^{-3}$ and $\Gamma = 3.2 \times 10^{14}\,\mathrm{Hz}$, which were verified by ellipsometry measurements. To precisely match the interference pattern in the spectra, the insulator thickness was set to $1130\,\mathrm{nm}$. The resulting simulated spectra are shown as dotted lines in the same graphs as the experimental spectra. The simulations were done in two parts: one simulation for the emissivity spectral range and one for the solar absorptance spectral range. This accommodated the limited range of material parameters, which were often obtained in two parts, one for the visible regime and one for the infrared. As described above, the visible range simulation shows spikes in absorption, which were not observed in the measured spectra. Another aspect that should be noted is the strong UV absorption shown in the simulated spectra. Since the developed measurement

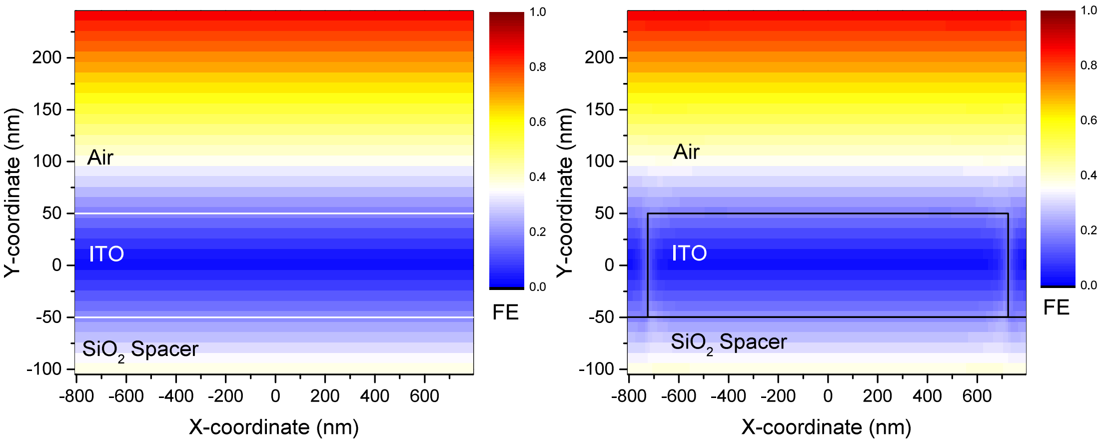

(a) 3.3 µm, planar ITO **(b)** 3.3 µm, patterned ITO

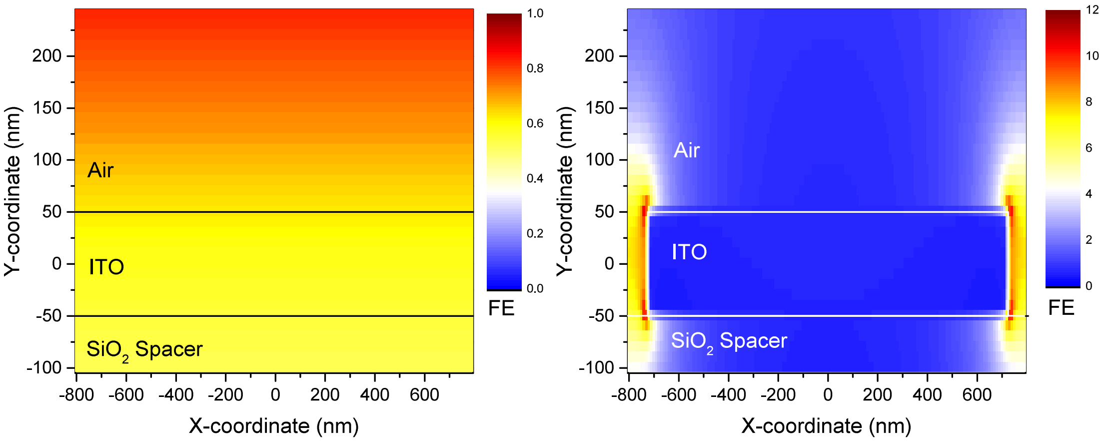

(c) 8.5 µm, planar ITO **(d)** 8.5 µm, patterned ITO

Figure 4.8: Near-field maps of the metareflector at (a, b) 3.3 µm and (c, d) 8.5 µm. The field enhancement (FE) describes the enhancement of the electric field normalised to the background. The left column shows the structure with a planar AZO film, the right column with a square of 1350 nm size.

setup does not support a spectral range extending into the UV region, a main contributor to α is not included in the experiments. A UV measurement on planar AZO confirmed good agreement of the simulated data, as expected since the material's Lorentz parameters come from ellipsometry measurements of the same AZO. Comparisons between simulated and experimental spectra show that total absorptance is increased by $0.04 - 0.05$ due to UV absorption. The limited FTIR spectral range on the other hand affects the emissivity values negligibly.

To evaluate the contribution of the patterning to the optical properties of the device, the electric near-fields were plotted for planar and patterned structures (figure 4.8). At 3.3 µm, the position

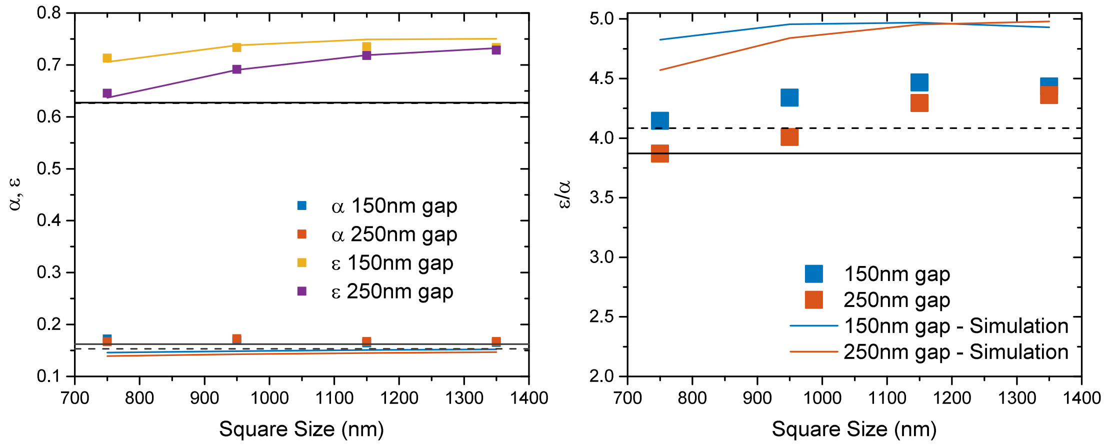

(a) **(b)**

Figure 4.9: (a) Absorptance and emissivity of the Experimental spectra (symbols) together with the simulated values (lines). The values for the planar structure are shown as black lines for experimental (dashed) and simulated (solid) results. (b) Figure of merit “Epsilon over Alpha” for the two different gap sizes using the same labelling as in (a).

of 0% absorption, both behave similar and show regions with maxima (FE $= 1$) and minima (FE $= 0$) of the standing wave. At $8.5\,\mu\mathrm{m}$, the device absorbs most of the incoming light, about 60% for the planar structure and approx. 80% for the patterned one with $1350\,\mathrm{nm}$ size and $250\,\mathrm{nm}$ gap. The difference in absorption corresponds to the different near-field distributions, where the patterned film shows an 6 times to 11 times higher near-field amplitude in the gap between the squares. The near-field enhancement is a characteristic property of plasmonic resonances, so that plasmonic resonances can be identified as the origin of the enhanced absorption.

We calculate α and ϵ from the measured and simulated spectra using Kirchhoff’s law of thermal radiation [163], which states that the measured IR absorbance will be equal to the structures emissivity. The values are shown in Fig. 4.9(a), where the simulated values were calculated for the same spectral ranges as the experimental data. The experimental values are shown by squares, while the simulated values are shown by lines. In the case of ϵ, the simulated and experimental values lie close together. For the simulated absorptance values, the same linear fit is used as in the previous section to compensate for the absorption spikes in the FDTD model. The experimental α values are higher than the simulated ones, mainly because the experimental setup with the integrating sphere does not capture all the light, especially not that diffracted at high angles. Thus the measured solar absorptance is higher than in reality, and the simulations represent the best case scenario. The graph also shows the values for the planar structures as horizontal lines for experimental (solid) and simulated (dashed) values. The experimental solar absorptance for planar AZO is lower than the simulated one, since the reflection between $1\,\mu\mathrm{m}$ to $2\,\mu\mathrm{m}$ is lower,

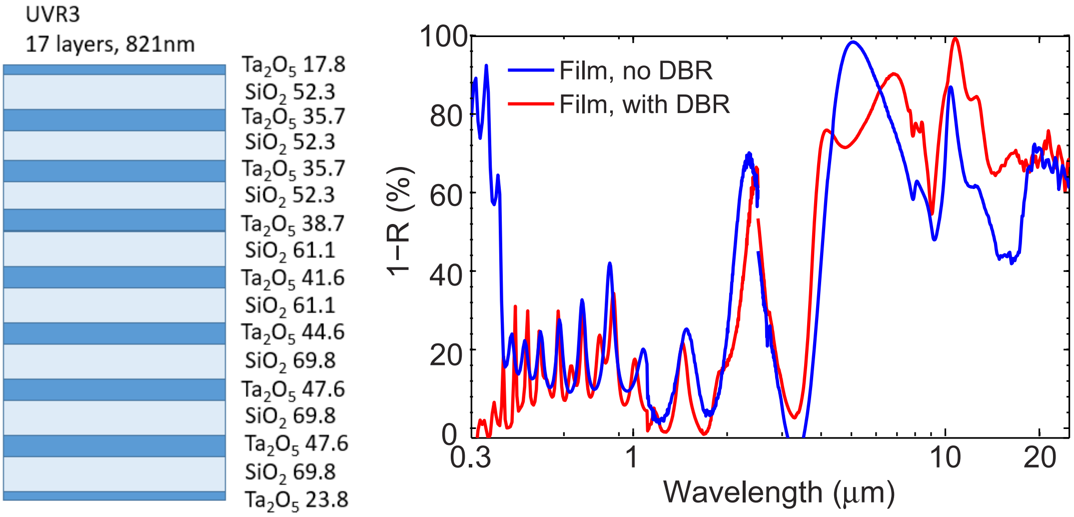

(a)

Figure 4.10: AZO-based metareflector with a distributed bragg reflector deposited on top. (a) Schematic representation, (b) experimental spectra of the device with a planar AZO film, with and without DBR.

see Fig. 4.7. The IR emissivity values lie on top of each other, indicating the high fit quality.

The figures of merit ϵ/α for the fabricated structure are shown in Fig. 4.9(b), using again square symbols for the experimental values, and solid lines for the simulated one. The horizontal black lines represent the values for a planar structure. The experimental data for the patterns shows values between 3.75 and 4.5, outperforming the planar film with all pattern sizes with $150\,\mathrm{nm}$ gaps, and with the two largest sizes with $250\,\mathrm{nm}$ gaps. The highest experimental value of $\epsilon/\alpha = 4.47$ is found for the $1150\,\mathrm{nm}$ squares with a gap of $150\,\mathrm{nm}$. The simulated figures of merit are, due to the lower absorptance, in all cases higher than the experimental values, showing the optimum case if all diffracted light in the visible range is captured by the measurement system. With $\epsilon/\alpha = 4.98$, the highest simulated value is found for a $1350\,\mathrm{nm}$ square size and $250\,\mathrm{nm}$ gap.

These values are obtained for the limited range of the experimental setups. As mentioned before, increasing the integration limits to the full defined range, α is raised by 0.04–0.05, thereby decreasing the figure of merit by approx. 20%. Therefore, the full-range values of the simulated structure result as $\alpha = 0.177$, $\epsilon = 0.710$ and $\epsilon/\alpha = 4.01$. A potential further improvement of the performance of the solar metareflector is given by changing the insulator thickness to $1500\,\mathrm{nm}$ to match the optimum case for the fabricated carrier concentration of $2.5 \times 10^{20}\,\mathrm{cm}^{-3}$. Taking the simulations for $N = 2 \times 10^{20}\,\mathrm{cm}^{-3}$ and $N = 3 \times 10^{20}\,\mathrm{cm}^{-3}$ of Fig. 4.4 as a reference, the emissivity could be increased by further $10\% - 14\%$.

Another way to improve the metareflector's performance is the use of a distributed Bragg reflector (DBR) to enhance the UV reflectance of the structure. Such a reflector coating, designed by Prof. Otto Muskens is shown in Fig. 4.10(a), consisting of a multilayer stack of SiO_2 and Ta_2O_5 with a total thickness of $821\,\mathrm{nm}$. The thickness of the two materials decreases from bottom to top, creating a broad reflection band due to constructive interference of back-reflected light in the UV spectral range. As shown in Fig. 4.10(b) for planar AZO, the structure effectively lowers α by reflecting UV radiation before it reaches the AZO layer. On the patterned AZO, the increased presence of insulators with a refractive index higher than that of air red-shifts the plasmonic resonances of the meta-surfaces. The achievable emissivity increases to $\epsilon = 0.793$, while the solar absorptance is reduced to $\alpha = 0.12$. The resulting figure of merit $\epsilon/\alpha = 6.7$ shows the strong performance increase enabled by the DBR.

Temperatures that could be achieved with the meta-surface can be calculated by entering the figure of merit into Eq. 4.3. This results in a temperature of $157\,\mathrm{K}$, which is close to the $153\,\mathrm{K}$ that are obtained by entering the values for quartz tiles.

4.5 VO_2-based meta-surface

VO_2 is a thermally switchable material that enables active thermal control [164]. In the case of low-temperature VO_2, the structure acts as a dielectric throughout the whole spectral range, while above a temperature threshold of 65°C the structure becomes plasmonic in the infrared. The samples containing planar VO_2 were fabricated by Consorzio CREO in Italy, and

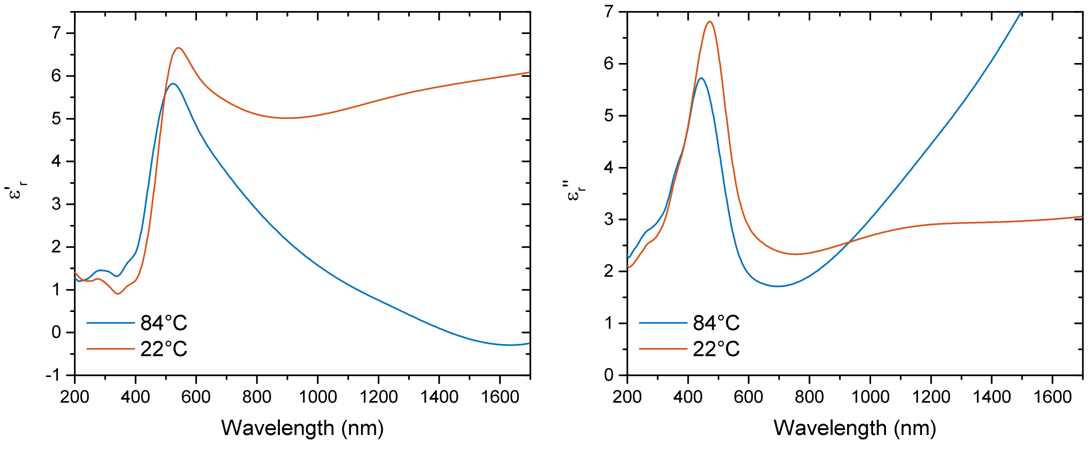

(a) **(b)**

Figure 4.11: Ellipsometry data of a VO_2 film at 22°C and 84°C. (a) Real part of the dielectric permittivity; (b) imaginary part.

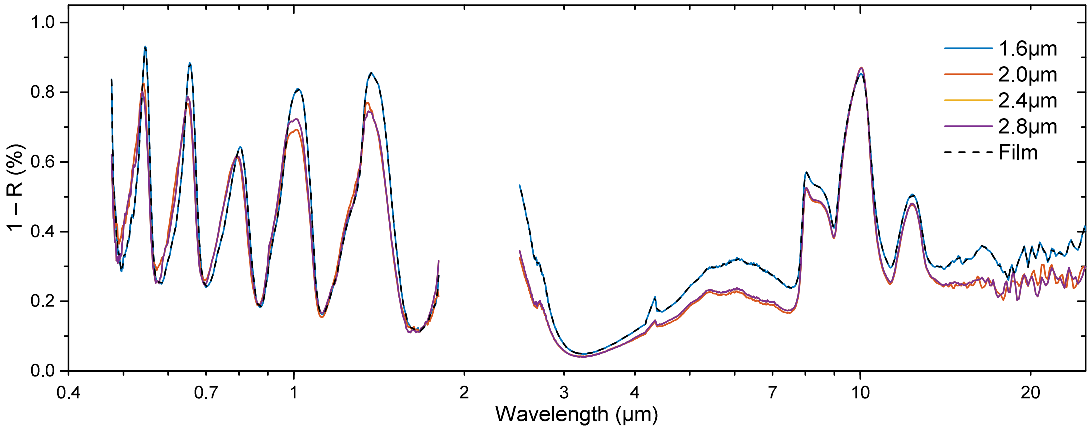

(a)

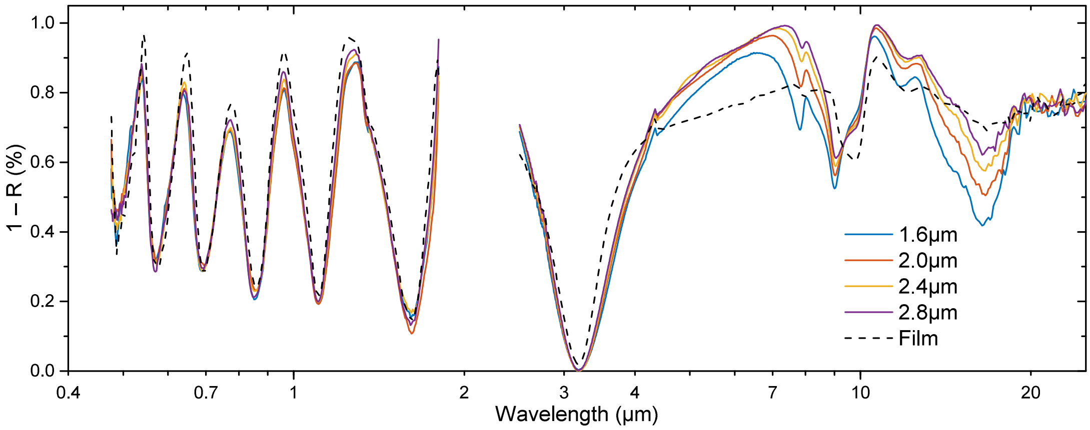

(b)

Figure 4.12: Spectra of the patterned VO_2 meta-surface with square sizes as indicated and gaps of $0.5\,\mu\mathrm{m}$. (a) at 25°C, (b) at 80°C. The unpatterned film is indicated by the black dashed line.

were subsequently patterned in Southampton using the same procedures as for the AZO-based meta-surface.

The real and imaginary part of the permittivity of VO_2 are given in Fig. 4.11 for two different temperatures. At room temperature, VO_2 acts as a dielectric with a single bandgap at around $450\,\mathrm{nm}$. Optical losses of the low-temperature VO_2 are higher than those of AZO and ITO, but lower than metals. When the VO_2 is thermally switched, the optical properties above $800\,\mathrm{nm}$ are drastically changed. An ENZ region is established at $1300\,\mathrm{nm}$, and a Drude-like increase of the optical losses with increasing wavelength becomes observable. The optical behaviour in the high-temperature state can be described as ‘metallic’, with the ENZ corresponding to a carrier concentration of $8 \times 10^{20}\,\mathrm{cm}^{-3}$.

The measured spectra in the visible and IR spectral range are given in Fig. 4.12 for low and high

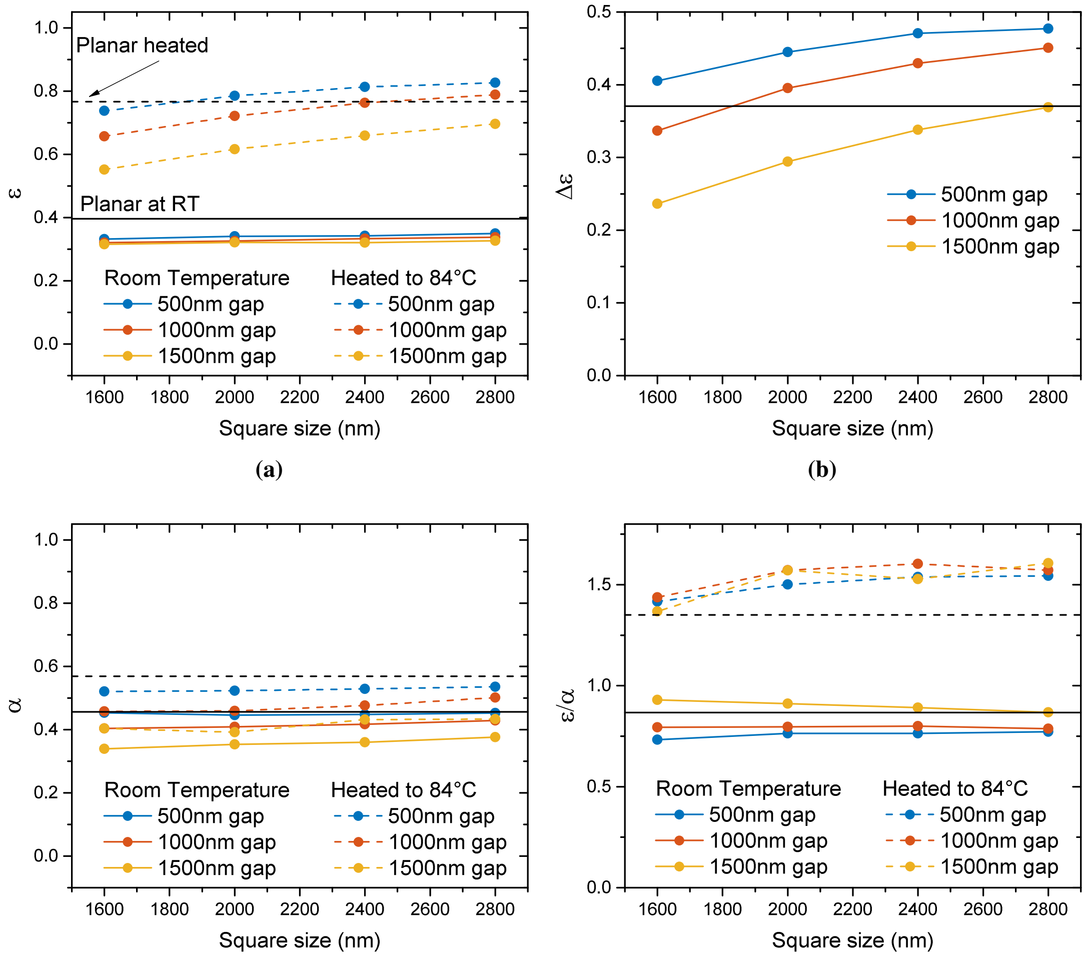

(a)

(b)

(c)

(d)

Figure 4.13: (a) Emissivity of the patterned and unpatterned VO$_2$ meta-surface for the two different temperatures, as a function of square size. (b) Solar absorptance for the fabricated meta-surfaces as a function of square size. (c) Emissivity tunability for the graphs in (a). (d) Figure of merit ϵ/α as a function of square size. In all graphs, the black horizontal lines denote the values for the unpatterned meta-reflector.

temperatures. In both cases, the short wavelength spectrum shows a high-amplitude interference pattern with increased absorption compared to AZO due to the higher optical losses. The IR part shows comparably low absorption at room temperature, with the SiO$_2$ phonon absorption bands at $10\,\mu\text{m}$ dominating the spectrum. At 85℃, the switched metallic behaviour of VO$_2$ allows a broad plasmonic resonance similar to that supported by AZO. The unpatterned film already shows this trend, while patterning of the film further increases IR absorption at resonance.

To characterise the switchability of the IR properties of the VO$_2$-based metareflector, the emissivity's tunability $\Delta\epsilon(\Delta T) = \epsilon(T_2) - \epsilon(T_1)$ is introduced as a new parameter. The temperatures were set as $\Delta T = 55\,\mathrm{K}$, with $T_1 = 25°\mathrm{C}$ and $T_2 = 80°\mathrm{C}$ to ensure full switching of the entire VO_2 film.

Figures 4.13(a, b) show the emissivity ϵ and the tunability $\Delta\epsilon$ of the patterned VO_2 meta-surfaces. At low temperature, the emissivity lies between 0.31 and 0.35, with a slight increase with higher pattern density (smaller spacing, larger squares). In the heated state, the patterns show good scaling of the absorption with increased pattern size, indicating a plasmonic resonance that is shifted towards longer wavelengths, as is also supported by Fig. 4.12(b). The VO_2 meta-surface, similar to the AZO metasurface, benefits from small interparticle gaps. The presentation of $\Delta\epsilon$ in Fig. 4.13(b) further points out the benefit of the proper pattern dimensions on the switchability of the plasmonic resonance. For a pattern gap of $0.5\,\mathrm{\mu m}$ and a square size of $2.8\,\mathrm{\mu m}$, $\epsilon = 0.81$ and $\Delta\epsilon = 0.47$. Comparing the IR absorption to the planar film, only the largest squares with the narrowest gaps are able to outperform it based on ϵ. For the emissivity tunability however, most of the patterns outperform the planar film.

Looking at the solar absorptance shown in Fig. 4.13(c), the values are in general higher than what was shown with the AZO meta-surface. This comes from the higher imaginary part of the VO_2 permittivity. The patterned meta-surfaces obtain mostly lower values compared to the planar reflector due to the reduced fill factor of the VO_2. Some overestimation of the solar absorptance due to light diffracted at high angles can be expected, as was the case for the AZO meta-surface. This explains why some of the values are above those of the planar film. Finally, the figure of merit ϵ/α is presented in Fig. 4.13(d). The values show more than 50% tunability by the smart meta-surface, showing the potential for future thermally switchable devices. Compared to the AZO meta-surface, the values are rather low, however one has to keep in mind that this is a proof-of-principle demonstration of the use of VO_2 without much optimisation in terms of VO_2 material properties, particularly its losses.

To summarise the findings of the VO_2-based metareflector, the device was able to demonstrate emissivity tunability based on the switchable optical properties of VO_2. In the dielectric state at room temperature, emissivity and solar absorptance are low, enabling a low-loss operation in situations where radiative cooling of a spacecraft is not necessary. If the temperature is increased above the thermal threshold to 80°C, emissivity is largely increased, competitive to the AZO metareflector presented earlier. The trade-off is an increase of the solar absorptance to more than three times the value observed with AZO. The decision to use either AZO or VO_2 for a meta-surface has therefore to be done based on which of the optical properties is more important for the application in question.

In this chapter, spectrally selective reflectors and absorbers based on the transparent conductive oxide AZO and the switchable plasmonic material VO_2 were demonstrated. The presented design with a periodic plasmonic pattern enhanced by a Salisbury screen has the advantages of being ultrathin, low-weight and individually customisable. High emissivity and low solar absorptance could be demonstrated with both materials, with an advantage in terms of traditional figures of merit for the AZO-based device. VO_2 on the other hand offers the unique ability to switch the IR emissivity based on the temperature of the surroundings, i.e. for the cooling of a spacecraft whose temperature needs to actively be stabilised. With expected further improvements of design parameters, deposition and patterning methods and material properties, a substitution of currently used quartz tiles can be expected in the near future.

5 Electro-plasmonic modulator using directly addressable nanoantennas

This chapter deals with the simulation of a gap-loaded nanoantenna structure for electro-plasmonic modulation. As will be seen in the later chapters containing the experimental work, the initial design that was fabricated suffered from several drawbacks, such as the small overlap of the modulated carrier distribution and the optical near-fields. In this chapter, the full electro-optical model that was developed to overcome those challenges is described. The design is optimised in two steps: the first using a device where the TiN back contact is removed and the antennas themselves serve as the electrode. This effectively removes coupling between the antennas and other metals in the device. After resonance pinning is confirmed as the last mechanism inhibiting device performance, an ITO gap-loaded antenna design is used, resulting in unprecedented modulation efficiency. A parameter analysis shows strengths and weaknesses of the new design and clears the path for the device fabrication in the future. Large parts of this chapter were published in the journal Optics Express [165]. The simulation work presented in this chapter was performed concomitantly to the fabrication and characterisation work that will be shown in the later chapters. Therefore the simulation results presented in this chapter show the highest electro-optical modulation values of this thesis.

5.1 Demonstration of the accuracy of the electro-optical model

To evaluate the accuracy of the combined model using Lumerical FDTD Solutions for the optical response and Lumerical DEVICE for the electrical charge modulation, it was benchmarked by comparison of simulated values to the experimental results for the structure by Park et al. [117]. The nanoscale nature of the two solvers uses significantly smaller mesh sizes than traditional photonics modelling. Instead, the modelling approach has to be regarded in comparison to semiconductor nanoelectronics, where nanometre thick carrier accumulation layers are simulated. This implies that the meshes have to provide sub-nanometre element sizes, which poses particular demands on the available memory and computational resources.

To obtain accurate results, the mesh in both solvers has to be fine enough to accurately sample the carrier distribution curves. During the work on the structure by Park et al., it was found that at

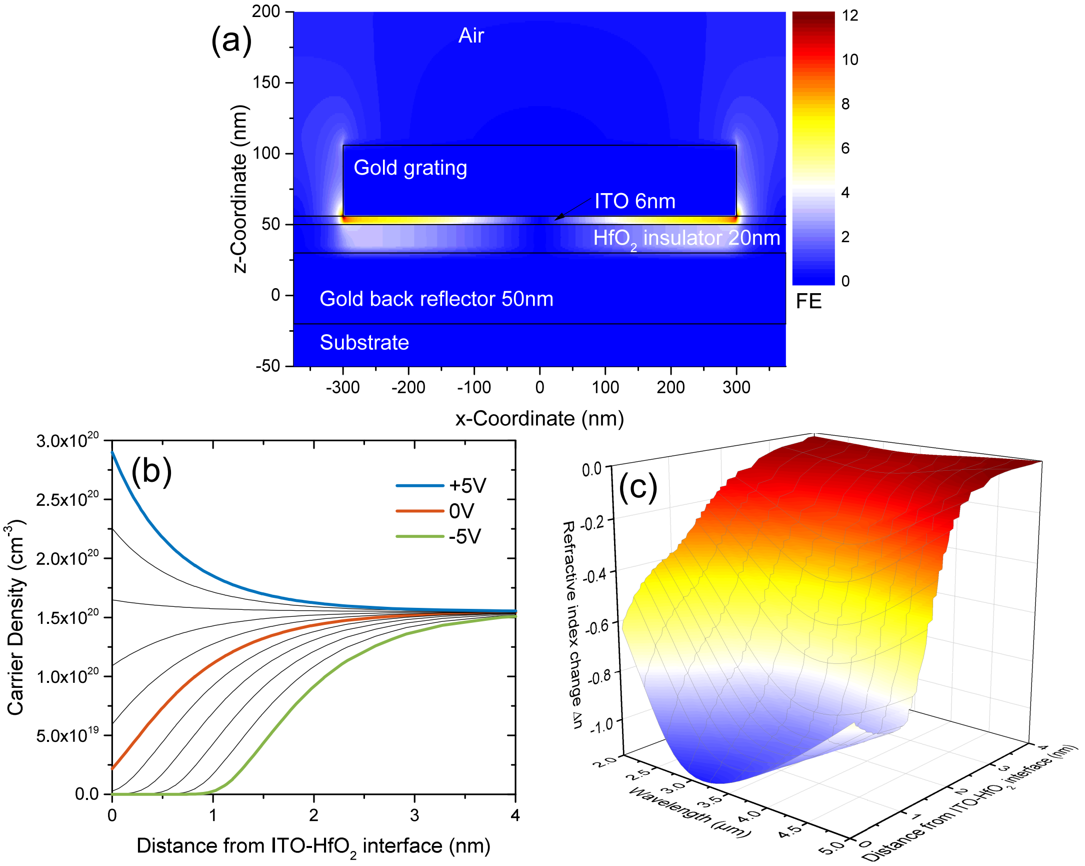

Figure 5.1: (a) Schematic, and near-field distribution at resonance, of the structure by Park et al. [117]. The gold grating consists of infinitely long wires with $600\,\mathrm{nm}$ width and $750\,\mathrm{nm}$ period. The field enhancement (FE) represents the normalised electric field distribution. (b) Simulated carrier distribution in a vertical line cut through the ITO using the software Lumerical DEVICE. (c) Induced refractive index change by changing the applied voltage from -5 V to $+5$ V as a function of wavelength and distance from the ITO-HfO_2 interface. Near the maximum refractive index change at $3\,\mu\mathrm{m}$, the refractive index nearly reaches zero close to the interface.

least 10 mesh elements per charge layer were needed. The structure is a reflective meta-absorber, which is shown in Fig. 5.1(a) together with its near-field distribution at resonance, and consists of a 2D grating stretched infinitely along the length of the stripes (y) and a periodic pattern in the direction of the polarisation of the incoming light (x). A gold back reflector is covered by $20\,\mathrm{nm}$ HfO_2 and $6\,\mathrm{nm}$ of ITO with a carrier concentration of $1.47 \times 10^{20}\,\mathrm{cm}^{-3}$. The gold grating on top consists of $600\,\mathrm{nm}$ wide stripes with $150\,\mathrm{nm}$ gaps. Since the vertical gap is smaller than the horizontal one, the calculated near-field concentrates below the grating stripes, overlapping well with the ITO.

Figure 5.1(b) shows the charge distribution of the structure under applied biases of 5 V to -5 V. Thin black lines show the carrier distribution at increments of 1 V. At 0 V, a depletion layer is formed as a result of the different Fermi levels of the ITO and the gold bottom contact. Upon the application of a positive bias, charges accumulate up to a carrier concentration of $3 \times 10^{20}\,\mathrm{cm}^{-3}$ in a sub-1 nm thick layer. The negative bias causes the depleted region to spread to a thickness of $1.5\,\mathrm{nm}$, as was also found by Park et al. [117].

To visualise the effect of the charge modulation, the charge difference between the depleted and accumulated case is converted into a refractive index change by applying the Drude model. The resulting graph is plotted in Fig. 5.1(c) as a function of wavelength and distance from the insulator-semiconductor interface. The refractive index of depleted ITO is near $\varepsilon_\infty = 2$ without any ENZ region, while the unmodulated carrier density of $1.6 \times 10^{20}\,\mathrm{cm}^{-3}$ has an ENZ region at $4.2\,\mu\mathrm{m}$, which is moved to $3\,\mu\mathrm{m}$ upon carrier accumulation. Coinciding with the ENZ, the region of the largest refractive index reduction is also at $3\,\mu\mathrm{m}$, as visible in the graph.

Figure 5.2 shows the the experimental and simulated reflectance of the sample. For the simulations, all material parameters were taken from reference [117], except for the ITO carrier concentration, which was slightly increased to $1.6 \times 10^{20}\,\mathrm{cm}^{-3}$ to centre the resonance wavelengths of the structure to the same spectral region. The spectra show excellent agreement between experiment and simulation, especially in the formation of constructive and destructive interferences at different voltages. The absolute reflectance change is 13 percentage points and the normalised modulation is $\Delta R/R_0 = (R(V_+) - R(V_-))/R(0) = 21.5\%$ at $4.0\,\mu\mathrm{m}$, while the experimental data shows 14 percentage points reflectance change and $\Delta R/R_0 = 25.7\%$ at $3.7\,\mu\mathrm{m}$, respectively. The most prominent difference is an offset of the simulated graphs by 0.1 on the y-axis, which can be attributed to the lack of surface roughness and other fabrication imperfections in the model. An effect of the chosen Drude model parameters on the reflectance offset was not found.

5.2 Uniformly ITO-coated plasmonic nanoantennas

In simulation studies, materials are assumed to be of the best quality that can reasonably be fabricated. For this chapter, this mainly affects the maximum applicable electric field before breakdown. For HfO_2, breakdown fields as high as $13\,\mathrm{MV\,cm}^{-1}$ have been reported [97], however only if the capacitance surface area remains as small as $10 \times 10\,\mathrm{nm}^2$. A more conservative value is $10\,\mathrm{MV\,cm}^{-1} = 1\,\mathrm{V\,nm}^{-1}$, which will be used for the maximum applied voltages. The other materials are modelled as described in section 3.3.

As was done throughout this thesis, the device parameter that is investigated in this chapter is the antenna extinction cross-section. Often in literature, simulations and experimental measurements present reflection or transmission data, since these are the directly measurable properties. However this leads to unreliable data if the change in reflection or transmission is normalised to an intensity dip near 0%. The results from Park et al. [117] and Huang et al. [119] both give normalised

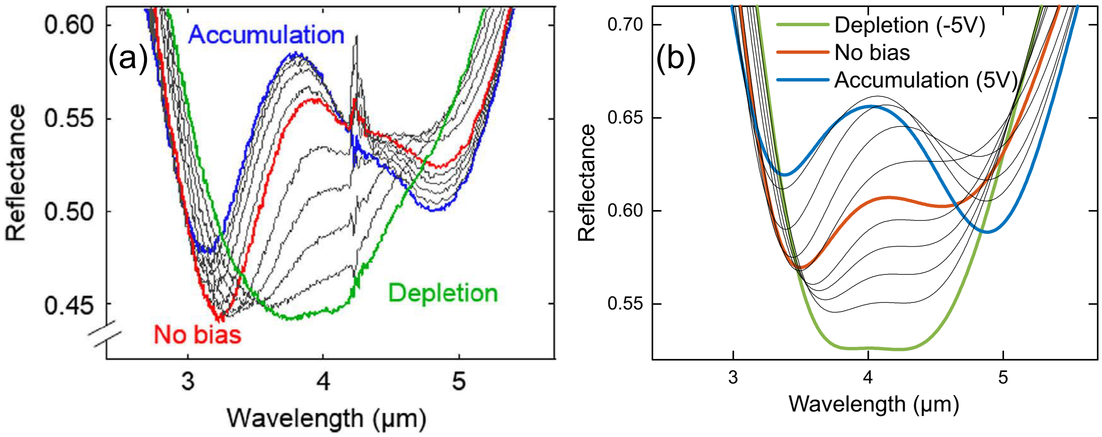

Figure 5.2: Comparison between the measured and simulated reflectance of a reflective meta-absorber. (a) Measured optical reflectance using an FTIR, taken from [117] (under the Creative Commons License 4.0 `http://creativecommons.org/licenses/by/4.0/`). (b) Simulated reflectance from combined Lumerical DEVICE and FDTD simulations, showing good agreement with the experimental spectra.

reflectivity changes at an intensity dip. Especially when comparing the experimental spectra of these two articles side by side, it becomes obvious that their modulation amplitude is quite different, even though they both report around $\Delta R/R \approx 30\%$.

Therefore, the extinction cross-section of the antenna will be the metric of choice. The extinction cross-section at resonance shows a maximum for plasmonic structures, which ensures that no minima are used as reference. This allows a consistent interpretation of the modulation strength of the structure. The spatial modulation spectroscopy setup can measure single-antenna extinction spectra and therefore confirm the theory with experimental results. Naturally, reflection and transmission will still be the measured values in a large-scale experiment, yet modulation of these values depends on the exact device and experiment design and has to be regarded independently of the modulation of the antenna properties. Therefore, a comparison of the modulation strength of the extinction cross-section, the transmission and the reflection will be given for the final structure.

Electrical modulation of plasmonic nanoantenna dimers [16], contrary to that of stacked reflectors, poses peculiar challenges and opportunities. One opportunity is the small surface area of the antennas which makes them promising electrodes for low-capacitance structures. The direct electrical connection of nanoantenna arms has been characterised and utilised before and showed conservation of the antenna's optical properties [21, 22]. Figure 5.3 gives simulations from the author showing the low impact of the connector wires, which were modelled with a width and height of $30\,\mathrm{nm}$ and several $100\,\mathrm{nm}$ length. The main resonance experiences a slight blue shift, which is matching the results published in figure 3 (a) of reference [21]. By using

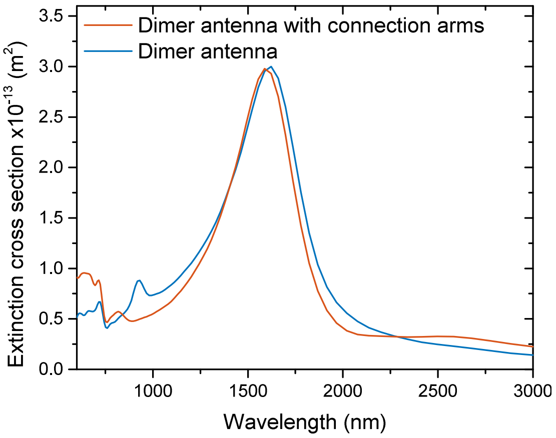

Figure 5.3: The influence of $30\,\mathrm{nm}$ wires connecting each antenna arm onto a gold dimer antenna with $250 \times 100 \times 30\,\mathrm{nm}^3$ arms and a $30\,\mathrm{nm}$ gap.

the nanoantenna as an electrode, the unit cell area of the capacitance is below $1\,\mathrm{\mu m}^2$, enabling ultrafast electrical modulation due to the low RC constant. This is an advantage for applications as a matrix, where one dimer antenna corresponds to one digital element, such as pixels or transistors.

One challenge on the other hand is the fact that dimer antennas are usually free standing and thus provide strong field enhancement only in the antenna gap. That makes it essential for the carrier modulation to occur in that region to get a large overlap between the electrical and optical response. Accumulating and depleting carriers homogeneously over a large area of TCO underneath the antennas is not sufficient. The following simulations use a wire mesh electrode consisting of gold dimer antennas, separated by a small gap, with each arm being electrically wired to a contact pad, see the top view in Fig. 5.4(a). The wires and antenna arms are modelled with a $30 \times 30\,\mathrm{nm}^2$ cross-section, which lies well within the capabilities of e-beam lithography. Since the wires are orthogonal to the antenna arms, they do not couple to longitudinally polarised light, so that their optical response can easily be separated from the antennas. This implies that the device can only be used for one polarisation, as is the case in most modulator designs.

A simple three layer structure was investigated first. The schematic of the structure, a uniformly coated nanoantenna dimer, is shown in Fig. 5.4(b). The gold nanoantennas represent the bottom electrode, which is then coated by a $2\,\mathrm{nm}$ thick HfO_2 insulator and a $100\,\mathrm{nm}$ thick sheet of ITO. Compared to the device in the previous chapter, the TiN electrode is replaced which allows the use of a very thin insulator. The carrier depletion at $0\,\mathrm{V}$ depends on the insulator thickness, resulting in a noticeable depletion layer in Fig. 5.4(c). At the application of a bias of $+2\,\mathrm{V}$, the initial depletion is compensated up to almost the flat band case. A negative bias further increases the thickness of the depleted layer. The uniformly ITO-coated antenna device therefore operates

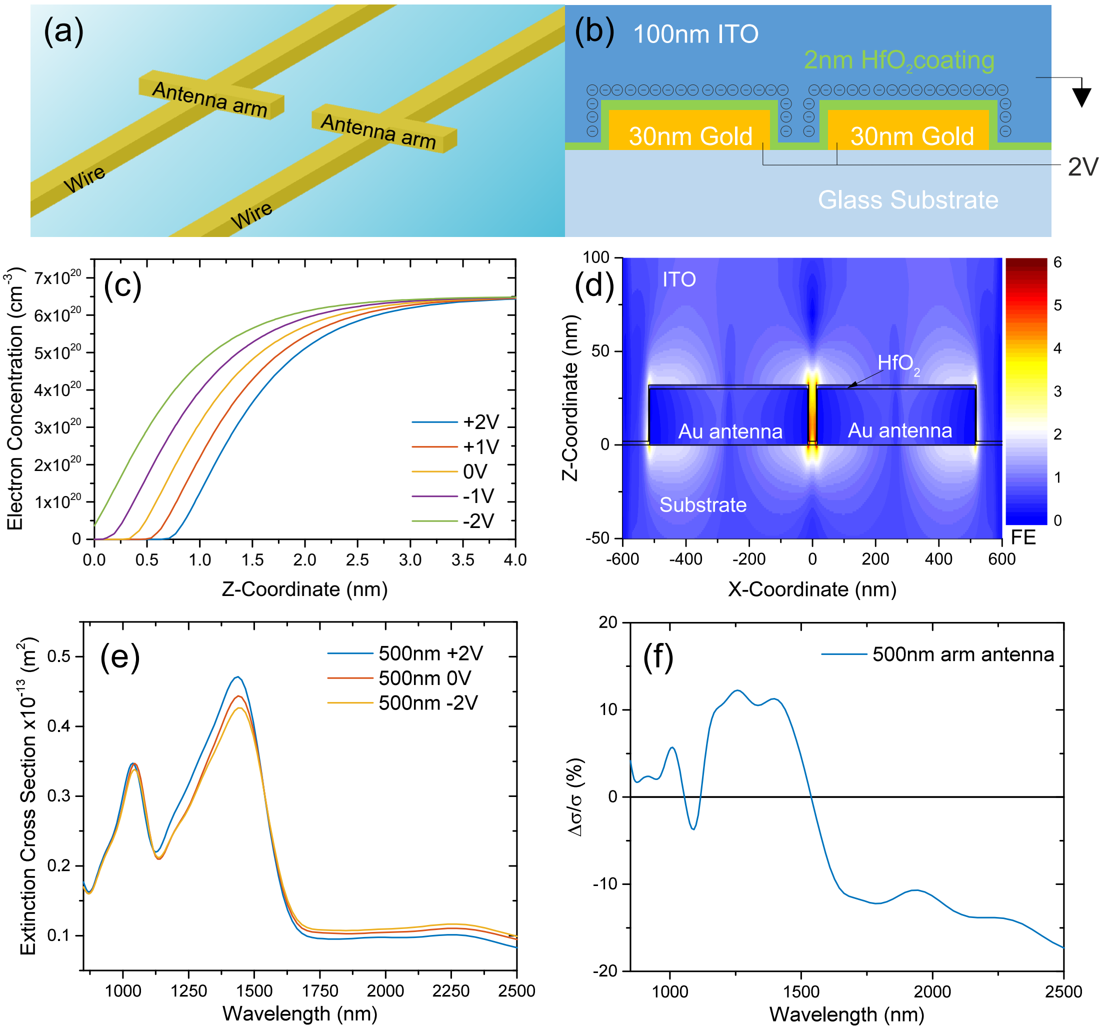

Figure 5.4: (a) Schematic representation of a gold dimer antenna whose arms are electrically addressable by thin wires. (b) Cross-sectional view of the gold dimer antenna, coated by $2\,\mathrm{nm}$ of HfO_2 and $100\,\mathrm{nm}$ ITO. (c) Charge distribution inside the ITO upon the application biases from -2 V to 2 V. (d) Optical near-field distribution of the proposed structure. The field enhancement (FE) is strongest in the gap and at the antenna ends. (e) Simulated extinction spectra of the depicted design, using an antenna with $500\,\mathrm{nm}$ arm length. (f) Normalised modulation from -2 V to 2 V by the same structure.

solely in depletion, which can be an advantage due to the larger thickness of depletion compared to accumulation layers. The carrier sheet wraps around the antenna, giving two modulation layers inside the antenna gap, which provide the necessary overlap with the optical near-field shown in Fig. 5.4(d). The ITO carrier density was set to $6.5 \times 10^{20}\,\mathrm{cm}^{-3}$, bringing the ITO ENZ region close to $1550\,\mathrm{nm}$, the telecom wavelength where the modulation is desired. The antenna arms are $500\,\mathrm{nm}$ long and with a $30\,\mathrm{nm}$ gap to achieve a resonance very close to the ENZ.

The results for the uniformly coated nanoantennas are shown in Fig. 5.4(e). The $l_{\text{eff}} = \lambda/2$ resonance of the antenna is located at approx. $1550\,\text{nm}$, showing some amplitude modulation but no resonance shift. At the short wavelength side, a second resonance ($l_{\text{eff}} = 3\lambda/2$) at $1100\,\text{nm}$ does not show significant modulation. For wavelengths above $1750\,\text{nm}$ $\varepsilon'_m < 0$ prevents antenna resonances due to the lack of a metal-dielectric interface. For long wavelengths, the ITO itself acts like a metal sheet. In this spectral range, the baseline cross-section of $1 \times 10^{14}\,\text{m}^2$ corresponds to the surface area of the antenna and the wires within one simulated unit cell. The spectrum of the normalised change in the extinction cross-section is given in Fig. 5.4(f).

The structure was designed with a focus on the effect of depletion, which shifts the refractive index towards higher values in the vicinity of the antenna. From this perspective, a large red-shift of the antenna resonance is expected. However, as can be seen in the spectra, the resonance shift is countered by the resonance pinning from unmodulated bulk ITO, which remains close to ENZ. Even though the ITO a few nanometres from the antenna acts as a dielectric, the near-field of the antenna extends over $100\,\text{nm}$ into the ITO, so that on average the ENZ ITO dominates. Sensitivity to small changes of the antenna length or its surrounding medium are lost. Therefore, the structure shows only an amplitude modulation of $\Delta\sigma/\sigma_0 = 11\%$ at $1550\,\text{nm}$. While this is a good value at this short wavelength, large scale resonance wavelength shifting cannot be realised with this simplistic structure.

5.3 ITO gap-loaded plasmonic nanoantennas

Circumventing the problem of resonance pinning is a tough challenge, since two (metal or TCO) electrodes need to be provided. A solution is realised by the gap-loaded antenna structure depicted in Fig. 5.5(a). In this structure, instead of coating the whole structure with ITO, it is only deposited inside the antenna gap. An ITO circle is deposited into the gap and acts as a switchable antenna load. The circle is $30\,\text{nm}$ in diameter and $50\,\text{nm}$ high. The carrier density was again chosen to be $6.5 \times 10^{20}\,\text{cm}^{-3}$, to bring the ENZ region of the ITO close to the $1550\,\text{nm}$ telecom wavelength. The antenna arms become the top electrode to provide electrical contact. As bottom electrode, a low-doped transparent conductive oxide is used, with a carrier density low enough to ensure the material does not couple to the antennas. $100\,\text{nm}$ of the undoped ZnO which was presented in section 3.1.2, with a carrier concentration of $6.9 \times 10^{19}\,\text{cm}^{-3}$ (Fig. 3.2), could be used. The transparent electrode allows modulation of both the transmittivity and reflectivity of the sample, opening a completely new field of applications. A potential disadvantage of the ITO back contact is that it will also accumulate and deplete charges which will be addressed in the last section of this chapter.

Because the gap-loaded antenna design was created with a focus on accumulation mode, a large HfO_2 thickness of $30\,\text{nm}$ ensures that depletion of the ITO gap-loading at $0\,\text{V}$ is low,

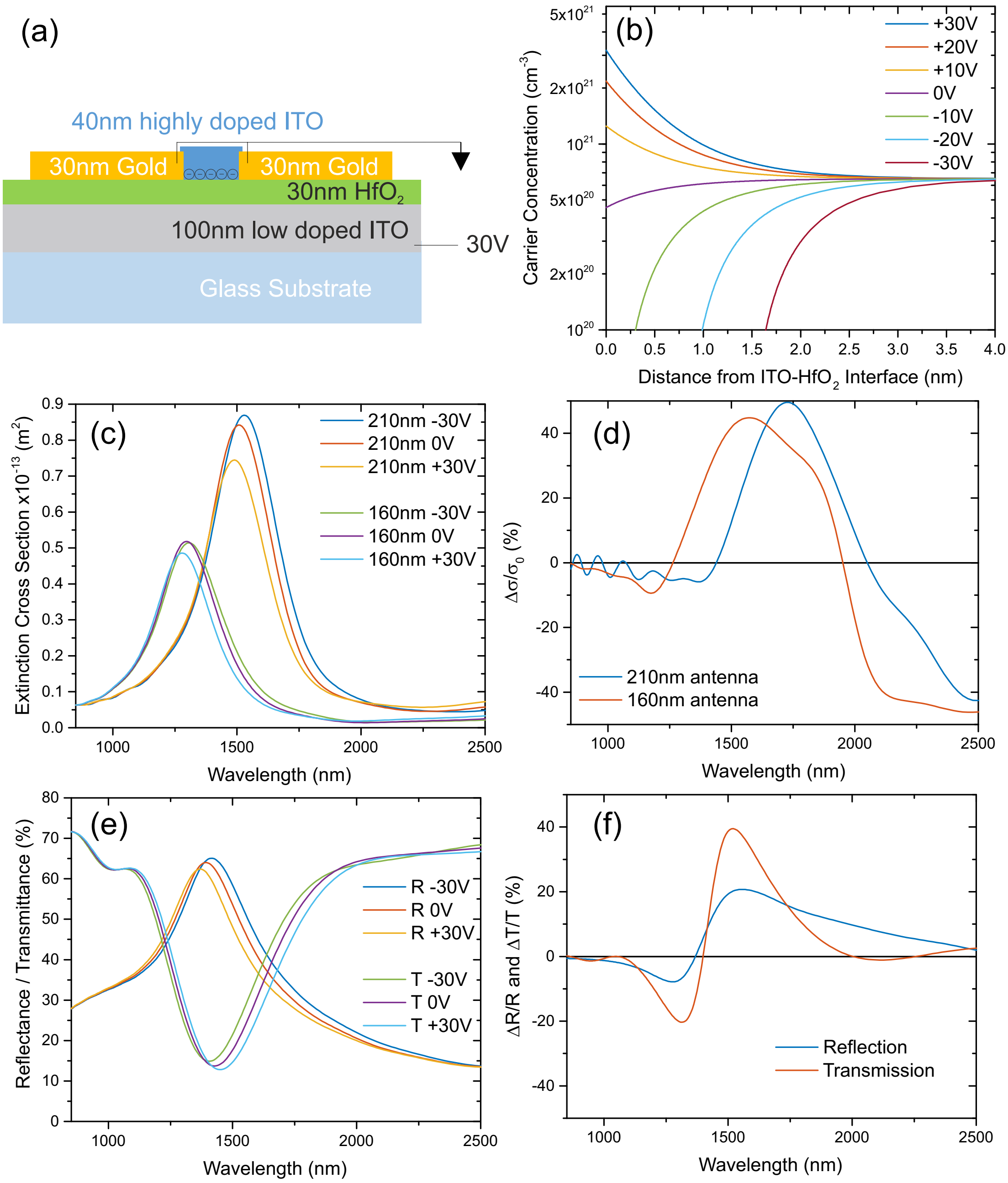

Figure 5.5: (a) Cross-sectional view of the gap-loaded structure, where the substrate is coated by a back contact consisting of $100\,\mathrm{nm}$ low-doped ITO and $30\,\mathrm{nm}$ of HfO$_2$. The gold dimer antenna serves as top electrode and has a gap-load of $50\,\mathrm{nm}$ highly doped ITO. (b) Carrier distribution inside the ITO gap-load as a function of voltage. The accumulated carriers reach $3 \times 10^{21}\,\mathrm{cm}^{-3}$. (c) Simulated extinction spectra of the depicted design, for antennas with $210\,\mathrm{nm}$ and $160\,\mathrm{nm}$ arm lengths. (d) Relative modulation spectra of the same antennas. (e) Transmission and reflection spectra of a periodic structure with $250\,\mathrm{nm}$ transverse spacing between the antenna arms. (f) Normalised modulation spectra of $\pm 30\,\mathrm{V}$ for the spectra in (e).

see Fig. 5.5(b). This eases the formation of an accumulation layer upon the application of a positive bias. An advantage of a thicker insulating layer is the lower probability of breakdown due to pinholes compared to the $2\,\mathrm{nm}$ thick insulator in the uniformly ITO-coated structure. To maintain an electric field of $1\,\mathrm{V\,nm^{-1}}$, the applied bias is set to $\pm30\,\mathrm{V}$. The positive bias accumulates charges at the bottom of the gap-load. The ITO in that region becomes optically metallic ($\varepsilon_m < 0$) and reduces the capacitive coupling between the two antenna arms, resulting in a blue-shift of the antenna resonance. The abundance of ITO outside the gap prevents the resonance pinning observed in the previous structure. The antenna shape and its metal-dielectric interface are preserved.

The extinction cross-section of this structure with and without the application of a bias are given in Fig. 5.5(c) for two different antenna arm lengths. Upon depletion, the resonance shows a small red-shift, which comes from the increased refractive index in the gap-load. Upon accumulation, a blue-shift occurs, accompanied by a decrease of the extinction cross-section. The combination of amplitude reduction and wavelength shift causes all the modulation to be located on the long wavelength side, instead of occurring symmetrically. This is similar to the results of the gap-loaded structures shown at the beginning of chapter 6.1 [25, 40].

Fig. 5.5(d) shows the normalised modulation spectra. For an antenna arm length of $210\,\mathrm{nm}$, the $0\,\mathrm{V}$ resonance peak is located at $1550\,\mathrm{nm}$, which is shifted by $38\,\mathrm{nm}$ in wavelength (2.4%) and $\Delta\sigma/\sigma_0 = 15\%$ in amplitude by the applied voltage. Yet, an even higher modulation is achieved on the side of the resonance. By reducing the antenna arm length to $160\,\mathrm{nm}$, this is utilised to achieve a normalised modulation of $\Delta\sigma/\sigma_0 = 44.8\%$ at $1550\,\mathrm{nm}$. Additionally, the full-width at half-maximum of $526\,\mathrm{nm}$ gives a particularly large region for the electro-optical working point. Comparing the values with those used in chapter 1, in terms of resonance shift the structure performs better than the one by Huang et al. which was 1.6% at $1550\,\mathrm{nm}$ [119]. In terms of normalised modulation strength, the structures from Huang et al. and Park et al. are both outperformed (30% and 35% respectively). These promising results show the potential of our method to enable strong modulation of free standing dimer nanoantennas at telecom wavelengths.

To ease comparison with devices from other authors, the simulated reflection and transmission of a periodic antenna array are given in Fig. 5.5(e). In longitudinal direction, the array consists of an infinite row of $160\,\mathrm{nm}$ long antenna arms, separated by $10\,\mathrm{nm}$ gaps which are loaded with ITO as before. In transverse direction, the antenna rows have a $250\,\mathrm{nm}$ spacing. It was found that spacings above $200\,\mathrm{nm}$ are sufficient to prevent resonance broadening through coupling. This results in the structure experiencing coupling in longitudinal, but not in transverse direction, leading to a medium impact of broadening to the optical modulation strength. The normalised spectra for this structure are shown in Fig. 5.5(f). As expected, the spectra show larger relative modulation when normalised to a dip (here for transmission), even though the modulation amplitude of both methods is the same. Up to $\Delta T/T_0 = 40\%$ are reached in transmission, which can be further tuned by reducing longitudinal coupling, or ensuring that the transmission dip comes closer to 0%. This is however only to be seen as an example for potential experimental results and the implications of the choice of measurement method.

The method depicted here, i.e. the reduction of capacitive coupling via an electrically switched $\varepsilon < 0$ layer of TCO, can be readily adapted to other structures, such as metasurfaces and plasmonic waveguides, opening up a new way of electrical control over optical properties. Naturally, the method can also be applied to other wavelength ranges by adjusting the antenna arm length and the initial ITO carrier concentration. The only limit in terms of the shortest wavelength where modulation is still achievable is the maximum carrier concentration obtainable by current deposition methods. For demonstrated carrier concentrations of e.g. $1 \times 10^{21}\,\mathrm{cm}^{-3}$ [64], the ENZ wavelength of ITO is at $1300\,\mathrm{nm}$.

Due to the nature of the gap-loaded approach, the antenna preserves many of its characteristic properties, such as the sub-$1\,\mu\mathrm{m}$ footprint and the high field confinement at the antenna ends. The latter are largely unaffected by the gap-load, so that they can be used for plasmonic sensing and near-field enhanced nonlinear effects.

5.4 Parameter analysis

In preparation for the fabrication of the structure, the influence of fabrication imperfections was quantified by simulating sweeps over several design parameters. Figure 5.6 shows the results of four design parameters, which are swept across several values. Figure 5.6(a) shows the electro-optical modulation performance for carrier concentrations from $2 \times 10^{20}\,\mathrm{cm}^{-3}$ to $1 \times 10^{21}\,\mathrm{cm}^{-3}$ inside the gap. As a general trend, higher gap-loadings result in a blue-shift of the unbiased resonance (not shown). In the normalised modulation spectra, two peaks A (marked in black) and B (marked in red) can be observed, where A is close to the resonance and B further toward the infrared. With increasing carrier concentration, peak A increases until reaching a maximum for a carrier concentration of $6.5 \times 10^{20}\,\mathrm{cm}^{-3}$. Further increase of the carrier concentration decreases the modulation peak again and narrows the modulation bandwidth. Peak B has opposite proportionality, with an increasing carrier concentration leading to a decrease in peak height. One must keep in mind that the spectra shown here are the result of a subtraction of spectra at two different voltages, which are then normalised to the $0\,\mathrm{V}$-case [cp. Fig. 5.5(b)]. Due to the fact that B is far off the resonance, is is the result of a minimal fluctuation in one of the spectra and has no direct usability.

Peak A shows the importance of the overlap of the antenna resonance and the transition wavelength of the gap-load. For $10^{21}\,\mathrm{cm}^{-3}$, the wavelength at wich the strongest modulation occurs is at $\lambda_t = 1300\,\mathrm{nm}$, however the antenna resonance stays close to the $1550\,\mathrm{nm}$ it was designed for. By adjusting the arm length, the overlap could be improved again, so that the

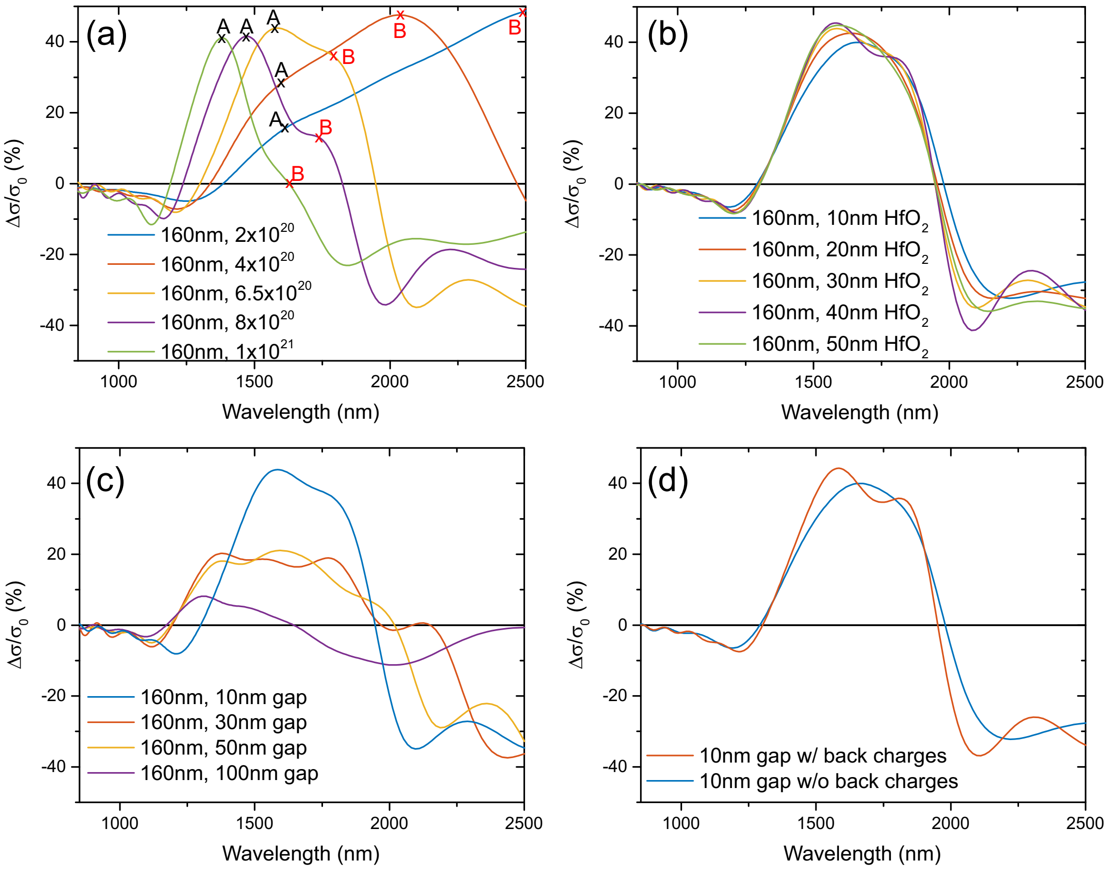

Figure 5.6: (a) Normalised modulation spectra as a function of the carrier concentration (in cm^{-3}) of the gap-load. The spectra show two main peaks. (b) Influence of the HfO_2 thickness on the peak modulation. (c) Influence of the antenna gap width on the modulation strength. (d) The modulation spectra with and without the inclusion of charge modulation in the low-doped ITO back contact.

conclusion for the carrier concentration sweep is that antenna size and carrier concentration have to match for optimum performance. For the antenna arm length of $160\,\mathrm{nm}$, a carrier concentration of $6.5 \times 10^{20}\,\mathrm{cm}^{-3}$ or higher is necessary to obtain modulation values above 40% near resonance at $1550\,\mathrm{nm}$.

Figure 5.6(b) shows a sweep over the HfO_2 insulator thickness. The thickness ranges from $10\,\mathrm{nm}$ to $50\,\mathrm{nm}$, while the electric field is kept constant at $1\ \mathrm{V}\,\mathrm{nm}^{-1}$ to analyse in which condition the carrier accumulation works most effectively. From $30\,\mathrm{nm}$ to $50\,\mathrm{nm}$ the modulation is equally high around 44% and reduced for lower values of the insulator thickness. The modulation strength reduces to 42% at $1637\,\mathrm{nm}$ for $20\,\mathrm{nm}$ and 40% at $1664\,\mathrm{nm}$ for $10\,\mathrm{nm}$. Since the switching voltage scales linearly with HfO_2 thickness, this shows that effective resonance modulation is also possible at lower voltages.

A critical parameter of our design is the gap width of the antenna arms. The modulation spectra

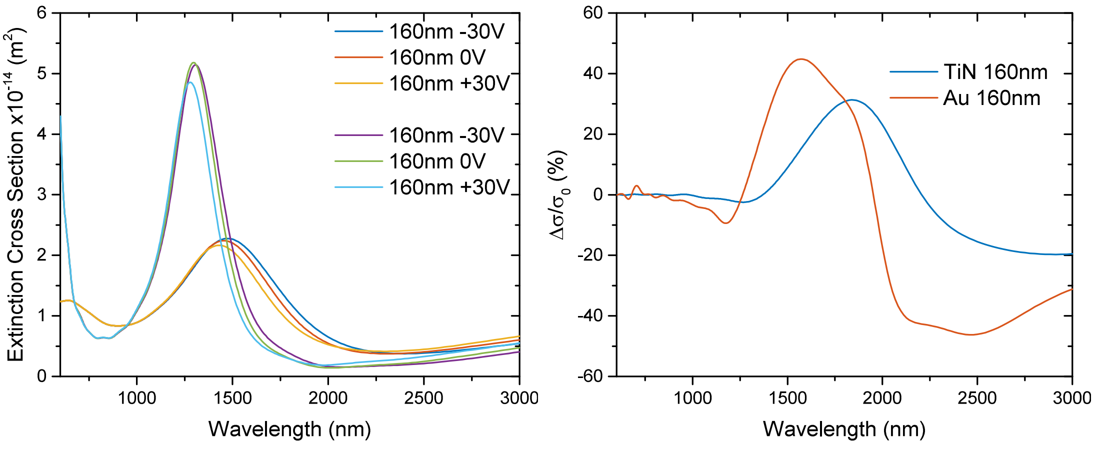

(a) **(b)**

Figure 5.7: TiN dimer nanoantennas for the modulator in the previous chapter. (a) Extinction cross-section spectra under bias; (b) normalised modulation compared to the gold-based modulator

of gap widths from $10\,\mathrm{nm}$ to $100\,\mathrm{nm}$ are shown in Fig. 5.6(c). A gap width of $10\,\mathrm{nm}$ shows by far the highest modulation, due to the high near-field confinement inside the gap. Larger gaps up to $50\,\mathrm{nm}$ still give strong modulation, however with reduced values of $\Delta\sigma/\sigma_0 = 20\%$. Gaps of $100\,\mathrm{nm}$ or higher should be avoided due to the reduced sensitivity of the antenna to gap-loading. Finally, the modulation spectra with and without taking charges at the bottom contact into account are compared in Fig. 5.6(d). For negative bias, the low-carrier ITO experiences charging up to the order of $1 \times 10^{21}\,\mathrm{cm}^{-3}$, counteracting the depleted gap-load. However due to the difference in near-field enhancement between the gap and the area below the antenna, the charges cause only a small perturbation of the modulation peak.

Figure 5.7 shows a comparison between the developed electro-plasmonic modulator and one with TiN nanoantennas instead of gold. The spectra in Fig. 5.7(a) have a lower amplitude and are broader than in the case for gold nanoantennas, but the resonance wavelength shifts by $49\,\mathrm{nm}$ between $10\,\mathrm{V}$ and $-10\,\mathrm{V}$. This is larger than the $38\,\mathrm{nm}$ which were achieved for gold, thus confirming the prediction from analytical theory that TiN nanoantennas are more sensitive to the surrounding medium. As can be seen from Fig. 5.7(b) however, in terms of the normalised extinction cross-section modulation, the TiN nanoantennas cannot outperform the device based on gold. For this metric, the broad resonances counter the advantages of TiN. This is connected to the material parameters of TiN, which were taken from experimental values of sputtered TiN films, and potential improvement of the resonance amplitude could be gained with TiN that has lower optical losses than obtained by the current deposition process. Until then, a TiN electro-plasmonic modulator does not offer an immediate benefit.

5.5 Conclusions of the simulation work

The simulations presented in this chapter show outstanding performance of electro-plasmonic modulation in terms of changes in the extinction cross-section of the nanoantennas. A modulation of near 45% was realised at the telecom wavelength of $1550\,\mathrm{nm}$. Contrary to designs from the literature, this was not realised at a minimum of the signal, where relative modulation intrinsically becomes high, but near resonance. This stresses the functionality of the chosen modulation mechanism, which is the carrier accumulation inside an ITO disk in the gap of a gold nanoantenna. This carrier accumulation partly short-circuits the antenna arms and thus blue-shifts the antenna resonance.

Experimental work on the modulator with directly addressable, gap-loaded antennas could not be brought to fruition within the scope of this work. However, with the accurate modelling of the electrical and optical properties of the device, with realistic material data that was proven to fit in countless previous experiments, it is likely that this design will show similar performance in reality. In the next chapter, the fabrication and optical characterisation of some fundamental antenna structures will be shown experimentally.

6 Fabrication and characterisation of novel antenna structures

This chapter describes the experimental work regarding novel antenna structures. The first part deals with the placement of an ITO disk into the gap of a dimer nanoantenna and the second part with the fabrication of nanoantennas out of TiN. These proof-of-principle experiments did not include electrical modulation of the fabricated structures, which is a separate part that will be the content of the subsequent chapter.

6.1 Gap-loaded ITO hybrid nanostructures

As mentioned in the literature review and demonstrated in the simulation results in chapters 1.1 and 5, the interaction of light and matter inside the gap of an antenna enables a variety of novel phenomena. For example, an advantage for electro-optical modulation of loading the gap of a dimer antenna, instead of covering it completely, lies in the fact that the antenna resonance is not quenched by the surrounding medium, if its $\varepsilon_r' < 0$. In the particular work described in this chapter, the aim was to demonstrate the placement of the ITO disk into the gap of the dimer antenna. The placement can be shown by observing an ITO-induced blue-shift of the antenna resonance, which occurs if the resonance wavelength of the antenna and the carrier concentration of the ITO are in a region where the refractive index of ITO is below 1. For this, a high ITO carrier concentration is needed. With the first of the two ITO evaporation recipes presented in chapter 3.1.2, achievable values as characterised by Hall measurements were on the order of $1 \times 10^{21}\,\mathrm{cm}^{-3}$, with results in an ENZ region in the near-IR range. Also of interest for gap-loaded antennas is the enhancement of nonlinear effects due to the confined near-field, which can for example be measured with pump-probe spectroscopy [40]. Therefore, the sample was also intended to be used for ultrafast characterisation of the gap-load via pump-probe experiments in the future, although this was not part of this thesis.

6.1.1 The effect of a high-carrier gap-load on an antenna resonance

Figure 6.1(a) shows the simulated extinction cross-section of a gap-loaded gold dimer antenna with an arm length of $250\,\mathrm{nm}$, $100\,\mathrm{nm}$ width, $30\,\mathrm{nm}$ thickness and a gap of $50\,\mathrm{nm}$ on a glass

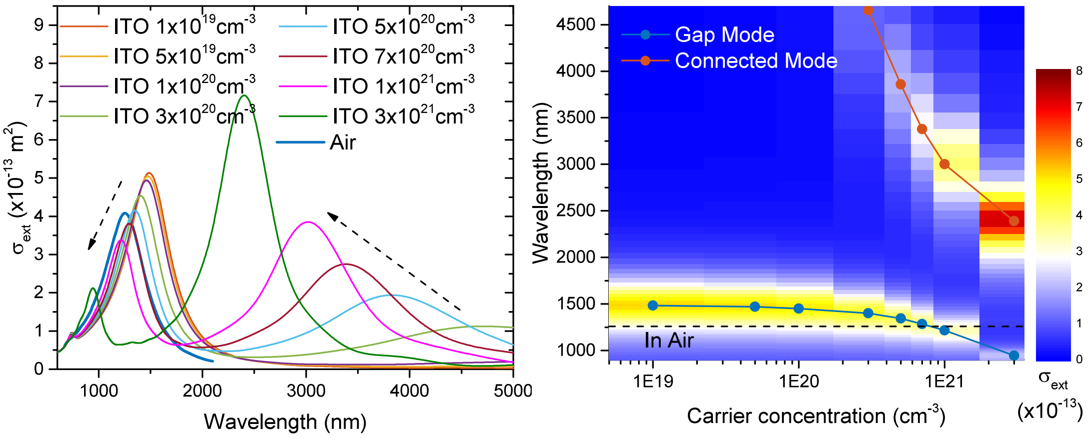

(a) **(b)**

Figure 6.1: Simulated extinction cross-section of a gap-loaded gold dimer antenna with an arm length of $250\,\mathrm{nm}$, $100\,\mathrm{nm}$ width, $30\,\mathrm{nm}$ thickness and a gap of $50\,\mathrm{nm}$. Lumerical was used with an ITO Drude model with carrier concentrations from $1 \times 10^{19}\,\mathrm{cm}^{-3}$ to $3 \times 10^{21}\,\mathrm{cm}^{-3}$. (a) The individual spectra, including the bare antenna; (b) peak lines of the spectra of (a). 'Gap mode' describes the normal antenna mode, 'connected mode' the longer wavelength mode created by short-circuiting the gap.

substrate. Several ITO carrier concentrations from $1 \times 10^{19}\,\mathrm{cm}^{-3}$ to $3 \times 10^{21}\,\mathrm{cm}^{-3}$ are shown, together with the bare antenna resonance. The simulations were done using Lumerical with the built-in material parameters for gold and glass, and for ITO a Drude model based on the parameters presented in chapter 2. The same spectra are shown as a contour map in Fig. 6.1(b) for better visualisation.

The refractive index of the low-carrier concentration ITO is close to 2, making the resonance to red-shift by more than $200\,\mathrm{nm}$ compared to the case in air. Increasing the ITO carrier concentration lowers the refractive index in the gap until the resonance wavelength matches that of the bare antenna at around $7 \times 10^{20}\,\mathrm{cm}^{-3}$ to $1 \times 10^{21}\,\mathrm{cm}^{-3}$. Further increase of the carrier concentration leads to a blue-shift. However, at such a high carrier concentration, the typical antenna resonance is no longer dominating the spectrum. Instead, a new peak starts appearing at $3 \times 10^{20}\,\mathrm{cm}^{-3}$, which shifts strongly with increasing carrier concentration and exhibits a three times higher amplitude at the highest carrier concentration. This new resonance is equivalent to the mode for an antenna with with one arm of twice the size, i.e. where the arms of the dimer antenna are connected through the gap. The high conductivity of the ITO results in a decreased capacitive and increased conductive behaviour of the gap, resulting in a charge transfer plasmon with twice the resonance wavelength. If the gap was short-circuited with the same material as the antenna, only the doubled wavelength resonance would be observable. However, due to the material in the gap being different from gold, both modes are observed. From an electronic circuit point-of-view, there is an impedance mismatch between the gold and ITO preventing perfect conductive coupling.

The peak lines shown in Fig. 6.1(b), where ‘gap mode’ describes the normal antenna mode and ‘connected mode’ the charge-transfer plasmon created by short-circuiting the gap, exhibit an anti-crossing behaviour. Both peaks blue-shift with increasing carrier concentration, the connected mode much stronger than the gap mode. It takes high carrier concentrations above $7 \times 10^{20}\,\mathrm{cm}^{-3}$to obtain any blue-shift compared to air. This shows how challenging the aim of this work is, and a potential outcome might be the mere observation of the connected mode. However, the blue-shift of longer antennas can be expected to be stronger, since the strength of the blue-shift depends on the resonance position of the bare antenna. The peak lines can be readily compared to the graphs in reference [40], especially figure 3(f), which shows a similar behaviour.

6.1.2 Fabrication and measurement methods

The nanostructures were fabricated in two e-beam lithography patterning steps. During these steps, the author received strong support from Dr. Yudong Wang for the e-beam design and fabrication process. First the gold antennas were deposited on top of a Schott Borofloat 33 glass substrate using a bi-layer lift-off process. The width, thickness and gap size of the antennas were kept constant at $100\,\mathrm{nm}$, $30\,\mathrm{nm}$ and $50\,\mathrm{nm}$ respectively, while the length scaled from $50\,\mathrm{nm}$ to $800\,\mathrm{nm}$. The second step, using the same bi-layer resist, consisted of writing nanodiscs with a diameter of $100\,\mathrm{nm}$, which were deposited using e-beam evaporation of ITO at $1.2\,\mathrm{Å\,s^{-1}}$ and under an oxygen pressure of $2 \times 10^{-4}\,\mathrm{mbar}$. The ITO was then annealed at 200 °Cfor $1\,\mathrm{h}$. This corresponds to the first recipe described in section 3.1.2.

The positioning of an ITO disc inside an antenna gap was not straightforward, because the automatic height alignment of the e-beam system is inaccurate on transparent and patterned samples. Due to that reason, as shown in Fig. 6.2(a), the ITO discs where not placed inside the gap of the dimer, but up to $160\,\mathrm{nm}$ outside of it. The displacement depends on the distance of the written pattern to the centre of the field of view of the e-beam system, which is $1\,\mathrm{mm}^2$ large. Figure 6.2(c) shows the schematic of how the pattern displacement ΔL relates to the height error ΔH of the measurement system. ΔH can be extracted from the e-beam system by measuring over a reference surface, so that, with a known e-beam deflection angle (system parameter), ΔL can be calculated. To overcome the displacement, chromium squares were deposited in the corners of the sample to provide a well-reflecting reference surface for the height alignment. The ITO placement was then sufficiently accurate. The images after correction are provided in Fig. 6.2(b). This correction method was presented in a talk at the conference *IEEE nano 2015* [166].

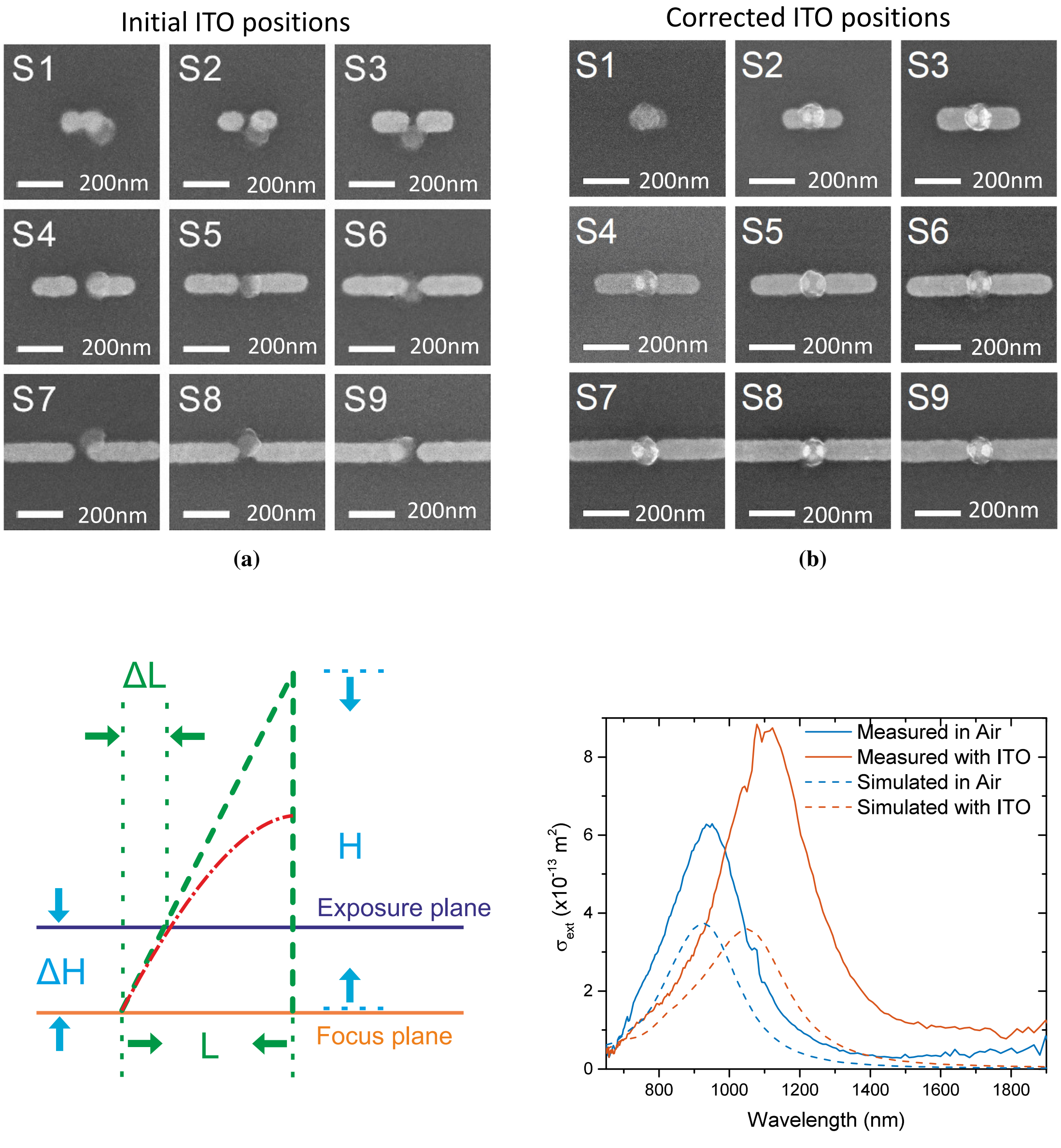

(a) **(b)**

(c) **(d)**

Figure 6.2: (a, b) Before and after SEM images of the height error correction, courtesy of Yudong Wang. (c) Schematic detailing how an incorrect height measurement creates an alignment error. The red dashed-dotted line shows the actual electron path, the green lines the virtual beam path. (d) Example spectra for a $150\,\mathrm{nm}$ arm antenna, with and without ITO gap-loading.

6.1.3 Single antenna sample

The single antenna sample was made to enable the characterisation of the hybrid nanostructures in the spatial modulation setup, where single nanoantennas can be measured individually. Two example extinction cross-section spectra of a $150\,\mathrm{nm}$ arm antenna with and without ITO gap-loading are shown in Fig. 6.2(d). A red-shift of the main resonance is observable if ITO is present. Simulated spectra for rectangular antennas using COMSOL are shown as well. For carrier concentration of $1 \times 10^{19}\,\mathrm{cm}^{-3}$, the simulation gives a similar resonance shift as the experimental ITO. The extinction cross-section is lower in the simulation than calculated from measurement, which can be due to the ITO contributing to the measured value, which was excluded in the simulation. Figure 6.3 gives the measured spectra for air as a function of antenna arm length in a contour plot, with the resonance peaks of all measurements and simulations overlaid. The chosen carrier concentration gives a good match over the range of measured arm lengths. The simulated peak lines follow a near linear increase of the resonance wavelength. The deviation of the measured peaks from the straight line is likely to arise from fabrication variations of shape or size of the antenna arms. The simulations were done with the nominal antenna dimensions. A blue-shift could not be observed even for the largest antenna arm length due to the low ITO carrier concentration. It is significantly lower than what was expected for the chosen recipe, so that subsequently Hall measurements were done regularly to monitor the deposition process.

6.1.4 Antenna array sample

Design description

A new sample was fabricated with a design that allows measurements in the extended infrared spectrum up to $5\,\mathrm{\mu m}$ wavelength. Individual dimer antennas with arm lengths from $50\,\mathrm{nm}$ to $450\,\mathrm{nm}$ cover the spectral range that can be measured by our spatial modulation setup. Additionally, $120 \times 120\,\mathrm{\mu m}^2$ antenna arrays with arm lengths of up to $800\,\mathrm{nm}$ can be characterised in the FTIR via ensemble measurements. As was shown in a previous publication [52], a distance of at least $600\,\mathrm{nm}$ is necessary so that the antennas do not couple. Because of this, the interparticle spacing inside the array was chosen as $1\,\mathrm{\mu m}$.

Two sets of antennas were written, one with an exposure dose of $500\,\mathrm{\mu C\,cm^{-2}}$ and one with $550\,\mathrm{\mu C\,cm^{-2}}$. This was to compensate small exposure variations, which mostly affect the gap size. If the dose is too high, the gap will be overgrown. If the dose is too small, the gap will be too large. For the whole sample, the antennas with $50\,\mathrm{nm}$ arm length did not come out, which means that they were removed during lift off and the corresponding areas are bare.

To characterise the ITO evaporation process, a test run was done beforehand. Hall measurements

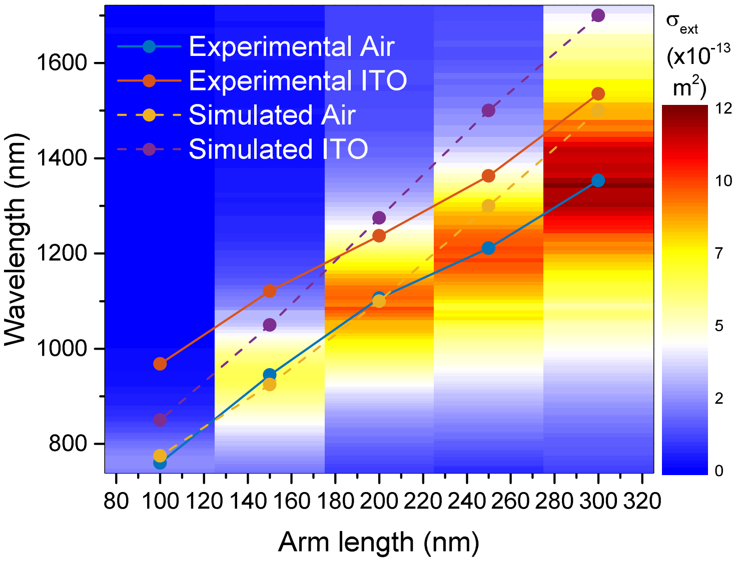

Figure 6.3: Resonance peak lines of the ITO gap-loaded gold dimer antennas, having a width of $100\,\mathrm{nm}$ and a thickness of $30\,\mathrm{nm}$. The spectra were measured using spatial modulation spectroscopy. Simulations were done using COMSOL. The carrier concentration of the ITO in the simulations was set to $N = 1 \times 10^{19}\,\mathrm{cm}^{-3}$.

gave a carrier density of $3.35 \times 10^{21}\,\mathrm{cm}^{-3}$ in the $100\,\mathrm{nm}$ thick film, which is an exceedingly high value. This carrier concentration corresponds to a transition wavelength of $\lambda_t = 752\,\mathrm{nm}$, which can however not be strictly assumed for the final sample since the properties of an ITO film vary from those of ITO nanostructures.

Optical characterisation

FTIR transmission spectra for the antenna set written with $500\,\mu\mathrm{C\,cm}^{-2}$, with polarisation along the longitudinal axis, are plotted in Fig. 6.4(a) and 6.4(b). The observable spectral range is limited by the FTIR laser at $1250\,\mathrm{nm}$ and by absorption from the glass substrate at $5000\,\mathrm{nm}$. The spectra show strong transmission dips, which correspond to extinction peaks of the antenna resonances. The extinction strength increases with increasing antenna arm length. For antennas with arms up to $450\,\mathrm{nm}$, several dips can be seen, while for greater arm lengths the spectra show only one dip per antenna. The antennas with $100\,\mathrm{nm}$ and $200\,\mathrm{nm}$ arm length do not show any transmission dips.

The two modes supported by the antennas with short arm lengths vary in amplitude. The $450\,\mathrm{nm}$ has a stronger resonance in mode 1 than in mode 2, while for the other arm lengths the amplitude is more even. Mode 1 corresponds to about twice the wavelength of mode 2. These trends and the spectra themselves are remarkably similar for the bare and gap-loaded antennas.

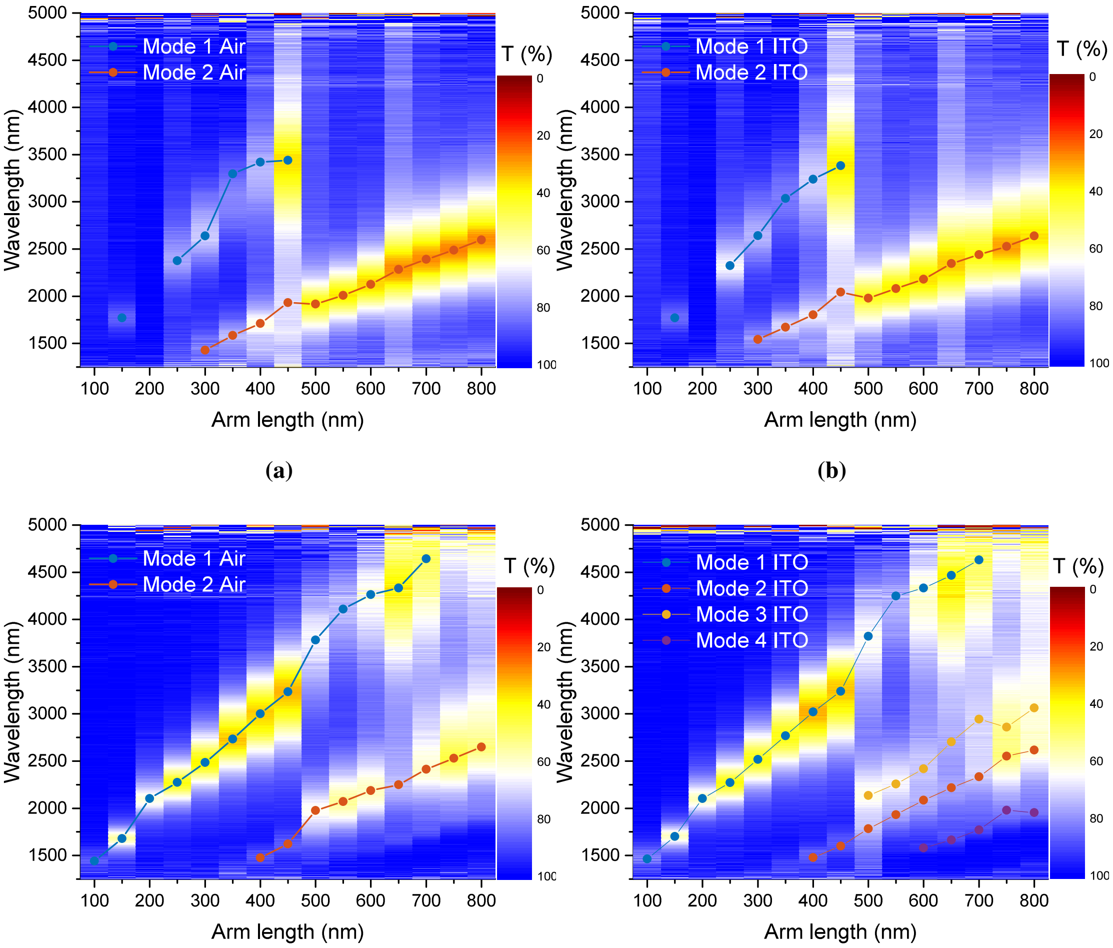

(a) **(b)**

(c) **(d)**

Figure 6.4: Transmission FTIR spectra from gold dimer antennas as function of arm length for an exposure dose of $500\,\mu\mathrm{C\,cm^{-2}}$ (a, b) and $550\,\mu\mathrm{C\,cm^{-2}}$ (c, d). (a, c) are bare antennas spectra and (b, d) with ITO in the gap. The antennas exhibit pronounced resonances which show as transmission dips, corresponding to extinction cross-section peaks.

Figure 6.4(c, d) show the FTIR transmission spectra for the $550\,\mu\mathrm{C\,cm^{-2}}$ set. The spectra are similar in strength to those of Fig. 6.4, however the number of transmission dips is changed. Here, the antennas with arm lengths up to $350\,\mathrm{nm}$ show single dips, while the antennas with longer arms show at least two transmission dips. That means the antennas that were fabricated with a higher dose show an inverse mode distribution compared to those antennas fabricated with the lower dose. A possible explanation for the lack of a second mode for short antenna arms could be the limited spectral range, i.e. the resonances of the second mode could occur at too short of a wavelength to observe them. Judging from the spectral locations, mode 2 in air corresponds to

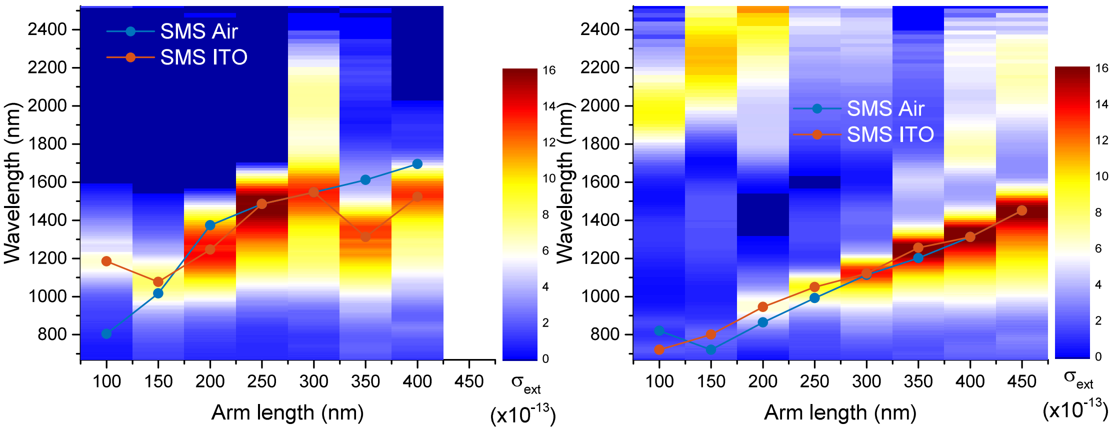

(a) **(b)**

Figure 6.5: Spatial modulation spectra of gold dimer antennas with ITO in the gap: (a) for the antenna set exposed with $500\,\mu\mathrm{C\,cm^{-2}}$; (b) for the set exposed with $550\,\mu\mathrm{C\,cm^{-2}}$. Dark blue colour signifies small negative $\Delta R/R$-values. The resonance peak positions of bare antennas are shown as well.

mode 3 with ITO, because both are at half the wavelength of their respective mode 1. The ITO gap-loaded antennas show two more resonances than the bare antennas, where mode 2 is a factor of 1.7 from mode 1 and mode 4 a factor of 3 from mode 1.

To obtain spectra for shorter wavelengths, spatial modulation spectroscopy (SMS) was performed. The spectral window of the setup spans from $680\,\mathrm{nm}$ to $2300\,\mathrm{nm}$ and is thus complementary to the FTIR measurements. The spectra of the gap-loaded antennas are plotted in Fig. 6.5 for the $500\,\mu\mathrm{C\,cm^{-2}}$ set Fig. 6.5(a) and the $550\,\mu\mathrm{C\,cm^{-2}}$ set Fig. 6.5(b). The measurements were performed on single antennas, which in the case of the $500\,\mu\mathrm{C\,cm^{-2}}$ set had been preselected based on SEM imaging to ensure that the antennas were intact, i.e. both arms are present and separated by a gap. This was the case in most of the antennas, and so the SEM analysis was not done again for the $550\,\mu\mathrm{C\,cm^{-2}}$ set. Since the measured spectra were very similar between the bare and gap-loaded version of the respective antenna sets, only the spectra of the ITO gap-loaded antennas are shown. However the peak lines for air are added into the same graph, so that a direct comparison is enabled.

The spectra of the $500\,\mu\mathrm{C\,cm^{-2}}$ set show mostly single resonances, with some spectral ranges showing negative extinction cross-sections coloured in dark blue. The measurement quality is not optimal, which was attributed to imperfections of the beam alignment. The observed resonance peaks are scaling with antenna arm length and coincide roughly between the bare and the gap-loaded case. The observed peaks line up with mode 2 of the FTIR spectra, in Fig. 6.4(b).

The $550\,\mu\mathrm{C\,cm^{-2}}$ antennas show clear resonances for all antennas that scale almost perfectly linear and agree well between the spectra in air and those with ITO. The signal-to-noise ratio is better than for the other antenna set, a trend which was also observed in the FTIR spectra. The spectra show a very good measurement quality with negligible spectral ranges below 0. The peak lines agree well with mode 2 Air and mode 3 ITO of the FTIR spectra, in Fig. 6.4(d). Some traces of mode 1 (both) and mode 2 ITO can also be seen in the plotted spectra. The general agreement between FTIR measurements and SMS, with respect to the spectral location of the resonance, is very good for all samples.

Of fused and unfused antenna arms

Scanning electron microscopy images of the array antennas, are shown in Fig. 6.6. As mentioned before, the $50\,\mathrm{nm}$ arm antennas were removed during lift-off. From the $100\,\mathrm{nm}$ antennas, some individual antenna arms did not come out either, leaving monomers only. These problems arise if the exposure dose is too low and not all of the e-beam resist is removed in the written area, so that the deposited gold is removed together with the residual resist during lift-off. The other antenna sizes are all present and have two antenna arms. The shape of the antennas is not perfectly rectangular, as the edges have rounded ends. This shape distortion is caused by the isotropic wet development, which softens hard contours. The deposited ITO discs are all present and well centred, showing that the height error correction, as described in section 6.1.2, worked well. A displacement of the ITO discs by about $20\,\mathrm{nm}$ to one side (left in the image) can be seen, but the entire gap is still covered.

A key property of the fabricated antennas is the gap size, which determines the coupling of the antenna arms and influences the sensitivity of the antenna to the ITO gap-loading. The smaller the gap, the higher the field enhancement inside, and the more sensitive the antenna becomes to the gap-load. The SEM images show small gaps in-between the antenna arms, with some variation in the exact size. Some of the antenna arms seem to be fused, showing that the dose in this case was too high. Conducting connections between the antenna arms can short-circuit the gap and thus quench the field enhancement inside.

The variation of the antenna gaps are given in more detail in Fig. 6.7. With increasing pattern density, the gap is known to overgrow due to increasing electron scattering. For this reason, the nominal gap in the e-beam layout was increased incrementally with increasing arm length, from $70\,\mathrm{nm}$ to $90\,\mathrm{nm}$. The actual gap size of the $500\,\mathrm{\mu C\,cm^{-2}}$ antennas was extracted from the SEM images and is displayed as the mean value and the standard deviation, calculated over four antennas, for each arm length. Comparing these results to the peak lines in Fig. 6.4, a correlation can be found between the long wavelength FTIR mode and a measured mean gap size of under $40\,\mathrm{nm}$. For these arm lengths, some of the antenna arms are fused, so that a resonance is found corresponding to a monomer antenna with twice the arm length. As is known from experiments

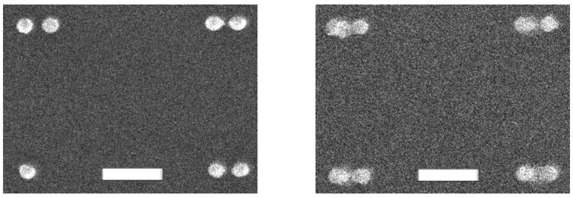

(a) 100nm in air **(b)** 100nm with ITO

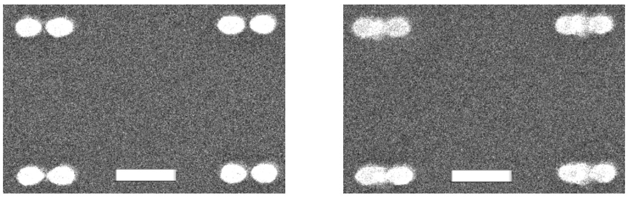

(c) 150nm in air **(d)** 150nm with ITO

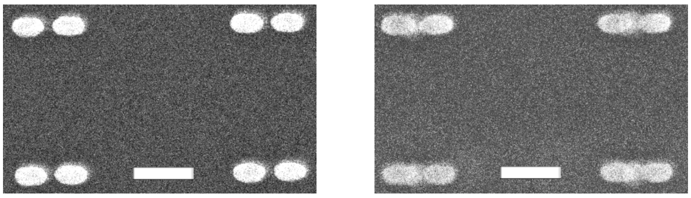

(e) 200nm in air **(f)** 200nm with ITO

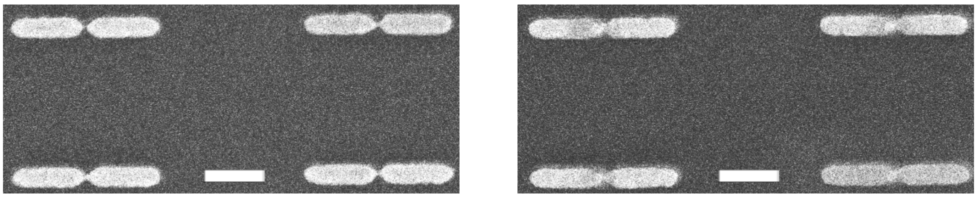

(g) 450nm in air **(h)** 450nm with ITO

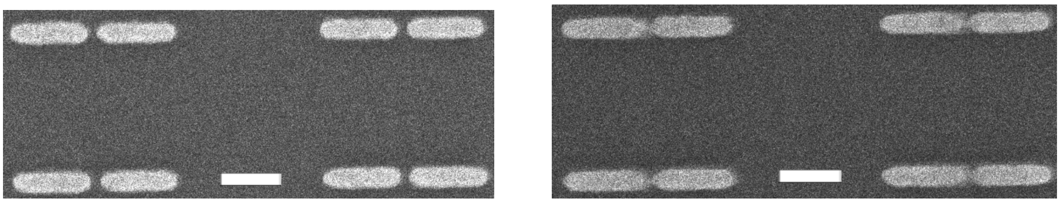

(i) 500nm in air **(j)** 500nm with ITO

Figure 6.6: SEM images of the antenna arrays with and without ITO gap-loading, for various antenna arm lengths. Length of scale bar is $400\,\mathrm{nm}$. Exposure dose was $500\,\mu\mathrm{C\,cm^{-2}}$.

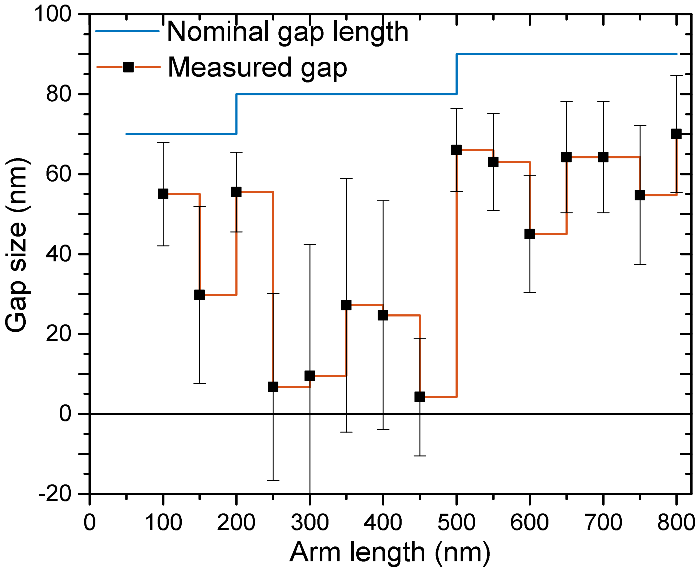

Figure 6.7: Nominal and measured gap of the $500\,\mu\mathrm{C\,cm^{-2}}$ antenna array structures. The measured gap is given as mean and standard deviation for four antennas.

with helium ion milling [25], a bridge short-circuiting the antenna gap with widths as small as $5\,\mathrm{nm}$ can shift the plasmonic resonance significantly. The ratio of fused and unfused antennas varies between the different arm lengths, as can be seen from the changing standard deviation. This explains the varying amplitudes of the different modes in the FTIR spectra.

An antenna of a certain size experiences a so-called fundamental mode, which is connected to the antenna arm length L by $\lambda_{\text{res}}/2 = n_1 L$, where n_1 is a constant depending on the shape, size and material of the antenna as well as the medium, and L the arm length (see chapter 2). Additionally, each symmetric antenna also features shorter wavelength modes at $3\lambda_{\text{res}}/2 = n_1 L$, $5\lambda_{\text{res}}/2 = n_1 L$, etc. These higher order modes are supported by the current oscillations inside the antenna arms. The even modes ($2\lambda_{\text{res}}/2 = n_1 L$, $4\lambda_{\text{res}}/2 = n_1 L \dots$) are dark modes due to symmetry, i.e. they are non-radiative [23]. For our measurements, this means that resonances with a factor of two between their wavelengths cannot come from dimer antennas with an intact gap. Instead, they signify short-circuited antennas with $\lambda_{\text{res}}/2 = n_1 L_2$, where L_2 is the doubled arm length.

So all peaks in air in Fig. 6.4 and Fig. 6.5 that are coinciding with the simulated peaks (Fig. 6.8), are coming from antennas with an intact gap. Intact dimer antennas seem to be present at least to some extent in every sample set. The low-dose set shows only this mode for some antenna lengths, and for the lower density single antennas in Fig. 6.5(a), it is the case for all sizes. The antennas that were written with the higher dose show both resonances and have therefore a mix of antennas with an intact and with a short-circuited gap. This also explains the varying amplitude

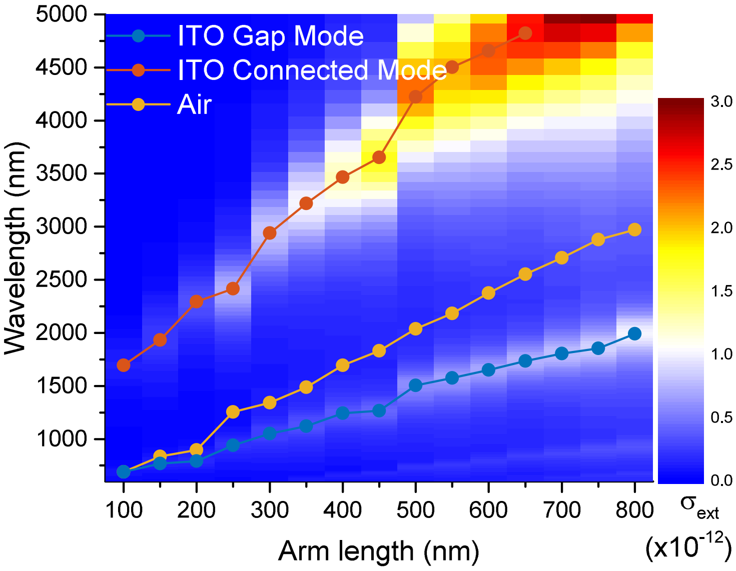

(a)

Figure 6.8: Simulated IR spectra for gap-loaded antennas. Simulations were done in Lumerical with longitudinal polarisation and an ITO carrier concentration of $N = 3 \times 10^{21}\,\mathrm{cm}^{-3}$. The peak line for antennas in air is shown for comparison.

of the different modes.

In the case of ITO gap-loaded antennas in the $500\,\mu\mathrm{C\,cm}^{-2}$ set, the behaviour is similar to that of bare antennas. In the $500\,\mu\mathrm{C\,cm}^{-2}$ set, the gap-loaded antennas exhibit further resonance, i.e. the modes 3 and 4 in Fig. 6.4(b). The ITO mode 4 appears at a third of the wavelength of the ITO mode, so it is likely the third order mode of the fused monomer $3\lambda_{\text{res}}/2 = n_1 L_2$. The last resonance to be allocated is mode 3, which is located at a wavelength a factor of 1.8 shorter than mode one and slightly longer than mode 2. A certain explanation for this mode could not be found. It is possible that it is the dark mode of mode 1, made visible due to the slight asymmetry in the ITO disc placement. An imperfect scaling due to the monomer size being larger than exactly two arms (i.e. including the size of the gap) would account for the resonance's peculiar spectral location.

Simulations with Lumerical are shown in Fig. 6.8, which were done using the dimensions and shape found in the SEM images. The arms were modelled as rectangular arms with semi-circular end caps. The air peak lines, agree well with the mode 2 of the FTIR modes and the dominant SMS modes, so that it can be assumed that these modes are the fundamental modes of the antenna. In the $500\,\mu\mathrm{C\,cm}^{-2}$ set, these modes are at slightly lower wavelengths than simulated and in the $550\,\mu\mathrm{C\,cm}^{-2}$ set at slightly higher wavelengths, which can be attributed to small size variations of the antennas due to the dose difference. Introducing the ITO gap-load into the simulations generates a long wavelength resonance similar to the one observed in the experiments. The third order of that mode can also be observed at below $1000\,\mathrm{nm}$. However, it has to be stressed that the experimental spectra show the connected mode even without the presence of ITO. Additionally, the simulated blue-shift of the fundamental antenna mode upon the introduction of ITO is not observed experimentally.

The influence of the fabricated ITO in terms of spectral shift is small in both sets. Most spectra feature no shift or a slight red-shift, except for the $350\,\mathrm{nm}$ and $450\,\mathrm{nm}$ arm length antennas of the $500\,\mu\mathrm{C\,cm^{-2}}$ set, which show a blue-shift in the SMS peaks and the long wavelength mode of the FTIR. The effect was much larger for the previous sample with only single antennas, where resonances were red-shifted by several hundred nanometre. This small impact on the resonance could show an ITO refractive index close to that of air. However, it is unlikely that it would occur over the whole wavelength range, which leads to the conclusion that the ITO on the current sample does not show any of the expected optical properties of ITO. Instead the ITO seems to behave like a dielectric with a spectrally constant low refractive index, which was connected to the unreliable ITO deposition process. As mentioned in chapter 3.1.2, this was afterwards improved, however a further fabrication run could not be implemented within the time-frame of this thesis. The notable appearance of the FTIR modes 3 and 4, which are only present in the $550\,\mu\mathrm{C\,cm^{-2}}$ set with ITO gap-loading, shows a change in conductance inside the gap. It is the only significant impact that could be assigned to the ITO gap-load.

6.2 Titanium nitride antennas

For plasmonic devices, TiN is a promising candidate as an alternative material, as described in section 1.1.2, due to its CMOS-compatibility and high carrier concentrations. Additionally, its permittivity has a higher sensitivity $\partial\varepsilon_r'/\partial\lambda$ than gold, making it more sensitive to changes of the particle shape and the surrounding medium. For this reason, TiN antennas were fabricated and their shapes and optical properties characterised. For the development of the fabrication processes for patterning TiN, which are described in this section, the author acknowledges strong support by Dr. Yudong Wang.

While initial attempts to directly deposit TiN in the correct pattern from sputtering were not fruitful, two etching processes resulted in accurate antenna shapes and dimensions. Currently, an etching process using a single layer of ZEP holds the most promise to become a standard for TiN nanoantenna fabrication. The following chapter describes the two different fabrication methods that were followed in the search for a working fabrication recipe.

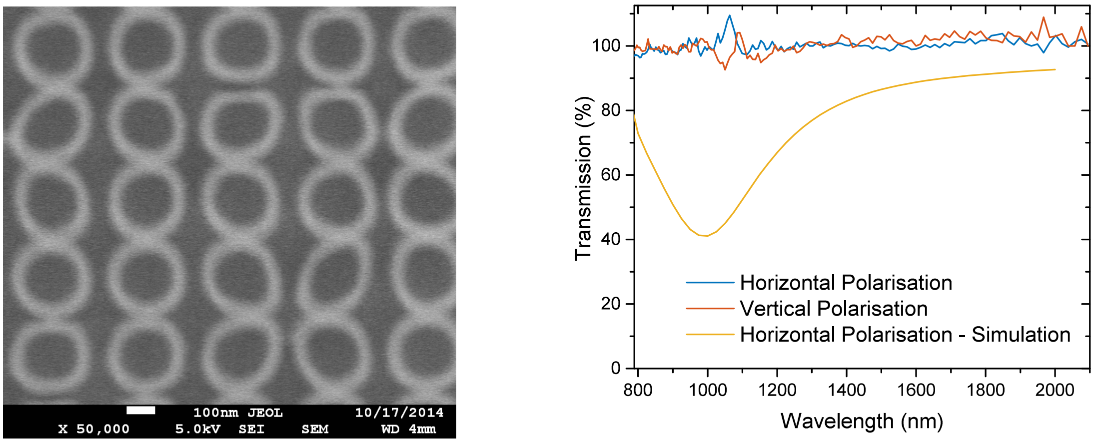

(a) **(b)**

Figure 6.9: TiN array with dimensions of 240 nm×250 nm×30 nm: (a) scanning electron microscopy, courtesy of Yudong Wang; (b) measured transmission spectra and spectrum simulated with COMSOL.

6.2.1 EBL using tri-layer patterning

TiN was deposited onto a CaF_2 substrate using sputtering, which contrary to evaporation is an isotropic deposition method and tends to coat side walls. For a standard e-beam lithography process, this means that the deposited material is removed with the resist during lift-off. To circumvent this issue, a tri-layer process was used, as described in section 3.1.1. The greater resist thickness prevents the deposited material from being connected to the rest of the film.

An SEM image of the developed resist before deposition is shown in Fig. 6.9(a). The TiN patterns were designed as circles, yet the resist patterns are ellipsoidal in shape with a width of 240 nm and lengths from 250 nm to 500 nm. Smaller dimensions were not possible with this design, since the TiN deposition was highly isotropic, and thus deposited at large angles. Therefore, it was expected to cover the side walls if the pattern size was smaller. An array of antennas extending over an area of $100 \times 100\,\mu\mathrm{m}^2$, consisting of TiN circles with dimensions of $240\,\mathrm{nm} \times 250\,\mathrm{nm} \times 30\,\mathrm{nm}$, was measured in transmission spectroscopy to obtain the optical extinction of the antenna ensemble. The transmission was normalised to a nearby area of the bare CaF_2 substrate. The resulting spectra for two polarisations is shown in Fig. 6.9(b). Apart from a small peak at 1100 nm, no features can be distinguished against the noise. The TiN seems to show no absorption or scattering, and the slight peak is considered to be an artefact from the excitation laser peak at 1064 nm. Normalisation around the peak can create spikes due to small fluctuations of the laser intensity. The simulated spectrum is shown in Fig. 6.9(b), which was modelled in COMSOL as a periodic array with an interparticle spacing of 600 nm. At

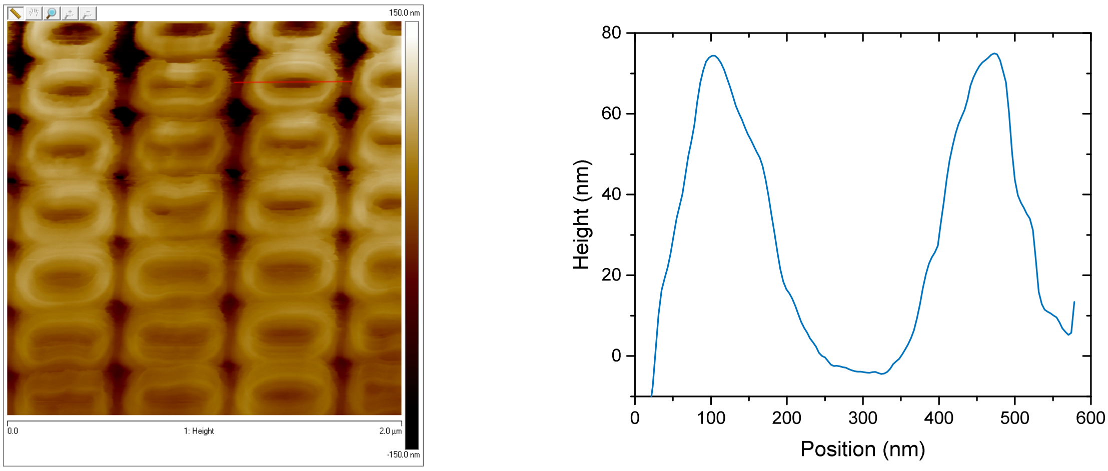

(a) **(b)**

Figure 6.10: Atomic force microscopy profiles: (a) false-colour height image of a TiN array; (b) height profile of a TiN particle along the red line indicated in (a).

1000 nm, the transmission dips to 40%, indicating a plasmonic resonance. No such resonance was observable in the experiments.

To verify the particle shapes, AFM measurements were performed on the sample. Figure 6.10(a) shows the height of the TiN in false-colour. The particles appear to have a peculiar cup-like shape with high walls and a very thin bottom. A cross-sectional profile of one TiN particle is given in Fig. 6.10(b) where the cup walls are shown to be over 70 nm high. The exact thickness at the bottom could not be determined due to the lack of a reference surface sufficiently close. Due to the non-uniform distribution, it can be assumed to be much less than the targeted 30 nm, which explains the absence of extinction in the optical measurements. The reason for these side walls is the wide spread of the sputter deposition, meaning that the chosen MMA thickness of 400 nm was still not enough. However, a further increase of the height might cause the structures to collapse, since the SEM image already shows strong variations in the shape and position of the resist pattern. Therefore, a new patterning method had to be found.

6.2.2 Negative resist fabrication

Another sample was fabricated using a negative e-beam resist with subsequent dry etching. A negative e-beam resist is a resist, from which upon development the unexposed area is removed. It is a useful way to save time when writing e-beam patterns for etching. Since the space between the antennas is larger than the area occupied by the antennas, writing that area in a positive resist can take a significant amount of time. Apart from the chosen resist, the process is the same as for single layer EBL.

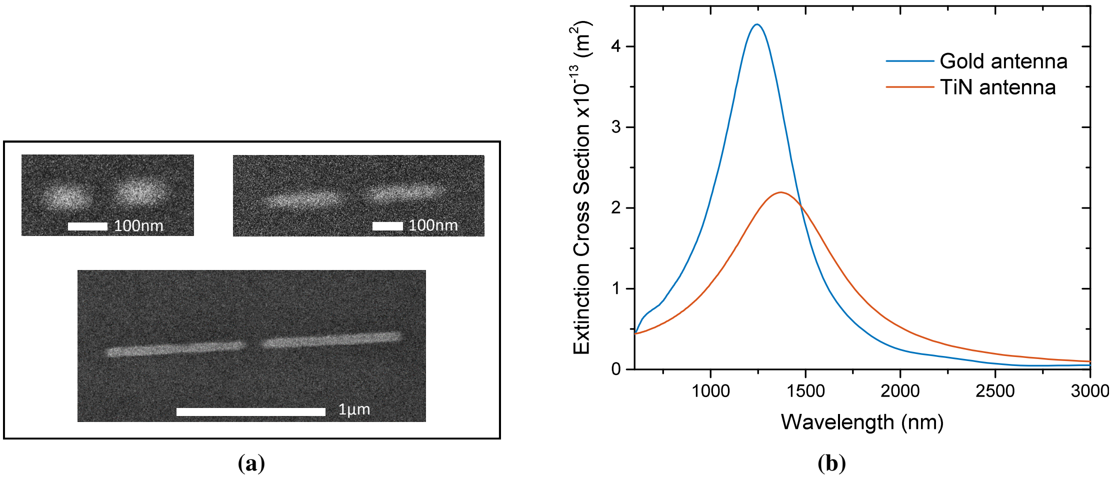

(a) **(b)**

Figure 6.11: (a) SEM of TiN antennas with lengths of $100\,\mathrm{nm}$, $250\,\mathrm{nm}$ and $1000\,\mathrm{nm}$. (b) Extinction cross-section spectra of a $250 \times 100 \times 30\,\mathrm{nm}^3$ arm dimer antenna with a $30\,\mathrm{nm}$ gap, simulated with Lumerical.

A TiN thin film with a thickness of $30\,\mathrm{nm}$ was deposited by sputtering and then coated with $50\,\mathrm{nm}$ of the resist HSQ. While in the first try the antenna arrays did not suffered from underexposure, the single antennas were well-defined. Example SEM images of the antennas with a length of $100\,\mathrm{nm}$, $250\,\mathrm{nm}$ and $1000\,\mathrm{nm}$ are shown in Fig. 6.11(a). Though the TiN appeared to be a weak scatterer and obtaining high quality SEM images was challenging, the shape and separation can be seen to match the desired parameters.

Simulated extinction cross-section spectra using Lumerical are shown in Fig. 6.11(b). Both of the antennas had the dimensions $250\,\mathrm{nm} \times 100\,\mathrm{nm} \times 30\,\mathrm{nm}$ for their arms and a $30\,\mathrm{nm}$ gap. The material properties of TiN were taken from ellipsometry measurements performed on the fabricated thin film. As can be seen, the extinction peak of a TiN antenna is lower than that of a gold antenna. This is due to higher optical losses which broaden and weaken the resonance. The peak is also red-shifted from $1246\,\mathrm{nm}$ to $1372\,\mathrm{nm}$ compared to gold due to the lower permittivity of TiN.

The height of the antenna structures was characterised with AFM measurements, which are given in Fig. 6.12. Fig. 6.12(a) shows a false-colour height image for a set of single antennas. Figure 6.12(c, d) are height profiles extracted from Fig. 6.12(a) and show the length scaling. The comparably low resolution limits the precision of the height measurement. A finer scan was was carried out on the $750\,\mathrm{nm}$ antenna and is shown in (b). The TiN film thickness of $30\,\mathrm{nm}$ is well-matched by the antenna structure.

To characterise the antennas, spatial modulation microscopy was performed. The individual antennas proved challenging to measure, because the reflected signal was significantly lower than

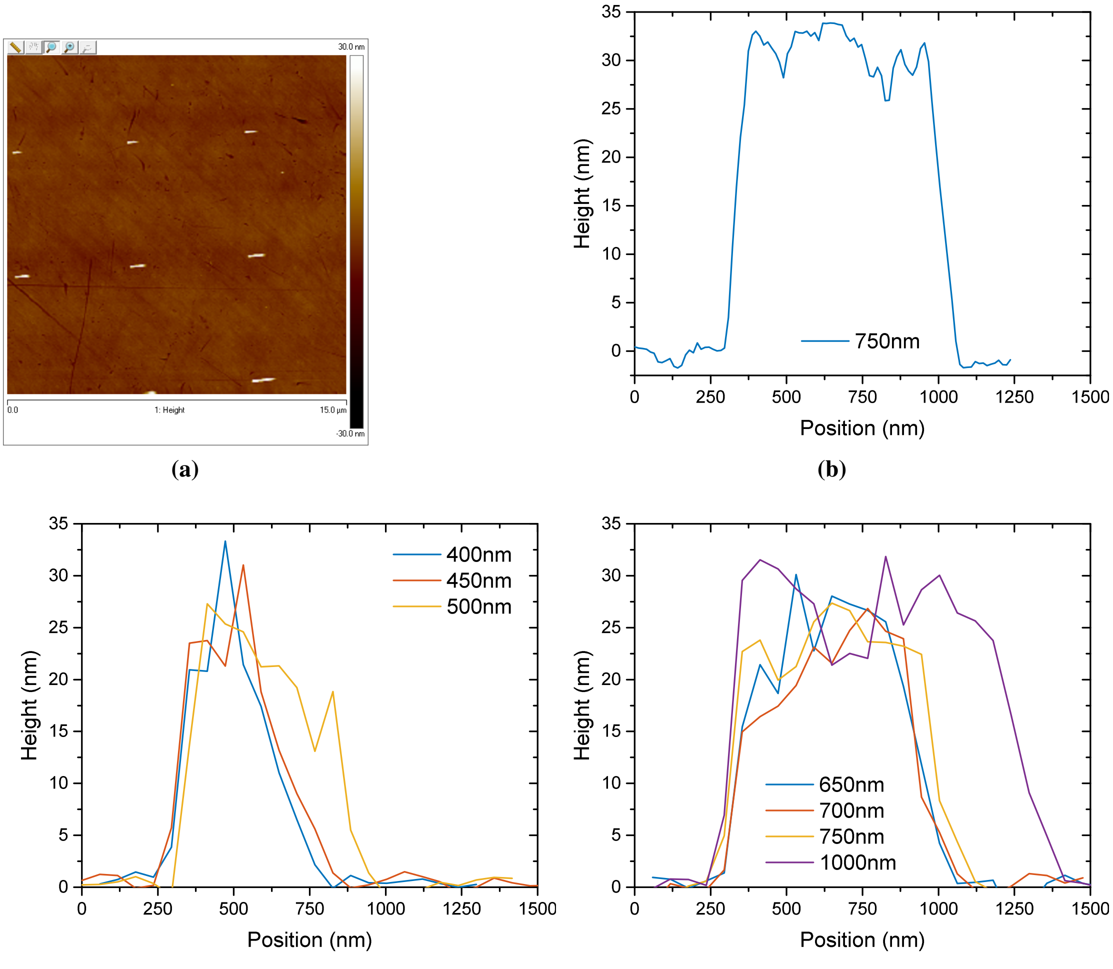

(a)

(b)

(c)

(d)

Figure 6.12: AFM height profiles of TiN single arm antennas. (a) False-colour height image of antennas with arm lengths from $400\,\mathrm{nm}$ to $1000\,\mathrm{nm}$. (b) Fine cross-section of a $750\,\mathrm{nm}$ antenna. (c, d) cross-sections extracted from the antennas visible in (a).

for the previously measured gold antennas. Therefore, it was difficult to know if the antenna was inside the beam. The high sensitivity to misalignment of the setup meant that many spectra of the same antenna differed drastically between measurements. With care, some repeating patterns were distinguished from several measurements and are presented for the $300\,\mathrm{nm}$, $350\,\mathrm{nm}$ and $450\,\mathrm{nm}$ arm length single antennas in Fig. 6.13(a). Since the signal-to-noise ratio was low, the spectra were averaged over four measurements in the case of $300\,\mathrm{nm}$ and $350\,\mathrm{nm}$ antennas and two measurements for $450\,\mathrm{nm}$. For the other antenna dimensions, no consistent spectra could be found.

The extinction cross-section is a whole order of magnitude lower than that of gold antennas,

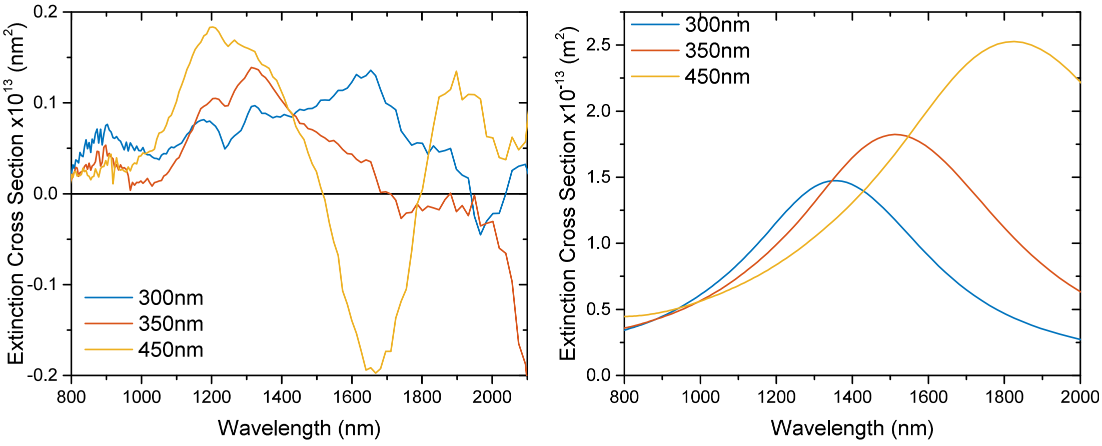

(a)

(b)

Figure 6.13: (a) Spatial modulation spectra for single TiN antennas on glass. The graphs were averaged over four (300 nm and 350 nm) and two (450 nm) measurements. (b) Lumerical simulation spectra of the same antennas.

e.g. in Fig. 6.5. A small peak around 900 nm and a larger one between 1200 nm to 1300 nm can be distinguished for all three antennas. The 300 nm antenna shows another peak at 1650 nm, where the 450 nm has a dip which goes into the negative. Due to the low signal-to-noise ratio, the spectral range above 1500 nm is not sufficiently meaningful. However, in the rest of the spectrum, the three different antennas behave very similar. It is not possible to distinguish any length-dependent feature.

Lumerical simulations for single TiN antennas of the fabricated sizes are shown in Fig. 6.13(b). Though the resonances are broad, they are still clearly distinguishable and show a continuous red-shift with increasing length. Contrary to the measurements, the amplitude is comparable with that of gold antennas. The peak for the 450 nm antenna around 1825 nm seems to overlap with a measurement peak at 1897 nm. The peaks of the other two simulated lengths have no counterpart in the measurements. The two peaks all measurements share can either be artefacts due to the measurement system or reflection properties of the TiN that do not depend on the antenna size.

Since the shape of the antennas is well defined, a possible explanation for the lack of length scaling, which is a key property of plasmonic structures, is that the antennas are not or not completely consisting of TiN. The material could have been altered in the fabrication process. TiN can oxidise to TiO_2 [79] at high temperatures. This occurs at several hundred degrees Celsius, where it takes more than an hour to penetrate 100 nm into the film. During the fabrication of the TiN antennas, the sputtered TiN thin film is coated by HSQ and then baked at 500 °C for 1 h. HSQ itself is not an aggressive chemical, but its solvent contains oxygen. It is possible that the TiN oxidises at this step, if at all. During the rest of the fabrication and the measurement steps, the sample is always handled at room temperature. A TiO_2 antenna would not experience plasmonic behaviour since TiO_2 is a dielectric. This would also explain the low measured reflectivity while the simulated resonance amplitude is comparable to that of gold.

In a recent paper, TiN antennas were successfully grown in a similar process [81]: to create antenna arrays, nanoimprinting was used to create a pattern into the resist with subsequent dry-etching to transfer the pattern into the TiN layer. The resist and its patterning are the main differences to the process used for this work, further supporting the hypothesis that the HSQ could be the issue.

6.3 Chapter summary

To summarise the findings, the placement of ITO disks into the gap of dimer nanoantennas was successfully demonstrated. Height alignment errors from the automatic height measurement of the e-beam system were corrected by depositing chromium pads far away from the antennas. The sample with only individual antennas showed a systematic red-shift induced by the ITO gap-load which could be attributed to a low carrier concentration of the ITO. This sample can be used for pump-probe spectroscopy in future experiments. In the subsequent repetition of the work using the antenna array sample, not all the gold dimer antennas had an intact gap. In future work, to ensure separation of the antenna arms, the nominal gap could be increased, or a different resist could be tried to ensure sharp antenna edges and reduce gap size fluctuations. The partially connected antennas can also be of interest in future work due to their increased nonlinear optical behaviour [25].

Moreover, the ITO deposited onto the antenna array sample had a small influence on the antenna resonances. Its presence was verified by the SEM images and while it is possible that for one antenna size the carrier concentration matches the case where no shift occurs, this is practically impossible for the large arm length and resonance wavelength range under investigation. A possible explanation is the increased surface area of ITO nanostructures compared to thin films, which influences the annealing process. Compared to the deposition of an ITO film, for which the recipe was designed, the ITO could be over-annealed and thus have a lower carrier concentration than anticipated. However, the non-Drude behaviour was also found in one of the ITO prototypes for the metareflector structure studied in chapter 4. It occurred only in some of the deposition runs, where it did not match the behaviour expected from the carrier concentration obtained by Hall measurements. The logical conclusion was that the ITO deposition recipe was unstable and did not always produce the desired material. This finding led to the development of an alternative ITO deposition recipe using an ion gun, which was described earlier in chapter 3.1.2.

The work on TiN nanoantennas could not be concluded successfully, however it provided a series of useful insights into the patterning of TiN. Due to the isotropic nature of sputtering, a direct patterning by lift-off is not feasible. Post-deposition etching appears to be the method of choice, though the negative resist HSQ could be responsible for the lack of plasmonic resonances in the patterned nanoantennas. Other resists such as ZEP520A could be more suitable for future work.

7 Experimental demonstration of electrically tuned plasmonic structures

The electrical control over plasmonic resonances, which is the main topic of this thesis, promises a new degree of freedom in the fabrication and application of plasmonic sensors, tunable reflectors and metamaterials. In this chapter, the experimental work on electrically tunable samples will be presented. The device design with a sandwich structure of the three main materials (metal, insulator and TCO) represents the initial concept of how optical antenna resonances can be modulated. The measured optical spectra with and without electrical modulation are presented here. Part of the experimental results were recently presented at the conference *CLEO Europe/ECEQ 2017*.

During the experimental work, several issues were encountered where the design of the device limited the performance. These were afterwards solved by the simulated design presented in chapter 5. It follows naturally that this chapter will deal with device designs that were conceived at an earlier time than the ones presented in chapter 5.

7.1 Simulations and performance analysis

The schematic of the sample is depicted in Fig. 7.1(a). Gold dimer antennas are embedded in ITO, whose carrier concentration is modulated by a MOS structure, consisting of a TiN back contact, $100\,\mathrm{nm}$ HfO_2 insulator and the ITO. The design follows the idea presented in reference [167]. Voltages of $\pm 10\,\mathrm{V}$ allow high carrier accumulation and depletion, which occur in a nanometre-thin film on top of the insulator. The change in carrier concentration modulates the refractive index of the ITO in that region, leading to a shift of the antenna resonance.

The simulations of the final multilayer structure are shown in Fig. 7.1(b). The bare antenna on glass (dark blue line) exhibits a resonance at $1246\,\mathrm{nm}$. Changing the insulator to $100\,\mathrm{nm}$ of HfO_2 gives a strong red-shift to $1558\,\mathrm{nm}$ and a decrease in amplitude (red line). An added TiN bottom contact further red-shifts to $1740\,\mathrm{nm}$ (yellow line). The purple line depicts the case coated with ITO with a carrier concentration of $1 \times 10^{19}\,\mathrm{cm}^{-3}$ and a thickness of $120\,\mathrm{nm}$. The high refractive index of this low carrier concentration ITO is around 2 for most of the observed wavelength range, giving another large red-shift to $2288\,\mathrm{nm}$. This is a much longer wavelength

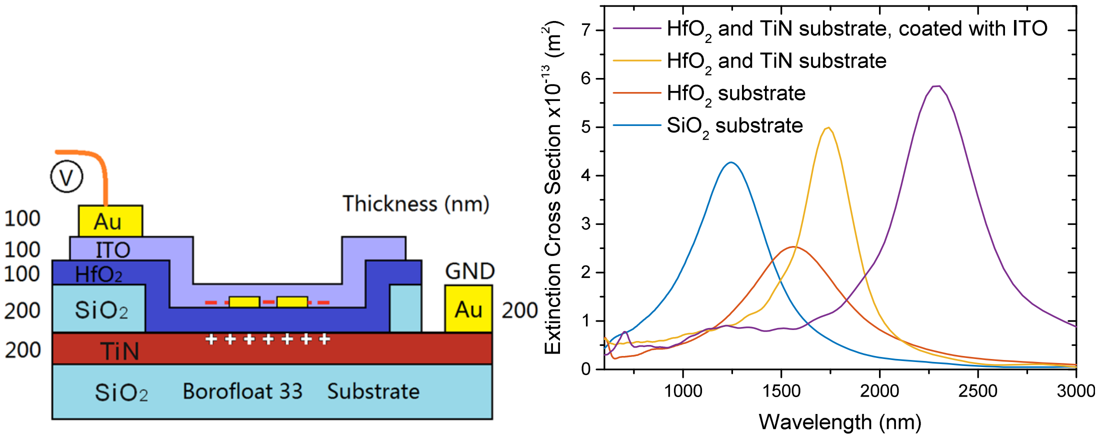

(a) **(b)**

Figure 7.1: (a) Cross-sectional schematic of the design of the electrically controlled sample. (b)Resonance wavelength of a gold dimer antenna with $250 \times 100 \times 30\,\mathrm{nm}^3$ arms and a $30\,\mathrm{nm}$ gap embedded in various structures. The final structure shown in (a) is built up layer by layer. The HfO_2 thickness is $100\,\mathrm{nm}$.

than for a bare antenna on glass, which imposes new challenges because the measurement system has to be sensitive in that area. It also limits the maximum antenna arm length that can be measured optically.

2D simulations using Lumerical DEVICE give an insight into the modulation strength of the design. An ideal modulation not only moves many carriers, but also does this over a large volume that allows a good overlap with the antenna near-field. The latter usually expands over $100\,\mathrm{nm}$ away from the antenna, as was found in chapter 3.3.3. Figure 7.2(a) shows the calculated electron density distributions for the sample with $100\,\mathrm{nm}$ HfO_2. In electrical testing, breakdown voltage of $12\,\mathrm{V}$ was found, wherefore the applied voltage was adjusted to $10\,\mathrm{V}$ as the allowable maximum. The ITO background carrier concentration is $4 \times 10^{20}\,\mathrm{cm}^{-3}$, as in the manufactured sample. At $0\,\mathrm{V}$, the simulation shows an intrinsic carrier depletion at the semiconductor-insulator interface, which comes from the different work functions of the layers. The accumulation under positive bias goes up to $1.4 \times 10^{21}\,\mathrm{cm}^{-3}$. However, it occurs only over a small thickness of below $1\,\mathrm{nm}$. Depletion occurs over a larger thickness, but with a lower amplitude, giving the same total amount of moved carriers.

Entering the carrier distribution into the optical FDTD solver, the spectra under bias can be computed. They are shown in Fig. 7.2(b) for the same structure as described in the previous section, with a gold dimer antenna with $250 \times 100 \times 30\,\mathrm{nm}^3$ arms and $30\,\mathrm{nm}$ gap size. The spectra show a small resonance shift of $10\,\mathrm{nm}$ in each direction. The amplitude changes asymmetrically, indicating that the antenna reacts differently to accumulation and depletion. A

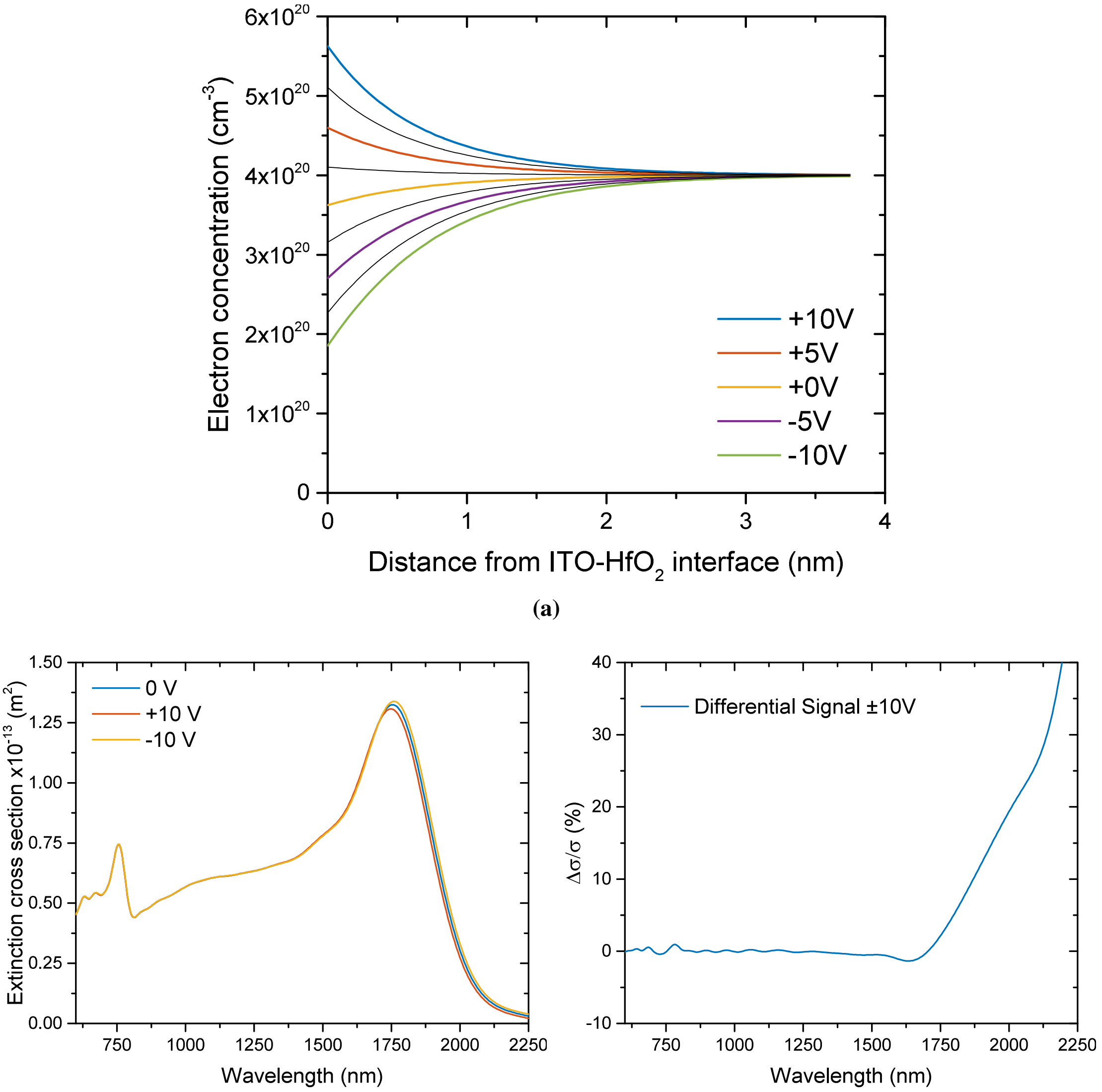

(a)

(b) **(c)**

Figure 7.2: (a) Electron concentrations calculated with Lumerical DEVICE for the multilayer structure with $100\,\mathrm{nm}$ HfO$_2$ as a function of applied voltage. (b) Optical simulations of the structure with a gold dimer antenna with $250\,\mathrm{nm} \times 100\,\mathrm{nm} \times 30\,\mathrm{nm}$ arms and $30\,\mathrm{nm}$ gap size as a function of voltage. (c) Differential signal from the spectra of (b) normalised to the $0\,\mathrm{V}$ spectra. The ITO carrier concentration is $4 \times 10^{20}\,\mathrm{cm}^{-3}$.

possible explanation is that depletion acts on a larger volume and has thus more interaction with the optical near-field. The asymmetric differential signal is shown in Fig. 7.2(c). The asymmetric modulation leads to only a positive peak of the differential at long wavelengths. The modulation amplitude increases continuously with wavelengths, which is caused by the decreasing amplitude of the resonance, to which the modulation is normalised. At the full-width at half-maximum of the resonance at $1800\,\mathrm{nm}$, the modulation amplitude is 10%. The location of the resonance is expected to scale with antenna arm length, so shorter arm lengths should provide electrical modulation in the measurable spectral range from $800\,\mathrm{nm}$ to $2500\,\mathrm{nm}$.

7.2 Experimental demonstration of electro-plasmonic modulation

For the sample, $100\,\mathrm{nm}$ TiN was sputtered on a glass wafer, which was then cut into chips. On these, $100\,\mathrm{nm}$ of HfO_2 was deposited using a plasma ALD process. The thickness of HfO_2 was confirmed via ellipsometry. On the thus prepared chips, antenna structures were written with a variety of gap and arm size. On top of these, $200\,\mathrm{nm}$ SiO_2 was deposited via PECVD, which was afterwards selectively etched around the antennas using RIE. The resulting open windows were filled with e-beam evaporated ITO using the first recipe detailed in section 3.1.2. On the side of the ITO window, on top of the SiO_2, $100\,\mathrm{nm}$ thick gold pads were deposited that overlapped with ITO and ensured electrical contact. All patterning for the antennas and the material windows was done using e-beam lithography with a bi-layer resist, a process that was largely supported by Dr. Yudong Wang. During the fabrication of the sample, an ITO reference film was made during the same deposition run as the sample and was measured to have a height of $120\,\mathrm{nm}$ and a carrier concentration of $1.2 \times 10^{21}\,\mathrm{cm}^{-3}$ (Hall measurement). As will be seen later, similar to the observations made in chapter 6.1, the optical ITO behaviour is different from what would be concluded based on the Hall measurement. Chronologically, the work in this chapter was begun at the same time as the ITO gap-loaded nanoantennas (chapter 6.1), which is why an improvement of the ITO deposition was not yet implemented.

In our design, the carrier modulation occurs within a thin part of the ITO on top of a HfO_2 insulator. Because of that, the whole multilayer structure creates interferences which can be electrically modulated. In Fig. 7.3(a) is shown the simulated and measured reflectivity of the multilayer structure in the absence of antennas (here called *bare ITO*). The measured spectra was normalised by dividing the reflectivity of the multilayer structure by that of a nearby gold pad, which are both shown in Fig. 7.3(b). As can be seen, the resulting spectrum shows two dips and one peak, the dips occurring at $743\,\mathrm{nm}$ and $1586\,\mathrm{nm}$, and the peak at $1057\,\mathrm{nm}$. The properties of the ITO were fitted by changing simulation parameters of the interference structure. Bare TiN reflects the light strongly (dark blue line). Adding $100\,\mathrm{nm}$ HfO_2 on top creates a destructive interference dip at $1024\,\mathrm{nm}$ (bright red line). Adding ITO splits the destructive interference into

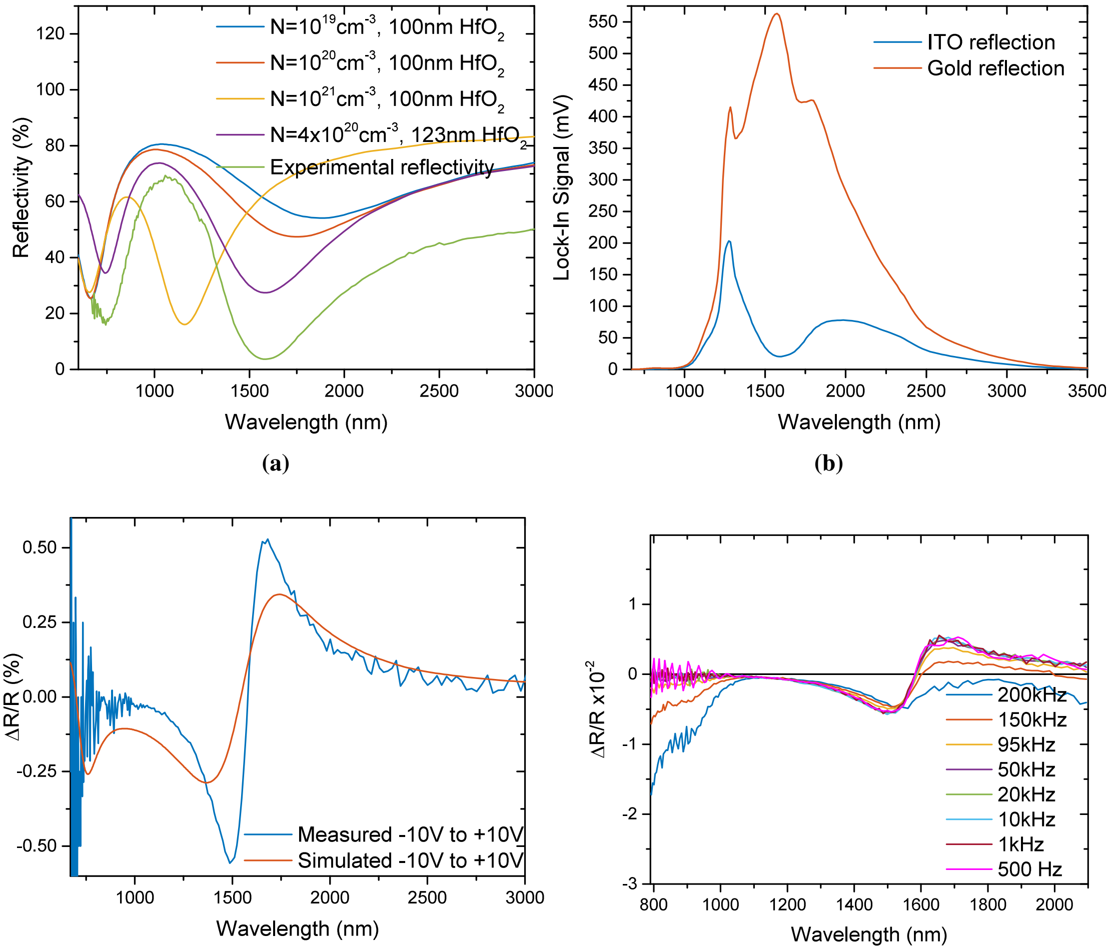

(a) **(b)**

(c) **(d)**

Figure 7.3: (a) Simulated and measured reflection spectra of the multilayer structure without antennas. The simulation fit was achieved by starting with bare TiN on a glass substrate and adding top layers as indicated. The green line represents the measured intensity signal normalised to that of a nearby gold pad, both shown in (b). (c) Electrical modulation signal from the multilayer structure without antennas. (d) Frequency sweep of the electrical modulation for ±10 V.

two dips separated by one peak, with spectral positions depending on the carrier concentration (yellow, purple and green lines). Since the ITO refractive index in the visible range changes weakly with carrier concentration, the first dip can be used to determine the HfO_2 thickness. In a second step, the carrier concentration of the ITO can be determined to compare the simulation results with the measurement. This leads to a HfO_2 thickness of $123\,\mathrm{nm}$ and an ITO carrier concentration of $4 \times 10^{20}\,\mathrm{cm}^{-3}$. The carrier concentration is significantly lower than the value obtained by Hall measurements, as mentioned before. Regarding the increased HfO_2 thickness necessary to match the experimental spectrum, it is possible that part of the TiN layer oxidised during the plasma ALD process. That layer of TiO, being a dielectric would be represented by the increased HfO_2 thickness. As a general trend, it can be noted that reflection in the simulation is higher than in the measured spectra, because the simulation assumes lower material losses and no fabrication imperfections.

Figure 7.3(c) shows the electrical modulation spectra of the ITO without antennas. It is compared to the results from combined electro-optical simulations using Lumerical FDTD and DEVICE. The electrical modulation spectra consist of a negative peak followed by a positive one. The polarity change occurs at $1586\,\mathrm{nm}$, the dip of the reflection signal. No asymmetry between positive and negative voltages was observable. The electrical modulation of the bare ITO can therefore be understood as a spectral shift of the destructive interference dip. The maximum reflectivity change is 0.5%. The simulated spectra agree well, except for their lower modulation amplitude. This can be attributed to the reflectivity of the dip in Fig. 7.3(a), which is greater than in the experiments, leading to lower values after normalisation. In the simulated spectra, the second reflection dip also experiences modulation. This is however not observable through the large noise of the experimental signal in that spectral range. Overall, the properties of the modulated structure are well represented by the simulation.

Further electrical modulation spectra are shown in Fig. 7.3(d). A frequency sweep was performed to characterise the response of the structure with increasing frequency. The resulting spectra are similar in shape, but show some differences in the signal-to-noise ratio and the modulation amplitude. Frequencies of $1\,\mathrm{kHz}$ and lower show increased noise. For frequencies higher than $95\,\mathrm{kHz}$, the signal is distorted at short wavelengths and above $1600\,\mathrm{nm}$. The distortion is attributed to the lock-in amplifier, whose maximum frequency is given as $200\,\mathrm{kHz}$. For $100\,\mathrm{kHz}$, strong spectral oscillations were observed (not shown), which were stable over several runs. These oscillations were not observed for any other modulation frequency and render modulation at $100\,\mathrm{kHz}$ infeasible. In conclusion, the electrical modulation can be performed reliably in a frequency range from $10\,\mathrm{kHz}$ to $95\,\mathrm{kHz}$.

For the spatial modulation measurements, the areas with antenna gap sizes of $55\,\mathrm{nm}$ and $80\,\mathrm{nm}$ were selected, because those were fabricated accurately and gave reproducible measurements. As was shown in the case of the ITO gap-loaded structures, $50\,\mathrm{nm}$ sometimes led to a short-circuiting of the antenna arms, so larger gaps were preferred for this project. The sample position was kept constant when switching between modulation types to ensure the laser stayed on the antenna. The nominal antenna width was $100\,\mathrm{nm}$ and the height $30\,\mathrm{nm}$, while antenna lengths of $50\,\mathrm{nm}$ to $500\,\mathrm{nm}$ were available. Due to a tight e-beam lithography schedule at the time of fabrication, no SEM images of the antennas were made. For future purposes, the SEM images could be obtained by etching a SiO_2 window into one of the areas covering further antenna arrays. Until then, due to the similarity of the structures with those described in chapter 6.1, the same shapes can be assumed for the following discussion. The spectra shown in Fig. 7.4 were taken using spatial

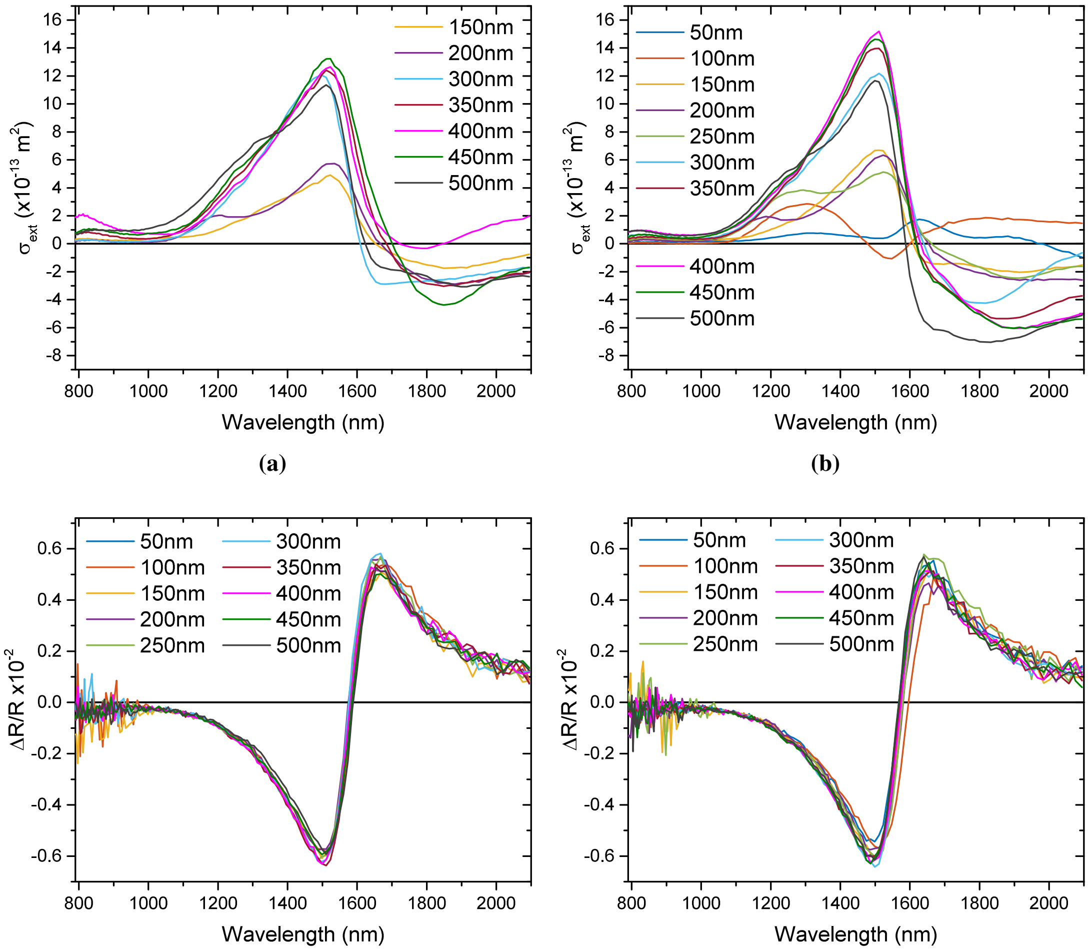

(a) **(b)** **(c)** **(d)**

Figure 7.4: Spectra taken from gold dimer antennas of lengths as indicated in the legends, with $100\,\mathrm{nm}$ width, $30\,\mathrm{nm}$ height. The gap size was $55\,\mathrm{nm}$ (a, c) and $80\,\mathrm{nm}$ (b, d) respectively, with polarisation along the longitudinal antenna axis. (a, c) Spatial modulation spectra; (b, d) electrical modulation spectra.

modulation and electrical modulation microscopy.

The spatial modulation spectra show one or more plasmonic resonance peaks. The main peak appears to recur at similar wavelengths for different arm lengths, especially for arm lengths greater than $200\,\mathrm{nm}$. It is likely that the antennas show resonance pinning due to the surrounding ITO's refractive index being close to 0. For a carrier concentration of $4 \times 10^{20}\,\mathrm{cm}^{-3}$, the ENZ region is located at $2000\,\mathrm{nm}$, meaning that near that wavelength the plasmonic resonance is quenched.

Some parts of the spectra show a negative signal. While this can be a sign of beam alignment issues, in this case it appears quite consistently in the wavelength range above $1600\,\mathrm{nm}$. If the background signal, which is the measured reflectivity in Fig. 7.3(a), changes its phase, it can lead to a negative $\Delta R/R$ signal. The phase of the lock-in amplifier is calibrated at the centre of the spectral range, so that phase changes result in a negative signal. As can be seen in Fig. 7.3(a), the signal passes an interference minimum at $1600\,\mathrm{nm}$, which explains the negative signal in the SMS antenna spectra.

The electrical modulation was generated using a square modulation with an amplitude of $\pm 10\,\mathrm{V}$ and a frequency of $20\,\mathrm{kHz}$ to obtain a high signal-to-noise ratio. The spectra show a negative and a positive peak, with the polarisation change at around $1600\,\mathrm{nm}$. The spectra are very similar in shape and position for the varying antenna arm lengths. Additionally measured electrical modulation spectra for transverse polarisations showed the same results (not shown).

To analyse the contribution from the antennas, the electrical modulation spectra of bare ITO was subtracted from the spectra of the various antennas. The results are shown in Fig. 7.5. Some small features can be distinguished from the background. The negative peak of the transverse spectra and the positive peak of the longitudinal spectra seem to be increased by the presence of the antenna. The effect appears to be stronger for the larger antennas, however it's never the same antenna that gives the strongest enhancement. Exceptions are the the $300\,\mathrm{nm}$ antenna with $55\,\mathrm{nm}$ gap that has a much smaller effect for transverse polarisation than in the other three spectra. In the same plot the $50\,\mathrm{nm}$ arm antenna shows the highest peak, which is however questioned by the large noise that is present in that spectrum. In the $80\,\mathrm{nm}$ gap longitudinal plot, the $100\,\mathrm{nm}$ arm antenna shows a signal decrease rather than an increase, which comes from the fact that the antenna's electrical modulation spectrum is shifted with respect to the others' (see Fig. 7.4(d)). The $300\,\mathrm{nm}$ antenna with $55\,\mathrm{nm}$ gap seems to have an artefact in both polarisations, leading the strongest antenna influence in the normalised plots.

7.3 Impact of the results

The work on the modulator design offered insight into the complex mechanism that allows electro-plasmonic modulation. With that device, the electrical modulation of optical properties by carrier accumulation and depletion in ITO could be demonstrated. It was shown, that the measurement setup gives reliable results in the range of $10\,\mathrm{kHz}$ to $95\,\mathrm{kHz}$ and that single antenna spectra can be taken by switching between spatial and electrical modulation spectroscopy. However, a clear contribution of the nanoantennas on the electrical modulation could not be determined, indicating that the device design is not yet sufficiently optimised. One deficiency is the poor overlap of the carrier distribution, which occurs in a 2D sheet at the bottom of the ITO, and the antenna near-field, which is a $100\,\mathrm{nm}$ thick volume around the antennas. Another is the necessity of a large insulator thickness to separate the TiN electrode from the antennas. How coupling between TiN and the antennas can negatively impact the near-field confinement was

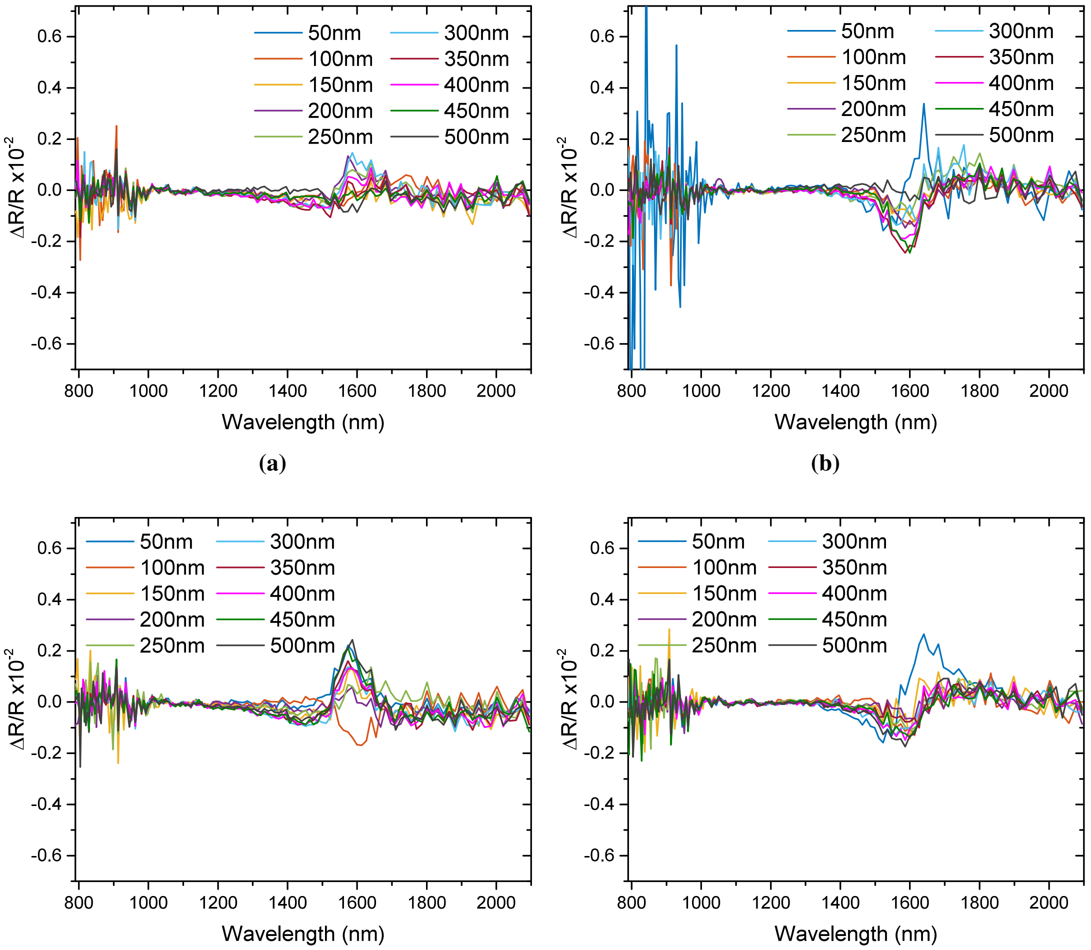

(a)

(b)

(c)

(d)

Figure 7.5: Spectra calculated by taking the difference between the electrical modulation spectra with and without the antenna. The antenna arm length is given in the legend, while the antenna width and height are $100\,\mathrm{nm}$ and $30\,\mathrm{nm}$, respectively. (a, b) Spectra for $55\,\mathrm{nm}$ gap and (c, d) for $80\,\mathrm{nm}$ gap antennas. Left column shows longitudinal, right column transverse spectra.

shown in chapter 3.3.3 on page 41.

While research was performed for the current chapter, two grating-based modulator designs were published by other groups [117, 119]. Instead of avoiding vertical coupling between the grating stripes and the bottom electrode, they utilised it by placing the ITO under the stripes. The resulting structure confined the near-field vertically, with a large part being located inside the ITO (cp. Fig. 5.1(a) on page 66). In turn they had to prevent horizontal coupling by widening the stripe separation. Though vertical coupling will not be pursued in this thesis, it is a worthwhile approach that deserves recognition.

The issues that were faced during the experimental work on this chapter were solved with the comprehensive electro-optical simulation model presented in chapter 5. Due to time constraints, the new design with directly addressable nanoantennas could not be fabricated and characterised within the scope of this thesis. Therefore, the author's experimental work on electrically tunable plasmonic structures concludes with the results presented in this chapter.

8 Conclusion and outlook

8.1 Thesis conclusion

The aim of this thesis was the demonstration and optimisation of electro-optical modulation using plasmonic nanostructures and transparent conductive oxides. As was discussed in the literature review, the electrical modulation of the carrier concentration of TCOs offers the most energy-efficient way of changing the refractive index of a material. While some preliminary work incorrectly overestimated the potential of electro-plasmonic modulation, current works of the groups of Harry Atwater and Mark Brongersma showed that strong optical modulation is achievable. The analytical theory developed in chapter 2 gave a qualitative description of the connection between the modulation of the refractive index and the obtainable resonance shift. Using this theory, the parameters that are necessary to maximise the impact of carrier accumulation and depletion on a plasmonic resonance were determined.

8.1.1 Simulations of optical devices

In the two chapters describing the simulation works of this thesis, an optical solar metareflector was designed to demonstrate the performance of AZO as a spectrally selective plasmonic material. Fabricated structures that were made according to the simulated design showed high reflectivity in the solar spectrum and high emissivity in the mid-infrared, thereby being able to act as a thermal dissipator. The developed meta-surface enabled reflection of the optical solar radiation to a great extent while providing a broad plasmonic resonance in the mid-infrared that serves as radiative emitter. Thanks to the plasmonic resonances created by the patterned structure, the device outperformed the unpatterned film and provides a light-weight, ultrathin and potentially flexible alternative to metallised quartz tiles. As a transparent conductive oxide alternative to ITO, AZO has the potential to reduce fabrication costs by reducing the dependency on indium, as well as offering highly controllable atomic-scale deposition.

The developed simulation model for nanoscale electrical carrier distributions and optical near-fields was utilised to provide a modulator design with maximised optical modulation. As a benchmark, experimental data from an external publication were chosen and compared to the results received when modelling the published device. The model was able to closely match the experimental results and gave confidence in the accuracy of the simulation. With this model, disadvantages of previous designs were successively removed. To reduce the amount of metal layers, which through optical coupling prevent the use of thin insulators, the nanoantennas were designed as electrically addressable electrodes. One way of increasing the electro-optical overlap, by coating the antennas with both the insulator and the ITO, was then analysed and found to support a particularly strong carrier modulation. However, it suffered from resonance pinning by the ENZ ITO, which reduced the modulation to changes of only the amplitude and not the resonance wavelength.

This hurdle was then circumvented by using an ITO gap-loaded design, where the ITO is deposited only inside the gap between the antenna arms. This completely removed the issue of resonance pinning and opened the way to a device with 45% relative optical modulation. Comparing this to the volume fraction in which the carrier density is modulated, the result is astonishing, because the antenna near-field covers a much larger volume than just the gap. The origin of the modulation lies in the partial short-circuiting of the gap by high-carrier ITO, which works on a thickness of less than a nanometre and cannot be described by the analytical theory presented earlier. The simulation shows that the thin layer of high-carrier ITO reduced the capacitive coupling between the two antenna arms and thereby lead to a blue-shift and amplitude decrease of the resonance. Additionally, the proposed modulator is the first to suggest modulation in both reflection and transmission, which adds a new mechanism to the library of electro-optical effects that can be used for plasmonic modulation.

8.1.2 Fabricated samples and designs

Fabrication and optical characterisation was done for several devices: the fabrication of gap-loaded nanoantennas provided a way to place ITO nanodisks into the gap of a gold dimer antenna, while the work on TiN nanostructures provided a basis for an alternative plasmonic material with higher sensitivity to carrier modulation.

The positioning of ITO inside a nanoantenna gap faced the challenge of a correct height measurement of the sample surface by the automated e-beam lithography system. Patterned or transparent surfaces gave incorrect readings on the order of tens of micrometres. Selective measurements on highly reflective pads deposited in the corners of the sample solved this issue. In the further process, the aim to demonstrate short-circuiting of the nanoantenna gaps suffered from fabrication tolerances of the bi-layer resist patterning, leading to dimer nanoantennas that were partially connected in the gap. This conductive connection caused the observation of two plasmonic resonances, one corresponding to a capacitive gap and one to a short-circuited gap. Since the role of ITO was also to short-circuit the gap, yet in a spectrally selective manner, its impact on the nanoantenna spectra could not be distinguished. Concomitantly, it was also found that the deposition recipe for ITO used up to that point was unstable and sometimes provided significantly lower carrier concentrations than intended. A new deposition recipe using ionised oxygen significantly improved the reliability of the process, which was characterised using advanced ellipsometry models to accurately obtain the optical constants of the material.

For nanoantennas made out of titanium nitride, a patterning recipe had to be developed. Direct sputtering into a patterned tri-layer resist structure was unsuccessful, and while an etching recipe using the negative resist HSQ and reactive ion etching gave the desired nanoantenna shapes, the TiN nanoantennas had poor reflection and showed weak plasmonic resonances. The exact reason for the deterioration of the TiN antennas could not be conclusively found.

8.1.3 Electro-optical modulators

The demonstration of electro-optical modulation was targeted with a structure where gold nanoantennas are fabricated on top of a TiN bottom contact and a HfO_2 insulator. The nanoantennas were then covered by a layer of ITO, which also provided the top electrical contact. The electrical modulation caused inside the ITO upon the application of an electrical bias over the insulator was simulated and measured. Optical spectra in the absence of nanoantennas showed that the multilayer sandwich gave an interference pattern that was spectrally shifted if a voltage was applied. The electrical modulation of optical properties of a structure could thus be demonstrated.

The nanoantennas, however, did not show an enhancement of this modulation, due to a lack of overlap between the electrical carrier modulation and the optical near-fields. The improved design that was developed through numerical simulations of the interactions of carrier distribution and optical near-field solved this issue, however it could not be realised within the scope of this thesis.

8.2 Outlook to future work

The field of plasmonic has been growing exceedingly quickly in the last few decades. New areas, such as the use of plasmonic structure for electro-optical modulation, are created every few years, pushing the boundaries of what can be achieved with photonics on the nanoscale. A decline of interest in the field can currently not be foreseen, which is why future work in the field of plasmonics, particularly in the area of electro-plasmonic modulation, can be expected for a long time.

A logical conclusion for future work is the fabrication of the device as it was presented in the electro-optical simulation chapter. The study was based largely on simulations, and while the accuracy of the developed model was proven to be high, findings between simulations of an ideal case and actual experimental results naturally differ. Lower breakdown voltages of the

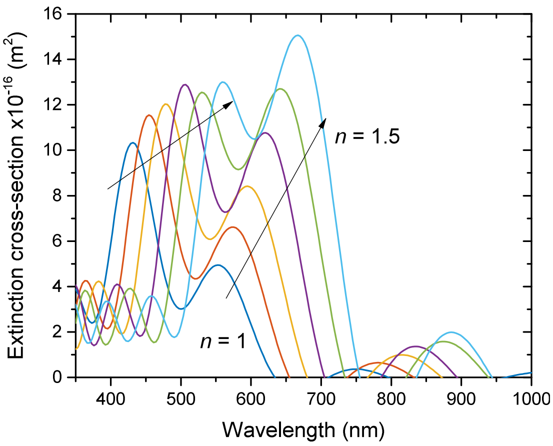

Figure 8.1: Extinction cross-section spectra of hybrid dimer nanoantennas with one silver and one gold antenna arm. The refractive index of the surrounding medium is changed from $n = 1$ (air) to $n = 1.5$. Simulation of the author, after reference [170].

insulator and larger antenna gaps can reduce the achievable modulation to values of $20\% - 30\%$, similar to the modulator designs published by other groups. However the design retains its unique properties such as modulation in transmission, as well as the sub-micrometer unit cell consisting of only one dimer antenna.

Two new experimental articles for electrical modulation have been published this year. One shows the use of diffusion of silver into ITO with applied electrical fields of $1\,\mathrm{mV\,nm^{-1}}$ [168]. The other demonstrated the influence of quantum effects on a surface plasmon resonance from a certain combination of ITO thickness, carrier concentration and resonance wavelength [169]. While classical models predict only a red-shift from carrier depletion (as is also done in this thesis), their experiments showed a blue-shift above a critical voltage due to localised carrier accumulation near the metal film. These articles show the continuous development of novel modulator designs for all sorts of applications.

New antenna materials have the chance to further increase obtainable modulation, and the search for them remains an important part of plasmonic research. The theoretical analysis showed that TiN nanoantennas shift the resonance stronger for a fixed refractive index change in the modulated medium. However it was also noted that this increased shift is countered by the broader resonance of TiN antennas, which is induced by the larger imaginary part of the permittivity. Future work will have to focus on optimisations in the fabrication and patterning of TiN nanostructures to enable higher electro-optical modulation.

The developed simulation model using a combination of electrical FEM and optical FDTD simulations is highly versatile and can be used to analyse novel designs, such as hybrid dimer nanoantennas where the two antenna arms are made out of different materials. In the simulation work in reference [170], such hybrid antennas showed the dipole resonances of both materials, i.e. a resonance at $400\,\mathrm{nm}$ from the silver arm and one at $550\,\mathrm{nm}$ from the gold arm, see Fig. 8.1. The amplitude of the two resonances depends on the refractive index of the surrounding medium, so that the electric field enhancement can be shifted from the silver arm resonance to the gold arm resonance by increasing the refractive index. This design can be used for electrical modulation, where the depletion of ITO around a hybrid nanoantenna could lead to large extinction cross-section modulations.

With new device designs being proposed each year, the application of modulators in plasmonic circuits appears to be just a few years ahead. However, when combining active plasmonic devices, one of the major drawbacks of plasmonics are the high intrinsic losses coming from the confinement of electro-magnetic energy inside the metal. This issue is apparent in the plasmonic waveguide modulators [89–92], which suffer from insertion and propagation losses even in the transmissive state. Combining several of these devices would reduce the optical amplitude so much that active elements would currently have to be employed to compensate the losses after every few modulators. Optical logic circuits based on plasmonics are therefore not yet industrially feasible. More foreseeable applications are individual ultra-compact elements for the amplitude modulation of light in reflection or transmission, where the free-standing modulator presented in this thesis has an advantage over waveguide-based modulators due to the lack of propagation losses.

In conclusion, the work for electro-plasmonic modulation on nanoscale devices continues to push the boundaries of current fabrication and simulation methods. The quantitative characterisation of novel structures will rely heavily on accurate simulation models such as the one presented in this thesis.

Bibliography

[1] Gustav Mie. ‘Beiträge zur Optik trüber Medien, speziell kolloidaler Metallösungen’. In: *Annalen der Physik* 330.3 (1908), pp. 377–445. DOI: `10.1002/andp.19083300302`.

[2] Mario Agio. ‘Optical antennas as nanoscale resonators’. In: *Nanoscale* 4 (3 2012), pp. 692–706. DOI: `10.1039/C1NR11116G`.

[3] Lukas Novotny. ‘From near-field optics to optical antennas’. In: *Physics Today* 64.7 (2011), pp. 47–52. DOI: `10.1063/PT.3.1167`.

[4] Randolph Kirchain and Lionel Kimerling. ‘A roadmap for nanophotonics’. In: *Nature Photonics* 1 (2007), pp. 303–305.

[5] Thomas W. Ebbesen, Cyriaque Genet and Sergey I. Bozhevolnyi. ‘Surface-plasmon circuitry’. In: *Physics Today* 61.5 (2008), pp. 44–50. DOI: `10.1063/1.2930735`.

[6] SV Gaponenko. *Introduction to Nanophotonics*. Cambridge University Press, 2010.

[7] M. Fleischmann, P.J. Hendra and A.J. McQuillan. ‘Raman spectra of pyridine adsorbed at a silver electrode’. In: *Chemical Physics Letters* 26.2 (1974), pp. 163–166. DOI: `10.1016/0009-2614(74)85388-1`.

[8] Alan Campion and Patanjali Kambhampati. ‘Surface-enhanced Raman scattering’. In: *Chemical Society Reviews* 27 (1998), pp. 241–250. DOI: `10.1038/srep40906`.

[9] Paul L. Stiles et al. ‘Surface-enhanced Raman spectroscopy’. In: *Annual Review of Analytical Chemistry* 1 (2008), pp. 601–626. DOI: `10.1146/annurev.anchem.1.031207.112814`.

[10] C. K. Chen, A. R. B. de Castro and Y. R. Shen. ‘Surface-Enhanced Second-Harmonic Generation’. In: *Phys. Rev. Lett.* 46 (2 1981), pp. 145–148. DOI: `10.1103/PhysRevLett.46.145`.

[11] Tolga Ergin et al. ‘Three-Dimensional Invisibility Cloak at Optical Wavelengths’. In: *Science* 328 (2010), pp. 337–339. DOI: `10.1126/science.1186351`.

[12] Jason Valentine, S Zhang and Thomas Zentgraf. ‘Three-dimensional optical metamaterial with a negative refractive index’. In: *Nature* 455.7211 (2008), pp. 376–9. DOI: `10.1038/nature07247`.

[13] D. Schurig et al. ‘Metamaterial Electromagnetic Cloak at Microwave Frequencies’. In: *Science* 314.5801 (2006), pp. 977–980. DOI: `10.1126/science.1133628`.

[14] Hiroki Mashiko et al. ‘Petahertz optical drive with wide-bandgap semiconductor’. In: *Nature Physics Letters* 12 (2016), pp. 741–746. DOI: `10.1038/nphys3711`.

[15] Carlos Ríos et al. ‘Integrated all-photonic non-volatile multi-level memory’. In: *Nature Photonics Letters* 9 (2015), pp. 725–732. DOI: `10.1038/nphoton.2015.182`.

[16] P. Mühlschlegel et al. ‘Resonant Optical Antennas’. In: *Science* 308.5728 (2005), pp. 1607–1609. doi: `10.1126/science.1111886`.

[17] Matthias Dominik Wissert. ‘Optical antennas: Linear and nonlinear excitation and emission’. PhD thesis. Karlsruhe: Karlsruhe Institute of Technology, 2012.

[18] Jiayi Zhang, Tolga Atay and Arto V. Nurmikko. ‘Optical detection of brain cell activity using plasmonic gold nanoparticles’. In: *Nano Letters* 9.2 (2009), pp. 519–524. doi: `10.1021/nl801891q`.

[19] Leo-Jay Black et al. ‘Optimal Polarization Conversion in Coupled Dimer Plasmonic Nanoantennas for Metasurfaces’. In: *ACS Nano* 8.6 (2014), pp. 6390–6399. doi: `10.1021/nn501889s`.

[20] Peter R. Wiecha et al. ‘Polarization Conversion in Plasmonic Nanoantennas using structural asymmetry and mode hybridization’. In: *Scientific Reports* 7 (2017), p. 40906. doi: `10.1038/srep40906`.

[21] Jord C. Prangsma et al. ‘Electrically Connected Resonant Optical Antennas’. In: *Nano Letters* 12.8 (2012), pp. 3915–3919. doi: `10.1021/nl3007374`.

[22] Johannes Kern et al. ‘Electrically driven optical antennas’. In: *Nature Photonics* 9 (2015), pp. 582–586.

[23] Martina Abb et al. ‘Interference, Coupling, and Nonlinear Control of High-Order Modes in Single Asymmetric Nanoantennas’. In: *ACS Nano* 6.7 (2012), pp. 6462–6470. doi: `10.1021/nn3021579`.

[24] Zhong-Jian Yang et al. ‘Twinned Fano interferences induced by hybridized plasmons in Au-Ag nanorod heterodimers’. In: *Applied Physics Letters* 96 (2010), p. 131113. doi: `10.1063/1.3378689`.

[25] Yudong Wang et al. ‘Ultrafast Nonlinear Control of Progressively Loaded, Single Plasmonic Nanoantennas Fabricated Using Helium Ion Milling’. In: *Nano Letters* 13.11 (2013), pp. 5647–5653. doi: `10.1021/nl403316z`.

[26] Katja Dopf et al. ‘Coupled T-shaped optical antennas with two resonances localized in a common nanogap’. In: *ACS Photonics* 2.5 (2015), pp. 1644–1651. doi: `10.1021/acsphotonics.5b00446`.

[27] A. Mohammadi, V. Sandoghdar and M. Agio. ‘Gold, copper, silver and aluminum nanoantennas to enhance spontaneous emission’. In: *Journal of Computational and Theoretical Nanoscience* 6 (2009), pp. 2024–2030. doi: `10.1166/jctn.2009.1259`.

[28] Marta Castro-Lopez et al. ‘Aluminum for Nonlinear Plasmonics: Resonance-Driven Polarized Luminescence of Al, Ag, and Au Nanoantennas’. In: *Nano Letters* 11 (2011), pp. 4674–4678. doi: `10.1021/nl202255g`.

[29] Patrick M. Schwab et al. ‘Linear and Nonlinear Optical Characterization of Aluminum Nanoantennas’. In: *Nano Letters* 13.4 (2013), pp. 1535–1540. doi: `10.1021/nl304692p`.

[30] Zhaleh Pirzadeh et al. ‘Plasmon-Interband coupling in Nickel nanoantennas’. In: *ACS Photonics* 1 (2015), pp. 158–162. doi: `10.1021/acsphotonics.5b00089`.

[31] Peter R. Wiecha et al. 'Enhanced nonlinear optical response from individual silicon nanowires'. In: *Physical Review B* 91.12 (2015), p. 121416. DOI: `10.1103/PhysRevB.91.121416`.

[32] Dianmin Lin et al. 'Dielectric gradient metasurface optical elements'. In: *Science Reports* 345.6194 (2014).

[33] H. H. Li. 'Refractive index of silicon and germanium and its wavelength and temperature derivatives'. In: *Journal of Physical and Chemical Reference Data* 9.3 (1980), pp. 561–658. DOI: `10.1063/1.555624`.

[34] Alexander E. Krasnok et al. 'All-dielectric optical nanoantennas'. In: *Optics Express* 20.18 (2012), pp. 20599–20604. DOI: `10.1364/OE.20.020599`.

[35] Victoriia E. Babicheva, Alexandra Boltasseva and Andrei V. Lavrinenko. 'Transparent conducting oxides for electro-optical plasmonic modulators'. In: *Nanophotonics* 4 (2015), pp. 165–185. DOI: `10.1515/nanoph-2015-0004`.

[36] Tommi Tynell and Maarit Karppinen. 'Atomic layer deposition of ZnO: a review'. In: *Semiconductor Science and Technology* 29, 043001 (2014). DOI: `10.1088/0268-1242/29/043001`.

[37] H Kim et al. 'Electrical, optical, and structural properties of indium-tin-oxide thin films for organic light-emitting devices'. In: *Journal of Applied Physics* 86.11 (1999), pp. 6451–6461. DOI: `10.1063/1.371708`.

[38] HJJ van Boort and R. Groth. 'Low-pressure sodium lamps with indium oxide filter'. In: *Philips Technology Review* 29 (1968), p. 17.

[39] Mamoru Mizuhashi. 'Electrical Properties of Vacuum-Deposited Indium Oxide and Indium Tin Oxide Films'. In: *Thin Solid Films* 70 (1980), pp. 91–100. DOI: `10.1016/0040-6090(80)90415-0`.

[40] Nicolas Large et al. 'Photoconductively Loaded Plasmonic Nanoantenna as Building Block for Ultracompact Optical Switches'. In: *Nano Letters* 10.5 (2010), pp. 1741–1746. DOI: `10.1021/nl1001636`.

[41] Martina Abb et al. 'All-Optical Control of a Single Plasmonic Nanoantenna ITO Hybrid'. In: *Nano Letters* 11.6 (2011), pp. 2457–2463. DOI: `10.1021/nl200901w`.

[42] Martina Abb et al. 'Transparent conducting oxides for active hybrid metamaterial devices'. In: *Journal of Optics* 14.11 (2012). DOI: `10.1088/2040-8978/14/11/114007`.

[43] Martina Abb et al. 'Hotspot-mediated ultrafast nonlinear control of multifrequency plasmonic nanoantennas'. In: *Nature communications* 5 (2014), p. 4869. DOI: `10.1038/ncomms5869`.

[44] Bernd Metzger et al. 'Doubling the Efficiency of Third Harmonic Generation by Positioning ITO Nanocrystals into the Hot-Spot of Plasmonic Gap-Antennas'. In: *Nano Letters* 14.5 (2014), pp. 2867–2872. DOI: `10.1021/nl500913t`.

[45] Antonio Capretti et al. 'Comparative study of second-harmonic generaton from epsilon-near-zero indium tin oxide and titanium nitride nanolayers excited in the near-infrared spectral range'. In: *ACS Photonics* 2.11 (2015), pp. 1584–1591. DOI: `10.1021/acsphotonics.5b00355`.

[46] Jongbum Kim et al. ‘Role of epsilon-near-zero substrates in the optical response of plasmonic antennasn’. In: *Optica* 3.3 (2016). DOI: `10.1364/optica.3.000339`.

[47] L. Caspani et al. ‘Enhanced nonlinear refractive index in ϵ-near-zero materials’. In: *Physical Review Letters* 116 (2016), p. 2339016. DOI: `10.1103/PhysRevLett.116.233901`.

[48] M. Zahirul Alam, Isreal de Leon and Robert W. Boyd. ‘Large optical nonlinearity of indium tin oxide in its epsilon-near-zero region’. In: *Science Reports* 352 (2016), p. 6287. DOI: `10.1126/science.aae0330`.

[49] Peijun Guo et al. ‘Ultrafast switching of tunable infrared plasmons in indium tin oxide nanorod arrays with large absolute amplitude’. In: *Nature Photonics* 10 (2016), pp. 267–273. DOI: `10.1038/nphoton.2016.14`.

[50] Daniel Traviss et al. ‘Ultrafast plasmonics using transparent conductive oxide hybrids in the epsilon-near-zero regime’. In: *Applied Physics Letters* 102.12 (2013), p. 121112. DOI: `10.1063/1.4798833`.

[51] Simon A. Gregory et al. ‘Extreme Subwavelength Metal Oxide Direct and Complementary Metamaterials’. In: *ACS Photonics* 2.5 (2015), pp. 606–614. DOI: `10.1021/acsphotonics.5b00089`.

[52] Martina Abb et al. ‘Surface-Enhanced Infrared Spectroscopy using metal oxide plasmonic antenna arrays’. In: *Nano Letters* 14.1 (2013), pp. 346–352. DOI: `10.1021/nl404115g`.

[53] M. Losurdo et al. ‘Parametrization of optical properties of indium-tin-oxide thin films by spectroscopic ellipsometry: Substrate interfacial reactivity’. In: *Journal of Vacuum Science & Technology A* 20.1 (2002), pp. 37–42. DOI: `10.1116/1.1421596`.

[54] Mark D. Losego et al. ‘Conductive oxide thin films: Model systems for understanding and controlling surface plasmon resonance’. In: *Journal of Applied Physics* 106, 024903 (2009). DOI: `10.1063/1.3174440`.

[55] Xiaoge Liu et al. ‘Quantification and impact of nonparabolicity of the conduction band of indium tin oxide on its plasmonic properties’. In: *Applied Physics Letters* 105.18, 181117 (2014). DOI: `10.1063/1.4900936`.

[56] Yu Wang, Antonio Capretti and Luca dal Negro. ‘Wide tuning of the optical and structural properties of alternative plasmonic materials’. In: *Optical Materials Express* 5.11, 246822 (2015). DOI: `10.1364/OME.5.002415`.

[57] C. Guillén and J. Herrero. ‘Comparing the plasmonic characteristics of sputtered ZnO:Al and In_2O_3:Sn thin films as a function of the heating temperature and atmosphere’. In: *Thin Solid Films* 605 (2016), pp. 136–142. DOI: `10.1016/j.tsf.2015.09.071`.

[58] Tadatsugu Minami, Hidehito Nanto and Shinzo Takata. ‘Highly conductive and transparent aluminum doped zinc oxide thin films prepared by RF magnetron sputtering’. In: *Japanese Journal of Applied Physics* 23.5 (1984), pp. L280–L282.

[59] C. Agashe et al. ‘Efforts to improve carrier mobility in radio frequency sputtered aluminum doped zinc oxide films’. In: *Journal of Applied Physics* 95.4 (2004), pp. 1911–1917. DOI: `10.1063/1.1641524`.

[60] F. Ruske et al. ‘Optical modeling of free electron behavior in highly doped ZnO films’. In: *Thin Solid Films* 518 (2009), pp. 1289–1293. doi: `10.1016/j.tsf.2009.03.218`.

[61] Gururaj V. Naik and Alexandra Boltasseva. ‘Semiconductors for plasmonics and metamaterials’. In: *physica status solidi (RRL) – Rapid Research Letters* 4.10 (2010), pp. 295–297. doi: `10.1002/pssr.201004269`.

[62] Gururaj V. Naik, Vladimir M. Shalaev and Alexandra Boltasseva. ‘Alternative Plasmonic Materials: Beyond Gold and Silver’. In: *Advanced Materials* 25 (2013), pp. 3264–3294. doi: `10.1002/adma.201205076`.

[63] H Kim et al. ‘Optimization of Al-doped ZnO films for low loss plasmonic materials at telecommunication wavelengths’. In: *Applied Physics Letters* 102, 171103 (2013).

[64] G Frank and H. Köstlin. ‘Electrical properties and defect model of tin-doped indium oxide layers’. In: *Applied Physics A* 27 (1982), pp. 197–206. doi: `10.1007/BF00619080`.

[65] M. Losurdo et al. ‘Interrelation between nanostructure and optical properties of oxide thin films by spectroscopic ellipsometry’. In: *Surface and Coatings Technology* 151–152 (2002), pp. 2–8. doi: `10.1016/S0257-8972(01)01617-6`.

[66] Woo-Hee Kim et al. ‘Low Pressure Chemical Vapor Deposition of Aluminum-Doped Zinc Oxide for Transparent Conducting Electrodes’. In: *Journal of The Electrochemical Society* 158.8 (2011), pp. D495–D499. doi: `10.1149/1.3599055`.

[67] Davood Raoufi et al. ‘Surface characterization and microstructure of ITO thin films at different annealing temperatures’. In: *Applied Surface Science* 253 (2007), pp. 9085–9090. doi: `10.1016/j.apsusc.2007.05.032`.

[68] H A Mohamed. ‘The effect of annealing and ZnO dopant on the optoelectronic properties of ITO thin films’. In: *Journal of Physics D: Applied Physics* 40 (2007), pp. 4234–4240. doi: `10.1088/0022-3727/40/14/019`.

[69] J. S. Kim et al. ‘Increase of charge carriers density and reduction of Hall mobilities in oxygen-plasma treated indium-tin-oxide anodes’. In: *Applied Physics Letters* 75.1 (1999), pp. 19–21.

[70] Scott H. Brewer and Stefan Franzen. ‘Indium tin oxide plasma frequency dependence on sheet resistance and surface adlayers determined by reflectance FTIR spectroscopy’. In: *Journal of Physical Chemistry B* 106 (2002), pp. 12986–12992.

[71] Scott H. Brewer and Stefan Franzen. ‘Calculation of the electronic and optical properties of indium tin oxide by density functional theory’. In: *Chemical Physics* 300 (2003), pp. 285–293.

[72] Richard W. Johnson, Adam Hultqvist and Stacey F. Bent. ‘A brief review of atomic layer deposition: from fundamentals to applications’. In: *Materials Today* 17.5 (2014), pp. 236–246. doi: `10.1016/j.mattod.2014.04.026`.

[73] Andreas Frölich and Martin Wegener. ‘Spectroscopic characterization of highly doped ZnO films grown by atomic-layer deposition for three-dimensional infrared metamaterials’. In: *Optical Materials Express* 1.5 (2011), p. 883. doi: `10.1364/OME.1.000883`.

[74] Hanna Saarenpää et al. 'Aluminum doped zinc oxide films grown by atomic layer deposition for organic photovoltaic devices'. In: *Solar Energy Materials & Solar Cells* 94 (2010), pp. 1379–1383. DOI: `10.1016/j.solmat.2010.04.006`.

[75] J. W. Elam and S. M. George. 'Growth of Zno/Al_2O_3 alloy films using atomic layer deposition techniques'. In: *Chemical Materials* 15 (2003), pp. 1020–1028. DOI: `10.1021/cm020607+`.

[76] A. K. Pradhan et al. 'Extreme tunability in aluminum doped zinc oxide plasmonic materials for near-infrared appliations'. In: *Scientific Reports* 4 (2014). DOI: `10.1038/srep06415`.

[77] M B Cortie, J Giddings and A Dowd. 'Optical properties and plasmon resonances of titanium nitride nanostructures'. In: *Nanotechnology* 21.11 (2010), pp. 115–201.

[78] P. Patsalas and S. Logothetidis. 'Optical, electronic, and transport properties of nanocrystalline titanium nitride thin films'. In: *Journal of Applied Physics* 90.9 (2001), pp. 4725–4734. DOI: `10.1063/1.1403677`.

[79] Kenji Hinode et al. 'Morphology-dependent oxidation behavior of reactively sputtered titanium-nitride films'. In: *Journal of Vacuum Science & Technology A* 15.4 (1997), pp. 2017–2022. DOI: `10.1116/1.580673`.

[80] J. S. Chawla, X. Y. Zhang and D. Gall. 'Effective electron mean free path in TiN(001)'. In: *Journal of Applied Physics* 113.6, 063704 (2013). DOI: `10.1063/1.4790136`.

[81] Shunsuke Murai et al. 'Plasmonic arrays of titanium nitride nanoparticles fabricated from epitaxial thin films'. In: *Opt. Express* 24.2 (2016), pp. 1143–1153. DOI: `10.1364/OE.24.001143`.

[82] Eyal Feigenbaum, Kenneth Diest and Harry A. Atwater. 'Unity-Order Index Change in Transparent Conducting Oxides at Visible Frequencies'. In: *Nano Letters* 10.6 (2010), pp. 2111–2116. DOI: `10.1021/nl1006307`.

[83] Wenshan Cai, Justin S. White and Mark L. Brongersma. 'Compact, high-speed and power-efficient electrooptic plasmonic modulators'. In: *Nano Letters* 9.12 (2009), pp. 4403–4411.

[84] VE Babicheva and IV Kulkova. 'Plasmonic modulator based on gain-assisted metal-semiconductor-metal waveguide'. In: *Photonics and Nanostructures – Fundamentals and Applications* 10.4 (2012), pp. 389–399.

[85] Zhaolin Lu, Wangshi Zhao and Kaifeng Shi. 'Nanoscale Plasmonic and Optical Modulators Based on Transparent Conducting Oxides'. In: *Physics.optics* (2012).

[86] Alok P. Vasudev et al. 'Electro-optical modulation of a silicon waveguide with an "epsilon-near-zero" material'. In: *Optics Express* 21.22 (2013), pp. 26387–26397. DOI: `10.1364/OE.21.026387`.

[87] Lin Jin et al. 'Electro-absorption modulator with dual carrier accumulation layers based on epsilon-near-zero ITO'. In: *Plasmonics* 11.4 (2015), pp. 1087–1092. DOI: `10.1007/s11468-015-0146-5`.

[88] U. Koch et al. 'Digital Plasmonic Absorption Modulator Exploiting Epsilon-Near-Zero in Transparent Conducting Oxides'. In: *IEEE Photonics Journal* 8.1 (2016), pp. 1–13. DOI: `10.1109/JPHOT.2016.2518861`.

[89] Jennifer A. Dionne et al. ‘PlasMOStor: A Metal-Oxide-Si Field Effect Plasmonic Modulator’. In: *Nano Letters* 9.2 (2009), pp. 897–902. DOI: `10.1021/nl803868k`.

[90] A. Melikyan et al. ‘Surface plasmon polariton absorption modulator’. In: *Optics Express* 19.9 (2011), pp. 8855–8869. DOI: `10.1364/OE.19.008855`.

[91] VJ Sorger et al. ‘Ultra-compact silicon nanophotonic modulator with broadband response’. In: *Nanophotonics* 1.1 (2012), pp. 17–22. DOI: `10.1515/nanoph-2012-0009`.

[92] Ho W. Lee et al. ‘Nanoscale Conducting Oxide PlasMOStor’. In: *Nano Letters* 14.11 (2014), pp. 6463–6468. DOI: `10.1021/nl502998z`.

[93] G. D. Wilk, R. M. Wallace and J. M. Anthony. ‘High-κ gate dielectrics: Current status and materials properties considerations’. In: *Journal of Applied Physics* 89.10 (2001), pp. 5243–5275. DOI: `10.1063/1.1361065`.

[94] S. M. Sze. *Semiconductor Devices: Physics and Technology*. 2nd. John Wiley & Sons, 2001.

[95] M. F. Al-Kuhaili. ‘Optical properties of hafnium oxide thin films and their application in energy-efficient windows’. In: *Optical Materials* 27.3 (2004), pp. 383–387. DOI: `10.1016/j.optmat.2004.04.014`.

[96] Kaupo Kukli et al. ‘Properties of hafnium oxide films grown by atomic layer deposition from hafnium tetraiodide and oxygen’. In: *Journal of Applied Physics* 92.10 (2002), pp. 5698–5703. DOI: `10.1063/1.1515107`.

[97] Cédric Sire et al. ‘Statistics of electrical breakdown field in HfO2 and SiO2 films from millimeter to nanometer length scales’. In: *Applied Physics Letters* 91.24 (2007). DOI: `10.1063/1.2822420`.

[98] A. Melikyan et al. ‘High-speed plasmonic phase modulators’. In: *Nature Photonics* 8.3 (2014), pp. 229–233. DOI: `10.1038/nphoton.2014.9`.

[99] Gang Xu et al. ‘Electron injection assisted phase transition in a nano-Au-VO2 junction’. In: *Applied Physics Letters* 93.6 (2008), p. 061911. DOI: `10.1063/1.2972106`.

[100] Jong-ho Choe and Jin Tae Kim. ‘Design of Vanadium Dioxide-Based Plasmonic Modulator for Both TE and TM Modes’. In: 27.5 (2015), pp. 514–517. DOI: `10.1109/LPT.2014.2384020`.

[101] Patr Markov et al. ‘Optically monitored electrical switching in VO_2’. In: *ACS Photonics* 2 (2015), pp. 1175–1182. DOI: `10.1021/acsphotonics.5b00244`.

[102] C Hoessbacher, Y Fedoryshyn and A Emboras. ‘The plasmonic memristor: a latching optical switch’. In: *Optica* 1.4 (2014), pp. 198–202. DOI: `10.1364/OPTICA.1.000198`.

[103] Alexandros Emboras et al. ‘Atomic scale plasmonic switch’. In: *Nano Letters* 16 (2015), pp. 709–714. DOI: `10.1021/acs.nanolett.5b04537`.

[104] Alexandre Aubry et al. ‘Plasmonic Light-Harvesting Devices over the Whole Visible Spectrum’. In: *Nano Letters* 10.7 (2010), pp. 2574–2579.

[105] Hao Wang and Liping Wang. ‘Perfect selective metamaterial solar absorbers’. In: *Opt. Express* 21.S6 (2013), A1078–A1093.

[106] N. I. Landy et al. ‘Perfect Metamaterial Absorber’. In: *Phys. Rev. Lett.* 100 (20 2008), p. 207402.

[107] Na Liu et al. ‘Infrared Perfect Absorber and Its Application As Plasmonic Sensor’. In: *Nano Letters* 10.7 (2010), pp. 2342–2348.

[108] Claire M. Watts, Xianliang Liu and Willie J. Padilla. ‘Metamaterial Electromagnetic Wave Absorbers’. In: *Advanced Materials* 24.23 (2012), OP98–OP120.

[109] K. Aydin et al. ‘Broadband polarization-independent resonant light absorption using ultrathin plasmonic super absorbers’. In: *Nature Communications* 2.517 (2011).

[110] Jeremy A. Bossard et al. ‘Near-Ideal Optical Metamaterial Absorbers with Super-Octave Bandwidth’. In: *ACS Nano* 8.2 (2014), pp. 1517–1524.

[111] Qiang Cheng et al. ‘An omnidirectional electromagnetic absorber made of metamaterials’. In: *New Journal of Physics* 12.6 (2010), p. 063006.

[112] J. Ginn et al. ‘Altering infrared metamaterial performance through metal resonance damping’. In: *Journal of Applied Physics* 105.7 (2009), p. 074304.

[113] Fei Yi et al. ‘Voltage tuning of plasmonic absorbers by indium tin oxide’. In: *Applied Physics Letters* 102.22, 221102 (2013). DOI: `10.1063/1.4809516`.

[114] Sa’ad Hassan et al. ‘Fabrication of a plasmonic modulator incorporating an overlaid grating coupler’. In: *Nanotechnology* 25 (2014), p. 495202. DOI: `10.1088/0957-4484/25/49/495202`.

[115] Anthony Olivieri et al. ‘Plasmonic nanostructured metal-oxide-semiconductor reflection modulator’. In: *Nano Letters* 15 (2015), pp. 2304–2311. DOI: `10.1021/nl504389f`.

[116] Yu Yao et al. ‘Electrically Tunable Metasurface Perfect Absorbers for Ultrathin Mid-Infrared Optical Modulators’. In: *Nano Letters* 14.11 (2014), pp. 6526–6532. DOI: `10.1021/nl503104n`.

[117] Junghyun Park et al. ‘Electrically Tunable Epsilon-Near-Zero (ENZ) Metafilm Absorbers’. In: *Scientific Reports* 5 (2015). DOI: `10.1038/srep15754`.

[118] Junghyun Park et al. ‘Dynamic Reflection Phase and Polarization Control in Metasurfaces’. In: *Nano Letters* 17.1 (2017), pp. 407–413. DOI: `10.1021/acs.nanolett.6b04378`.

[119] Yao-Wei Huang et al. ‘Gate-Tunable conducting oxide metasurfaces’. In: *Nano Letters* 16 (2016), pp. 5319–5325. DOI: `10.1021/acs.nanolett.6b00555`.

[120] Prasad P. Iyer, Mihir Pendharkar and Jon A. Schuller. ‘Electrically Reconfigurable metasurfaces using heterojunction resonators’. In: *Advanced Optical Materials* (2016). DOI: `10.1002/adom.201600297`.

[121] Lukas Novotny. ‘Effective Wavelength Scaling for Optical Antennas’. In: *Physical Review Letters* 98 (26 2007). DOI: `10.1103/PhysRevLett.98.266802`.

[122] Garnett W. Bryant, F. Javier Garcia de Abajo and Javier Aizpurua. ‘Mapping the plasmon resonances of metallic nanoantennas’. In: *Nano Letters* 8.2 (2008), pp. 631–636. DOI: `10.1021/nl073042v`.

[123] Craig F Bohren and Donald R Huffman. *Absorption and Scattering of Light by Small Particles*. Wiley Science Paperback Series 6. Wiley, 1983. Chap. 4. DOI: `10.1017/S0263574798270858`.

[124] Hitoshi Kuwata et al. 'Resonant light scattering from metal nanoparticles: Practical analysis beyond Rayleigh approximation'. In: *Applied Physics Letters* 83.22 (2003), pp. 4625–4627. DOI: `10.1063/1.1630351`.

[125] Jens Dorfmüller et al. 'Plasmonic nanowire antennas: Experiment, simulation, and theory'. In: *Nano Letters* 10.9 (2010), pp. 3596–603. DOI: `10.1021/nl101921y`.

[126] John R. Rumble. *CRC Handbook of Chemistry and Physics*. Taylor & Francis, 2017.

[127] P. B. Johnson and R. W. Christy. 'Optical Constants of the Noble Metals'. In: *Phys. Rev. B* 6 (12 1972), pp. 4370–4379. DOI: `10.1103/PhysRevB.6.4370`.

[128] Carolina Novo et al. 'Contributions from radiation damping and surface scattering to the linewidth of the longitudinal plasmon band of gold nanorods: a single particle study'. In: *Physical chemistry chemical physics* 8 (2006), pp. 3540–3546. DOI: `10.1039/b604856k`.

[129] C Moosmann et al. 'Investigating the influences of the precise manufactured shape of dipole nanoantennas on their optical properties'. In: *Optics express* 21.1 (2013), pp. 594–604. DOI: `10.1364/OE.21.000594`.

[130] Andreas Trügler and Ulrich Hohenester. 'Strong coupling between a metallic nanoparticle and a single molecule'. In: *Physical Review B* 77 (2008). DOI: `10.1103/PhysRevB.77.115403`.

[131] C. Rhodes et al. 'Dependence of plasmon polaritons on the thickness of indium tin oxide thin films'. In: *Journal of Applied Physics* 103 (2008), p. 093108. DOI: `10.1063/1.2908862`.

[132] J. Aizpurua et al. 'Optical properties of coupled metallic nanorods for field-enhanced spectroscopy'. In: *Physical Review B* 71 (23 2005), p. 235420. DOI: `10.1103/PhysRevB.71.235420`.

[133] Mario Agio and Andrea Alù. *Optical Antennas*. Cambridge University Press, 2013.

[134] P. Nordlander et al. 'Plasmon Hybridization in Nanoparticle Dimers'. In: *Nano Letters* 4.5 (2004), pp. 899–903.

[135] Prashant K. Jain and Mostafa A. El-Sayed. 'Plasmonic coupling in noble metal nanostructures'. In: *Chemical Physics Letters* 487.4–6 (2010), pp. 153–164. DOI: `10.1016/j.cplett.2010.01.062`.

[136] Weihua Zhang and Olivier J. F. Martin. 'A Universal Law for Plasmon Resonance Shift in Biosensing'. In: *ACS Photonics* 2 (2015), pp. 144–150. DOI: `10.1021/ph500355d`.

[137] Prashant K. Jain, Wenyu Huang and Mostafa A. El-Sayed. 'On the Universal Scaling Behavior of the Distance Decay of Plasmon Coupling in Metal Nanoparticle Pairs: A Plasmon Ruler Equation'. In: *Nano Letters* 7.7 (2007), pp. 2080–2088. DOI: `10.1021/nl071008a`.

[138] Robert W Boyd. *Nonlinear Optics*. Academic press, 2003.

[139] A. Illiberi et al. 'Spatial atmospheric atomic layer deposition of $\mathrm{Al}_x\mathrm{Zn}_{1-x}\mathrm{O}$'. In: *Applied Materials & Interfaces* 5 (2013), pp. 13124–13128. DOI: `10.1021/am404137e`.

[140] Do-Joong Lee et al. 'Structural and Electrical Properties of Atomic Layer Deposited Al-Doped ZnO Films'. In: *Advanced Functional Materials* 21.3 (2011), pp. 448–455. DOI: `10.1002/adfm.201001342`.

[141] O. L. Muskens et al. 'Optical extinction spectrum of a single metal nanoparticle: Quantitative characterization of a particle and of its local environment'. In: *Phys. Rev. B* 78 (20 2008). DOI: `10.1103/PhysRevB.78.205410`.

[142] A. Arbouet et al. 'Direct Measurement of the Single-Metal-Cluster Optical Absorption'. In: *Phys. Rev. Lett.* 93 (12 2004). DOI: `10.1103/PhysRevLett.93.127401`.

[143] Aurelien Crut et al. 'Optical absorption and scattering spectroscopies of single nano-objects'. In: *Chem. Soc. Rev.* 43 (11 2014), pp. 3921–3956. DOI: `10.1039/C3CS60367A`.

[144] Natasha Fairbairn et al. 'Single-nanoparticle detection and spectroscopy in cells using a hyperspectral darkfield imaging technique'. In: *SPIE Proceedings* 8595 (2013). DOI: `10.1117/12.981941`.

[145] Jonathan A. Fan et al. 'Near-Normal Incidence Dark-Field Microscopy: Applications to Nanoplasmonic Spectroscopy'. In: *Nano Letters* 12.6 (2012), pp. 2817–2821. DOI: `10.1021/nl300160y`.

[146] Otto Muskens et al. 'Optical response of a single noble metal nanoparticle'. In: *Journal of Optics A: Pure and Applied Optics* 8.4 (2006), S264–S272. DOI: `10.1088/1464-4258/8/4/S28`.

[147] OL Muskens and Guillaume Bachelier. 'Quantitative absorption spectroscopy of a single gold nanorod'. In: *The Journal of Physical Chemistry C* 112 (2008), pp. 8917–8921.

[148] N Fairbairn et al. 'Spatial modulation microscopy for real-time imaging of plasmonic nanoparticles and cells'. In: *Optics Letters* 37.15 (2012), pp. 3015–3017.

[149] Otto L Muskens, Natalia Del Fatti and Fabrice Vallée. 'Femtosecond response of a single metal nanoparticle'. In: *Nano Letters* 6.3 (2006), pp. 552–6. DOI: `10.1021/nl0524086`.

[150] Katja Dopf et al. 'Superresolution optical fluctuation imaging (SOFI) aided nanomanipulation of quantum dots using AFM for novel artificial arrangements of chemically functionalized colloidal quantum dots and plasmonic structures'. In: *SPIE Proceedings* 9126 (2014), 91260N-1–91260N-9. DOI: `10.1117/12.2051277`.

[151] Antonino Calà Lesina et al. 'On the convergence and accuracy of the FDTD method for nanoplasmonics'. In: *Optics Express* 23.8 (2015), pp. 10481–10497. DOI: `10.1364/OE.23.010481`.

[152] D. L. Wood et al. 'Optical properties of cubic hafnia stabilized with yttria'. In: *Applied Optics* 29.4 (1990), pp. 604–607. DOI: `10.1364/AO.29.000604`.

[153] Edward D. Palik. *Handbook of Optical Constants of Solids*. Academic Press, 1997.

[154] Andreas Trügler. 'Optical properties of metallic nanoparticles'. PhD thesis. Karl-Franzens-Universität Graz, 2011.

[155] Ulrich Hohenester and Andreas Trügler. 'MNPBEM – A Matlab toolbox for the simulation of plasmonic nanoparticles'. In: *Computer Physics Communications* 183.2 (2012), pp. 370–381. DOI: `10.1016/j.cpc.2011.09.009`.

[156] Jasmin Smajic et al. 'Comparison of numerical methods for theaAnalysis of plasmonic structures'. In: *Journal of Computational and Theoretical Nanoscience* 6 (2009), pp. 1–12. DOI: `10.1166/jctn.2009.1107`.

[157] Wilfried Ley, Klaus Wittmann and Willi Hallmann. *Handbook of Space Technology*. Wiley, 2009. Chap. 4.3.

[158] John H. Henninger. 'Solar absorptance and thermal emittance of some common spacecraft thermal-control coatings'. In: *NASA Reference Publication* 1121 (1984).

[159] David G. Gilmore. *Spacecraft Thermal Control Handbook I*. The Aerospace, 2002. Chap. 4.

[160] European cooperation for space standardization. 'Space product assurance – measurements of thermo-optical properties of thermal control materials'. In: *ESA Requirements and Standards Division* (2008).

[161] R. L. Fante and M. T. McCormack. 'Reflection properties of the Salisbury screen'. In: *IEEE Transactions on Antennas and Propagation* 36.10 (1988), pp. 1443–1454. DOI: `10.1109/8.8632`.

[162] Akiyoshi Mitsuishi, Yahiko Yamada and Hiroshi Yoshinaga. 'Reflection Measurements on Reststrahlen Crystals in the Far-Infrared Region'. In: *Journal of the Optical Society of America* 52.1 (1962), pp. 14–16. DOI: `10.1364/JOSA.52.000014`.

[163] G. Kirchhoff. 'Ueber das Verhältniss zwischen dem Emissionsvermögen und dem Absorptionsvermögen der Körper für Wärme und Licht'. In: *Annalen der Physik* 185.2 (1860), pp. 275–301. ISSN: 1521-3889. DOI: `10.1002/andp.18601850205`. URL: `http://dx.doi.org/10.1002/andp.18601850205`.

[164] M. Benkahoul et al. 'Thermochromic VO2 film deposited on Al with tunable thermal emissivity for space applications'. In: *Solar Energy Materials and Solar Cells* 95.12 (2011), pp. 3504–3508. DOI: `https://doi.org/10.1016/j.solmat.2011.08.014`.

[165] Christoph A. Riedel et al. 'Nanoscale modeling of electro-plasmonic tunable devices for modulators and metasurfaces'. In: *Opt. Express* 25.9 (2017), pp. 10031–10043. DOI: `10.1364/OE.25.010031`.

[166] CH de Groot et al. 'Quantification of misalignment in e-beam lithography due to height map error on optically non-uniform substrates for plasmonic nanoantennas'. In: *International Conference on Nanotechnology (IEEE nano)*. Ed. by IEEE. Vol. 15. 2015.

[167] Yudong Wang. 'Magnetoresistance in constrained domain walls'. PhD thesis. University of Southampton, 2013.

[168] Krishnan Thyagarajan et al. 'Millivolt modulation of plasmonic metasurface optical response via ionic conductance'. In: *Advanced Materials* 29 (2017), p. 1701044. DOI: `10.1002/adma.201701044`.

[169] Xiaoge Liu and Ju-Hyung Kang and Hongtao Yuan and Junghyun Park and Soo Jin Kim and Yi Cui and Harold Y. Hwang and Mark L. Brongersma. ‘Electrical tuning of a quantum plasmonic resonance’. In: *Nature Nanotechnology* 3 (2017). Advance Online Publication, pp. 1–5. DOI: `10.1038/nnano.2017.103L3`.

[170] Guangqing Du et al. ‘Localized surface plasmon resonances in core-embedded heterogeneous nano-bowtie antenna’. In: *Applied Physics B* 120 (2015), pp. 47–51. DOI: `10.1007/s00340-015-6095-z`.